

IN VITRO AND IN VIVO STUDIES OF NANOMOLDED PRINT® PARTICLES OF
PRECISELY CONTROLLED SIZE, SHAPE, AND SURFACE CHEMISTRY

Stephanie E. A. Gratton

A dissertation submitted to the faculty of the University of North Carolina at Chapel Hill in partial fulfillment of the requirements for the degree of Doctor of Philosophy in the Department of Chemistry.

Chapel Hill
2008

Approved by:

Joseph M. DeSimone

Moo J. Cho

Rudolph Juliano

Valerie Ashby

Michael Rubinstein

ABSTRACT

Stephanie E. A. Gratton

In vitro and *in vivo* studies of nanomolded PRINT particles of precisely controlled size, shape, and surface chemistry

(Under the direction of Professor Joseph M. DeSimone)

A novel method for the fabrication of polymeric particles on the order of tens of nanometers to several microns is described. This imprint lithographic technique called PRINT (Particle Replication In Non-wetting Templates), takes advantage of the unique properties of elastomeric molds comprised of a low surface energy perfluoropolyether network, allowing the production of monodisperse, shape-specific nanoparticles from an extensive array of organic precursors. This engineered nature of particle production has a number of advantages over the construction of traditional nanoparticles such as liposomes, dendrimers, and colloidal precipitates. The gentle “top down” approach of PRINT enables the simultaneous and independent control over particle size and shape, composition, and surface functionality, and permits the loading of delicate cargos such as small organic therapeutics and biological macromolecules. Thus, this single tool serves as a comprehensive platform for the rational design and investigation of new nanocarriers in medicine, having applications ranging from therapeutics to advanced diagnostics.

Preliminary *in vitro* and *in vivo* studies were conducted, demonstrating the future utility of PRINT particles as delivery vectors in nanomedicine.

The interaction of particles with cells is known to be strongly influenced by particle size, however little is known about the interdependent role that size, shape and surface chemistry have on cellular internalization and intracellular trafficking. The internalization of specially-designed, monodisperse hydrogel particles was examined using HeLa cells as a function of size, shape, and surface charge. Evidence of particle internalization was obtained using conventional biological techniques as well as transmission electron microscopy. These findings suggest that HeLa cells readily internalize non-spherical particles with dimensions as large as 3 μm using several different mechanisms of endocytosis. Moreover, it was found that rod-like particles enjoy an appreciable advantage when it comes to internalization rates, reminiscent of the advantage that many rod-like bacteria have for internalization in non-phagocytic cells.

DEDICATION

To all of my family and friends, for their continued love and support

ACKNOWLEDGEMENTS

First, I would like to thank my Ph.D. advisor, Dr. Joseph M. DeSimone for his support and guidance throughout the years. This experience has truly been invaluable and has taught me an immense amount as a scientist, and as a person. Dr. DeSimone has always been able to inspire me to do better, and I owe a lot of my scientific development to him. Thank you.

I would also like to thank Dr. Mary E. Napier for many scientific discussions and moral support for the last couple of years. Many thanks go out to all members of the DeSimone lab, both past and present. Special thanks go to: Dr. Patrick D. Pohlhaus, Dr. Matthew C. Parrott, Dr. Patricia A. Ropp, Dr. Candice Brannen, Dr. J. Christopher Luft, Dr. Shaomin Tian, Dr. Ji Guo, Kevin P. Herlihy, Stuart S. Williams, Stephen P. Jones, Timothy Merkel, Janine Nunes, Dr. Henry Zhang, Dr. Jin Wang, Dr. Jason P. Rolland, Dr. Ginger Rothrock, and Dr. Benjamin W. Maynor.

I have been blessed with a multitude of successful collaborations outside of the DeSimone laboratory, and I would like to thank the following people for their contribution to this work: Dr. Marieke van der Aa, Dr. Francis C. Szoka, Dr. Clifton Shen, Dr. Anna Wu, Dr. Tove Olafsen, Dr. Hsiang-Rong Tseng, Dr. Michael Phelps, Dr. Anne Wolthusen, Dr. Terry Van Dyke, Dr. Jin Lee, Dr. Moo J. Cho, Dr. Hyunmin Kang, Dr. Rudolph Juliano, Dr. David A. Olson,

Dr. Benjamin F. Pierce, Dr. Valerie V. Sheares, Charlene M. Ross and the entire animal studies core. I would also like to express my gratitude to my undergraduate advisor, Dr. Alex Adronov for all of advice and mentoring of me throughout the years. It was Dr. Alex Adronov and Dr. Paul Ayers who encouraged me to attend graduate school, particularly at UNC Chapel Hill.

I owe a big thank you to the doctors at the University of North Carolina at Chapel Hill, especially Dr. Stephan Moll, Mr. Bart Scott, and Dr. Timothy Sadiq for keeping me alive and trying their best to keep me pain-free.

I would especially like to thank my family and friends who have supported me throughout all my life endeavors. Particular thanks go to Michael J. Barrett, Dr. Stefanie A. Mortimer, Brittany C. Westlake, Brandi Hill, and Kerri Henderson. Thank you all very much. I would also like to thank my brother and sister, James and MaryAnne Gratton, who have always shown their love and support. Lastly, and most importantly, I wish to thank my parents, Linda and Daniel Gratton, whom have always supported and encouraged me to do my best.

TABLE OF CONTENTS

	Page
LIST OF TABLES.....	xii
LIST OF FIGURES.....	xiii
LIST OF ABBREVIATIONS.....	xx
Chapter 1. Nanoparticles in Medicine.....	1
1.1 Nanoparticle therapeutics.....	2
1.2 Development of optimal nanoparticles for therapeutic applications.....	3
1.2.1 Nanoparticle size.....	7
1.2.2 Nanoparticle shape.....	8
1.2.3 Surface properties.....	9
1.3 Challenges with polymer conjugates as nanoparticle-based therapeutics.....	11
1.4 Challenges with liposome-as nanoparticle-based therapeutics.....	11
1.5 Imparting size, shape, and composition control of materials for nanomedicine.....	13
1.6 The future of nanomedicine.....	23
1.7 References.....	26

Chapter 2. The effect of particle design on cellular internalization pathways.....	29
2.1 Introduction.....	30
2.2 Experimental.....	34
2.2.1 Materials.....	34
2.2.2 PRINT particle preparation.....	35
2.2.3 Particle size analysis of PRINT particles using scanning electron microscopy.....	37
2.2.4 Zeta potential measurements.....	37
2.2.5 Cell lines and maintenance.....	37
2.2.6 Cell uptake and cytotoxicity – The effect of charge using 1 μm (AR = 1) particles.....	38
2.2.7 <i>In vitro</i> cytotoxicity – The effect of size and shape.....	39
2.2.8 Uptake experiments – The effect of size and shape.....	39
2.2.9 Confocal laser scanning microscopy.....	40
2.2.10 Transmission electron microscopy (TEM).....	41
2.2.11 Inhibitor studies.....	42
2.3 Results and discussion.....	42
2.4 Conclusions.....	63
2.5 References.....	65
Chapter 3. Nanofabricated particles for engineered drug therapies: A preliminary biodistribution study of PRINT nanoparticles.....	67

3.1 Introduction.....	68
3.2 Experimental.....	69
3.2.1 Materials.....	69
3.2.2 Preparation of PRINT nanoparticles.....	70
3.2.3 Preparation of liposomes.....	73
3.2.4 Particle size analysis of PRINT nanoparticles using scanning electron microscopy (in the dry state).....	73
3.2.5 Particles size analysis of PRINT nanoparticles and liposomes using dynamic light scattering (in suspension).....	74
3.2.6 Zeta potential measurements.....	74
3.2.7 Radiolabeling of PRINT nanoparticles with ^{125}I	75
3.2.8 <i>In vitro</i> cytotoxicity.....	76
3.2.9 Biodistribution of [^{125}I]-labeled PRINT particles.....	76
3.3 Results and discussion.....	86
3.4 Conclusions.....	88
3.5 References.....	
Chapter 4. Exploiting the enhanced permeability and retention effect for tumor targeting.....	90
4.1 Introduction.....	91
4.2 Experimental.....	93
4.2.1 Materials.....	93

4.2.2	Preparation of surface-functionalized PRINT nanoparticles.....	93
4.2.3	Particle size analysis of PRINT nanoparticles using scanning electron microscopy (in the dry state).....	95
4.2.4	Particles size analysis of PRINT nanoparticles using dynamic light scattering (in suspension).....	96
4.2.5	Zeta potential measurements.....	96
4.2.6	<i>In vitro</i> internalization.....	96
4.2.7	<i>In vitro</i> cytotoxicity.....	97
4.2.8	Hemolysis assay using 200 nm PEGylated PRINT particles.....	98
4.2.9	Biodistribution of fluorescently-tagged 200 nm PEGylated PRINT particles.....	98
4.2.10	Dosing study using a fluorescently-tagged 200 nm PEGylated PRINT particles.....	100
4.3	Results and discussion.....	100
4.4	Conclusions.....	115
4.5	References.....	117
Chapter 5.	Summary of conclusions and recommendations for future work.....	119
5.1	Summary of conclusions.....	120
5.1.1	Cellular uptake mechanisms of non-targeted organic PRINT particles.....	120
5.1.2	Preliminary biodistribution studies of PRINT particles.....	122
5.1.3	Taking advantage of the enhanced permeability and retention effect.....	123

5.2 Recommendations for future work.....	124
5.2.1 Engineering unique particle shapes and the <i>in vitro</i> and <i>in vivo</i> implications.....	125
5.2.2 Imparting superior control over particle surface chemistry.....	128
5.2.3 Actively targeting cancer cells using a targeting ligand.....	135
5.2.4 Examining the effect of modulus on <i>in vivo</i> circulation times.....	138
5.3 References.....	140

LIST OF TABLES

Table 1.1	Clinically approved liposomal therapeutics.....	5
Table 1.2	Clinically approved polymeric therapeutics.....	6
Table 1.3	Clinically approved nanoparticle-based therapeutics.....	7
Table 2.1	Particle composition.....	36
Table 2.2	Particle size and surface charge characterization as determined by scanning electron microscopy and zeta potential measurements (respectively). Particle labels describe master cavity size.....	45
Table 3.1	Particle composition.....	71
Table 3.2	Particle characterization.....	78
Table 4.1	Particle composition.....	94
Table 4.2	Particle characterization.....	103
Table 4.3	The effect of dosing at 6 h post-injection. In these experiments, it was found that not all organ accumulations scaled linearly with a doubling of dose (i.e. lungs, kidneys, heart, and tumor).....	115

LIST OF FIGURES

Figure 1.1	Common nanoparticle-based therapeutics approved for Clinical use.....	2
Figure 1.2	Ligand-receptor interactions on cancer cells. Molecular conjugates and multivalent particles are equally efficient at targeting when the surface density of the receptor is low. However, targeted nanoparticles are much more efficient at targeting cancer cells when the surface density of the receptor on the cancer cells is high (for example, the transferrin receptor).....	10
Figure 1.3	Schematic illustration of the PRINT process and traditional embossing processes: (A) Silicon master template; (B) mold release from master template; (C) mold filling via capillary fill with counter sheet having a higher surface energy than the PFPE mold. Depending on the exact nature of the liquid to be molded and the details of the process; (D) once can fill the cavities only and not wet the land area around the cavities or (D') once can fill the cavities and have a thin layer of liquid on the land area around the cavities. The thickness of the layer of connecting flash liquid is determined from the principles associated with free meniscus coating processes with the resulting (E and E') pattern transfer to substrate; (F and F') mold release from array of isolated features; and (G) dissolution of the harvesting film to yield free particles. As an alternative to PRINT, one can use PFPEs using traditional embossing processes where pressure and heat are applied (H and I) to form an embossed film (J) after the mold is removed..	16
Figure 1.4	A) Atomic force micrograph of a 160 nm post master; B) scanning electron micrograph of an unused, empty PFPE mold with 160 nm features (aspect ratio = 1:1); and C) a scanning electron micrograph of harvested PEG-composite particles on the medical adhesive sacrificial layer.....	19

Figure 1.5	SEM micrographs of 200 nm monodisperse, shape-specific particles made from a wide range of materials; bioabsorbable, biocompatible, proteins and active pharmaceuticals.....	20
Figure 1.6	PRINT particles varying in size, shape, surface chemistry, and deformability. The particle composition for all of these particles was approximately the same and included PEG (bulk of the matrix), a cross-linker, and a linker group for conjugation of stabilizing groups (such as PEG) or targeting ligands (such as peptides, antibodies, etc). A) Scanning electron micrograph (SEM) of cubic-shaped particles with a cube side length = 5 μm ; B) SEM of cylindrical nanoparticles having diameter = 110 nm and height = 35 nm; C) SEM of cylindrical nanoparticles having diameter = 200 nm and height = 200 nm; D) SEM of rod-like PRINT particles having diameter = 100 nm and height = 300 nm; E) SEM of 3 μm “hex nut” particles; F) Cylindrical PRINT particles containing a covalently attached red fluorophore that have been functionalized on one face with a generic linker group (green fluorophore) that will allow the conjugation of targeting peptides, antibodies, and aptamers region-specifically onto the particle probes; G) and H) Particles for mechano-biology studies having approximately the same dimensions as red blood cells (cylinders with a diameter = 7 μm and a height = 1.7 μm made from (G) a non-deformable, highly cross-linked hydrogel; and (H) lightly cross-linked, deformable hydrogel.....	22
Figure 2.1	Illustration of PRINT. Fabrication of the silicon master template (box, upper left); Wetting of the silicon master with (green) liquid fluoropolymer, followed by curing (top row); PFPE elastomeric mold produced with nanoscale features from the master (upper right); Confining (red) organic liquid to cavities by applying pressure between mold and a PFPE surface (middle row); Removal of organic particles from mold with adhesive layer (bottom left); Dissolution of adhesive layer producing free particles (bottom right).	33
Figure 2.2	Chemical structures of monomers and a partial structure of the PRINT particles.....	36

Figure 2.3	Micrographs of PRINT particles varying in both size and shape. The particle composition for these experiments was 67 wt % trimethyloxypropyl ethoxylate triacrylate (MW = 428 g/mol), 20 wt % poly(ethylene glycol) monomethylether monomethacrylate (MW = 1,000 g/mol), 10 wt % 2-aminoethylmethacrylate hydrochloride (AEM·HCl), 2 wt % fluorescein- <i>O</i> -acrylate, and 1 wt % 2,2-diethoxyacetophenone. Top Row (A-C) Scanning electron micrograph of the cubic series of particles {Diameters equal to 2 μ m (A), 3 μ m (B), and 5 μ m (C)}. Second Row (D-F) fluorescence micrographs of the cubic series of particles {Diameters equal to 2 μ m (D), 3 μ m (E), and 5 μ m (F)}. Third Row (G,H) Scanning electron micrographs of the cylindrical series of microparticles having the same height (1 μ m), but varying diameters (Diameter = 0.5 μ m (G) and 1 μ m (H)). Last Row (I-K) Scanning electron micrographs of a series of cylindrical nanoparticles {Diameter = 200 nm, Height = 200 nm (I), diameter = 100 nm, height = 300 nm (J), diameter = 150 nm, height = 450 nm (K)}. Scale bars = 20 μ m (A-F), 1 μ m (G-K).....	46
Figure 2.4	Internalization profile of PRINT particles with HeLa cells over a 4 hour time period at 37°C. Legend depicts the particle diameter/particle volume.....	47
Figure 2.5	MTS Assay showing the cytotoxicity of all particles under investigation. All experiments were carried out with a 4 h incubation with HeLa cells, except the final bar, where the 200 nm particles were tested for cytotoxicity out to 72 hours.....	49
Figure 2.6	Effect of charge on cellular internalization. A) The chemical transformation, leading to changes in surface charge, B) Particle internalization after 3 hours of incubation with HeLa cells with positively charged particles C) Particle internalization after 4 hours of incubation with HeLa cells with negatively charged particles.....	51
Figure 2.7	Internalization of 1 μ m PRINT particles by various cell lines. Cells were dosed with various concentrations of particles for 4 h at 37°C. (A) Cellular internalization profiles; (B) Cytotoxicity of particles. Red circles represent positively charged particles; blue circles represent negatively charged particles. The data shown were representative of more than three separate experiments.....	54

Figure 2.8	Confocal laser scanning microscopy images of HeLa cells after a 1 h incubation period at 37°C with A) 3µm cubes, B) 2 µm cubes, C) 1 µm (AR = 1) cylinders, D) 200 nm (AR = 1) cylindrical particles {scale bar = 10 µm}.....	57
Figure 2.9	Transmission electron microscopy images of HeLa cells at 37°C (incubation times in parenthesis) with B-D) 200 nm x 200 nm cylindrical particles (AR = 1) (B,C – 15 minutes, D - 4 hours), E-F) 150 nm x 450 nm cylindrical particles (E-F – 1 hour), G-I) 1 µm cylindrical particles (G – 1 hour, H,I – 4 hours).....	59
Figure 2.10	Probing the mechanisms of cellular internalization using inhibitors of endocytosis. HeLa cells were incubated with the indicated inhibitors in the graph as outlined in the experimental methods. Percent internalization was normalized to particle internalization in the absence of inhibitors.....	62
Figure 3.1	Chemical structures of monomers and a partial structure of the PRINT nanogel. <i>p</i> -Hydroxystyrene was introduced for radioiodination at 1% (w/w). Throughout the present study, it is assumed that iodinated PRINT nanogels behave the same as unmodified particles.....	78
Figure 3.2	Scanning electron micrographs of 200 nm PRINT particles used in the present study.....	79
Figure 3.3	A time-dependent study of the mean diameter, polydispersity and stability of PRINT particles (top), and liposomes (bottom) using dynamic light scattering.....	81
Figure 3.4	MTS assay depicting the non-toxic nature of 200 nm PRINT particles incubated with HeLa cells. Approximately 10 ³ cells were plated per 1 cm ² . Cells were exposed to varying concentrations of PRINT particles in 0.1 mL media for 4 h at 37 °C before the MTS assay was performed. Control wells, where the cells were exposed to only PBS serve as 100% in normalization. Vertical bars stand for one SD with n = 5.....	82

Figure 3.5	Biodistribution of 200 nm [¹²⁵ I]-labeled PRINT particles in healthy mice subsequent to bolus tail vein injection at a dose of 20 mg/kg. The organ accumulation is expressed as a percent of injected dose after animals were sacrificed at 10 min, 30 min, 1, 3, 8, and 24 h post-intravenous injection. The organ data is presented as the mean ± SD with n = 4. The recovery found in the blood assumes a blood volume of 2.18 mL/25 g mouse.....	83
Figure 3.6	Blood pharmacokinetic profile of PRINT particles in healthy C57BL/6J mice. At given time intervals, four animals were sacrificed and blood was collected via cardiac puncture. Radioactivity observed was converted to particle concentration using the specific radioactivity measured and assuming a total blood volume of 2.18 mL/25 g mouse. The data was subject to two-compartmental analysis (WinNonlin) resulting in pharmacokinetic parameters discussed in the text. For simplicity, data obtained 24 h post-injection are not shown in the figure or used for PK parameter determination.....	85
Figure 4.1	Passive tumor targeting of PRINT nanoparticles by EPR effect.....	93
Figure 4.2	Scanning electron micrograph of 200 nm PRINT particles used in the present study.....	102
Figure 4.3	Dynamic light scattering of 200 nm PRINT particles that have been post-functionalized with PEG 5K and DyLight 800. The mean diameter was measured at 225 nm, with a polydispersity of 0.005.....	103
Figure 4.4	Zeta potential analysis of 200 nm PRINT particles. A) Purified particles before any post-functionalization (zeta potential = 33 ± 3 mV). B) Purified particles that have been post-functionalized with PEG 5K and DyLight 800 (zeta potential = - 26 ± 2 mV).....	104
Figure 4.5	<i>In vitro</i> internalization profiles of PEGylated 200 nm particles with a negative zeta potential using Ramos cells. Both the positively charged particle and negatively charged particle controls are included. Overall, the internalization of all particle sets was low.....	106

Figure 4.6	<i>In vitro</i> cytotoxicity profiles (MTS Assay) of PEGylated 200 nm particles with a negative zeta potential using Ramos cells.....	107
Figure 4.7	<i>In vitro</i> hemolysis assay of PEGylated 200 nm particles with a negative zeta potential using human blood. Here, the positive control is Triton-X 100, which is known to lyse red blood cells, and the negative control is poly(ethylene glycol) (MW = 8000 g/mol).....	108
Figure 4.8	Whole animal imaging on the IVIS-100 Xenogen imaging system. 200 nm PRINT particles were injected via the tail vein in nude mice bearing Ramos tumors. The major organs of accumulation (i.e. the liver and spleen) were visible as early as 10 minutes.....	109
Figure 4.9	Tumor growth rate as a function of time. 10^7 cells were injected subcutaneously into the right flank of nude mice. Experiments were conducted at day 14 post-inoculation, where the average tumor volume was 0.72 cm^3	109
Figure 4.10	Biodistribution of 200 nm PRINT particle in nude mice bearing Ramos tumors. The organ accumulation is expressed as a percent of recovered dose after animals were sacrificed at 10 min, 1 h, and 6 h post-intravenous injection. The organ data is presented as a mean \pm SD with n=4.....	111
Figure 4.11	Organ distribution of 200 nm (AR = 1) PRINT particles (A) versus the PBS control (B). Organs were excised from both animal groups at 6 h post-injection.....	112
Figure 4.12	The effect of dosage as a function of percent recovered dose at 6 h post-injection.....	115
Figure 4.13	The effect of dosage as a function of total fluorescence intensity at 6 h post-injection.....	115
Figure 4.14	Whole animal imaging on the IVIS-100 Xenogen imaging system as a function of dosage.....	116
Figure 5.1	<i>In vitro</i> internalization of cationically charged hex nut PEG hydrogel particles by confocal microscopy....	128

Figure 5.2	<i>In vitro</i> internalization of cationically charged hex nut PEG hydrogel particles by transmission electron microscopy.....	129
Figure 5.3	<i>In vitro</i> examination of cationically charged hex nut PEG hydrogel particles by scanning electron microscopy.	130
Figure 5.4	Fluorescent micrographs of 2 μm (AR = 3) PEG hydrogel end-functionalized particles. These particles contain fluorescein- <i>o</i> -acrylate in the particle matrix, and have been end-functionalized with NHS-rhodamine. A) Particles coming off the sacrificial adhesive layer, and B) Purified particles dispersed in an aqueous solution.....	133
Figure 5.5	Confocal micrographs of 2 μm x 2 μm x 6 μm PEG hydrogel end-functionalized particles interacting with HeLa cells. These particles contain fluorescein- <i>o</i> -acrylate in the particle matrix, and have been end-functionalized with NHS-rhodamine. In all cases observed, the positively charged end of the particle interacted with the negatively charged membrane of the cells....	134
Figure 5.6	Fluorescent micrographs of hex nut PEG hydrogel end-functionalized particles. These particles contain fluorescein- <i>o</i> -acrylate in the particle matrix, and have been end-functionalized with NHS-rhodamine. A) Particles coming off the sacrificial adhesive layer, and B) Purified particles dispersed in an aqueous solution....	135
Figure 5.7	The effect of modulus on circulating artificial red blood cells. A) SEM micrograph of rigid 7 μm particles (AR = 0.25, no porogen), B) the biodistribution of rigid 7 μm particles (AR = 0.25, no porogen), C) SEM micrograph of flexible 7 μm particles (AR = 0.25, 50 wt% porogen), D) the biodistribution of flexible 7 μm particles (AR = 0.25, 50 wt% porogen).....	138

LIST OF ABBREVIATIONS

ADA	adenosine deaminase
AEM	2-aminoethyl methacrylate hydrochloride
ATP	adenosine triphosphate
AR	aspect ratio
AUC	area under the curve
CHOL	cholesterol
CO ₂	carbon dioxide
Cyto D	cytochalasin D
d	diameter
DEAP	diethoxyacetophenone
DLS	dynamic light scattering
DMF	dimethyl formamide
DMSO	dimethyl sulfoxide
DNA	deoxyribonucleic acid
DOG	2-deoxyglucose
DPBS	Dulbecco's phosphate buffered saline
DSPC	1,2-Distearoyl- <i>sn</i> -Glycero-3-Phosphocholine
EPR	enhanced permeability and retention effect
g	gram
GCSF	granulocyte colony-stimulating factor
h	height
HCF	hepatocyte growth factor

HCl	hydrochloric acid
HIV	human immunodeficiency virus
i.m.	intramuscular
i.r.	intravitreal
IRIV	immunopotentiating reconstituted influenza virus
i.t.	intrathecal
i.v.	intravenous
kDa	kiloDalton
kg	kilogram
Li	lithium
m β CD	methyl- β -cyclodextrin
mCi	milliCurie
MEM	minimum essential medium
mg	milligram
μ L	microliter
mL	milliliter
μ m	micrometer
M _n	number average molecular weight
MW	molecular weight
NaN ₃	sodium azide
NHS	N-hydroxy succinimide ester
nm	nanometer
PBS	phosphate buffered saline

PDMS	poly(dimethyl siloxane)
PEG	poly(ethylene glycol)
PET	poly(ethylene terephthalate)
PFB	plasma free hemoglobin
PFPE	perfluoropolyethers
PK	pharmacokinetic
PLA	poly(D-lactic acid)
PLGA	poly(lactide-co-glycolide)
PPY	poly(pyrrole)
PRINT	Particle Replication In Non-wetting Templates
PTFE	poly(tetrafluoroethylene)
RES	Recticulo-Endothelial System
RNA	ribonucleic acid
s.c.	subcutaneous
SEM	scanning electron microscopy
TEM	transmission electron microscopy
TGA	thermogravimetric analysis
THF	tetrahydrofuran
UV	ultra violet
VEGF	vascular endothelial growth factor
wt %	weight percent

CHAPTER 1

NANOPARTICLES IN MEDICINE

1.1 Nanoparticle therapeutics

Nanotechnology can be defined as technology that is developed at the atomic, molecular, or macromolecular scale, where at least one dimension is measured in the nanometer range [1]. This size range (from 1-1000 nanometers) allows for the creation and use of structures, systems and devices that have novel properties with atomic-level control. The application of this type of fine control in the field of medicine is known as nanomedicine [2]. The development of nanoparticle therapeutics has given rise to an emerging modality in the diagnosis and treatment of cancer. Currently, there are 24 nanoparticle therapeutics that have been approved for clinical use [3]. To date, clinical applications of nanoparticle therapeutics have been dominated by liposomal and polymeric platforms (Figure 1.1).

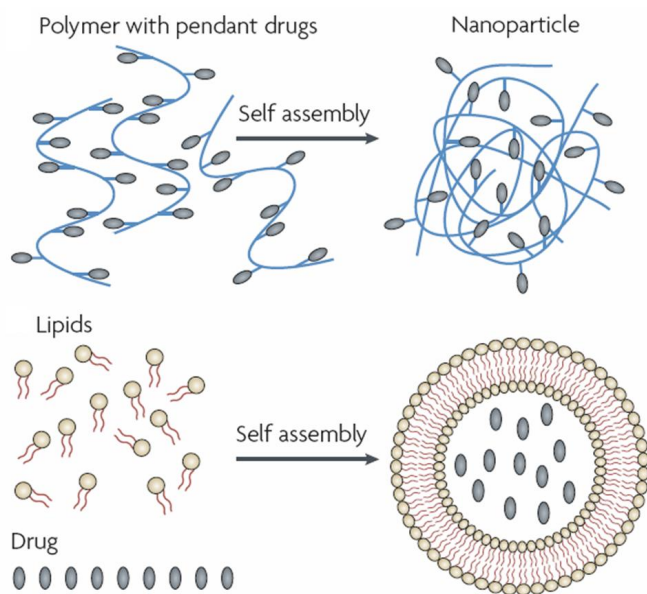


Figure 1.1 Common nanoparticle-based therapeutics approved for clinical use. Adapted from [4].

Liposomes, and more broadly, micelles, have been produced by a range of both natural and synthetic amphiphilic polymers leading to nano-scale structures. The use of liposomes in medical applications has received a great deal of attention in recent years. These membrane structures, composed of a phospholipid bilayer surrounding an aqueous or hydrophilic core, show exceptional biocompatibility and thus a great potential for clinical use as pharmaceutical carriers, particularly in the treatment of cancer. Indeed, several liposome-based drugs are already on the market such as Doxil®, AmBisome®, and DaunoXome® (Table 1.1). Liposomal delivery vehicles have several advantages over traditional cancer therapeutics in that they can encapsulate the therapeutic and/or diagnostic agent within the liposome core, thereby protecting the cargo from degradation. One of the most crucial advantages of these types of carriers lies in their ability to deliver hydrophobic drugs, thereby overcoming drug solubility issues which are commonly associated with the most powerful small molecule chemotherapeutics known. Liposomal delivery agents can be functionalized with biocompatible polymers such as poly(ethylene glycol) (PEG) to facilitate increased circulation times *in vivo* [5,6]. In this way, liposomes can take advantage of the enhanced permeability and retention (EPR) effect, a phenomenon that is a result of the leaky vasculature present in solid tumors arising from the rapid development of the tumor tissue [7,8]. The EPR effect is observed with macromolecules as they pass through the leaky tumor vasculature and are retained in the tumor due to the poor, underdeveloped lymphatic drainage observed in that tissue. Furthermore, the periphery of liposomes

can be modified with targeting ligands in an effort to increase the localization of these particles into the desired cells, tissues, and organs.

Additional directions in the search for the ideal organic nanoparticle include the design and synthesis of polymer conjugates. Polymer–drug conjugates are hybrid structures that tend to be water soluble (due to the control of the chemical composition of the polymer), can be tumor specific via the EPR effect, and tumor targeting ligands can decorate the polymer portion of the conjugate. These moieties have shown that they can be captured by cellular internalization [9,10]. The typical synthetic strategy for the fabrication of polymer-conjugates has involved the modification of polymer chain ends after polymerization to form reactive end groups. Several polymer conjugates have been approved for clinical use, such as Genexol-PM®, Neulasta®, and Renagel® (Table 1.2). In addition to the traditional liposomal and polymeric nanoparticle-based therapeutics, there are a small number of other platforms that have made it to the clinic (Table 1.3).

Nanoparticle Therapeutic (Company)	Platform	Disease	Administration Route
Abelcet (Enzon)	Liposomal amphotericin B	Fungal Infections	i.v.
AmBisome (Gilead Scieces)	Liposomal amphotericin B	Fungal and protozoal infections	i.v.
DepoCyt (SkyePharma)	Liposomal cytarabine	Malignant lymphomatous meningitis	i.t.
DaunoXome (Gilead Sciences)	Liposomal daunorubicin	HIV-related Kaposi's sarcoma	i.v.
Myocet (Zeneus)	Liposomal doxorubicin	Combination therapy with cyclophosphamide in metastatic breast cancer	i.v.
Epaxal (Berna Biotech)	Liposomal IRIV vaccine	Hepatitis A	i.m.
Inflexal V (Berna Biotech)	Liposomal IRIV vaccine	Influenza	i.m.
DepoDur (SkyePharma, Endo)	Liposomal morphine	Post-surgical analgesia	Epidural
Visudyne (QLT, Novartis)	Liposomal Verteporfin	Age-related macular degeneration, pathological myopia, ocular histoplasmosis	i.v.
Doxil/Caelyx (Ortho Biotech, Scehring- Plough)	Liposome-PEG doxorubicin	HIV-related Kaposi's sarcoma, metastatic breast cancer, metastatic ovarian cancer	i.m.
Estrasorb (Novavax)	Micellular estradiol	Menopausal therapy	Topical

Table 1.1 Clinically approved liposomal therapeutics. Adapted from [3].

[HIV, human immunodeficiency virus; i.m., intramuscular; IRIV, immunopotentiating reconstituted influenza virosome; i.t., intrathecal; i.v., intravenous; PEG, poly(ethylene glycol)]

Nanoparticle Therapeutic (Company)	Platform	Disease	Administration route
Copaxone (TEVA pharmaceuticals)	L-Glutamic acid, L - alanine, L -lysine, and L -tyrosine	Multiple sclerosis	s.c.
Genexol-PM (Samyang)	Methoxy-PEG-poly(D, L- lactide)	Metastatic breast cancer	i.v.
Adagen (Enzon)	PEG-adenosine deaminase	Severe combined immunodeficiency disease associated with ADA deficiency	i.m.
Macugen (OSI Pharmaceuticals)	PEG-anti-VEGF aptamer	Age-related macular degeneration	i.r.
Pegasys (Nektar, Hoffman- LaRoche)	PEG- α -interferon 2a	Hepatitis B, hepatitis C	s.c.
Neulasta (Amgen)	PEG-GCSF	Neutropenia associated with cancer chemotherapy	s.c.
Somavert (Nektar, Pfizer)	PEG-HGF	Acromegaly	s.c.
Oncaspar (Enzon)	PEG- L -asparaginase	Acute lymphoblastic leukemia	i.v., i.m.
Renagel (Genzyme)	Poly(allylamine hydrochloride)	End-stage renal disease	Oral

Table 1.2 Clinically approved polymeric therapeutics. Adapted from [3].

[ADA, adenosine deaminase; GCSF, granulocyte colony-stimulating factor; HGF, hepatocyte growth factor; i.m., intramuscular; i.r., intravitreal; i.v., intravenous; PEG, poly(ethylene glycol); s.c., subcutaneous; VEGF, vascular endothelial growth factor]

Nanoparticle Therapeutic (Company)	Platform	Disease	Administration route
Abraxane (Abraxis BioScience, AstraZeneca)	Albumin-bound paclitaxel	Metastatic breast cancer	i.v.
Emend (Elan, Merck)	Nanocrystalline aprepitant	Antiemetic	Oral
Tricor (Elan, Abbott)	Nanocrystalline fenofibrate	Anti-hyperlipedemic	Oral
Rapamune (Elan, Wyeth Pharmaceuticals)	Nanocrystalline sirolimus	Immunosuppressant	Oral

Table 1.3 Clinically approved nanoparticle-based therapeutics. Adapted from [3].
[i.v., intravenous]

1.2 Development of optimal nanoparticles for therapeutic applications

Beyond the ability of nanoparticles to take advantage of the EPR effect for passive tumor targeting, there are several additional features of nanoparticle therapeutics for cancer treatment that distinguish them from current approaches [4].

1.2.1 Nanoparticle size

Engineered nanoparticles allow for the careful control of size, shape and surface properties. Altering any of these particle design parameters can have a dramatic effect on circulation half lives *in vivo*. The ideal size of nanocarriers useful in nanomedicine is defined by several biological thresholds. First the lower bound of ~10 nm (diameter) is defined by renal filtration [11]. This is the threshold for first pass elimination by the kidneys. The upper bound is not as clearly defined, and is likely tumor dependent. Based on research looking into the EPR effect, it can be

estimated that the open interendothelial junctions are $< 1\ \mu\text{m}$. Some early work with liposomes and tumor xenograft models have suggested a cut-off of roughly 400 nm [12]. Therefore, it can be estimated that the ideal nanocarrier should be between 10 and 400 nm in diameter. An advantage of the large size of nanoparticles is that they have the ability to carry a large payload and protect that cargo from degradation while in circulation. Moreover, the cargo is generally located inside the particle matrix, and thus does not affect the pharmacokinetics or biodistribution profile of the nanocarrier. A new layer of sophistication can be designed into nanoparticles as they have the capacity to encapsulate multiple types of drug molecules.

1.2.2 Nanoparticle shape

The majority of nanocarriers that have been approved for clinical use or are in clinical trials are spherical in shape. Recent literature has suggested that spherical moieties may not be the optimal shape for nanomedicine [13-15]. Since the spherical shape of liposomes and polymer conjugates are determined by external forces, obtaining nanocarriers from these types of platforms that are non-spherical has proven difficult. Discher et al. examined the *in vivo* properties of filamentous micelle structures, called filomicelles (diameter = 22-60 nm, length = 2 – 18 μm), and compared that to spherical micelles having similar chemistry [13]. They discovered that the non-spherical filomicelles persisted *in vivo* much longer than their spherical counterparts, and were effective at delivering paclitaxel to human-derived tumors in mice. This study emphasized the role of vehicle geometry in nanomedicine. The

role of shape has been further examined using theoretical approaches. Decuzzi and co-workers have used theoretical models to determine the ideal shape of nanoparticles for use in medicine [16,17]. Here, it was found that spherical particles having a diameter of 100 nm show the lowest likelihood of encountering the conjugate antigen on the target endothelium. Non-spherical particles are much more likely to be found near the capillary walls and adhere to the target cancer cells. In these studies, spherical particles showed the worst chance of penetrating vascular fenestrations, which is commonly exploited for tumor accumulation of nanoparticles via the EPR effect. In addition, deviations from the typical spherical shapes towards disk and cylindrical particle shapes have the added advantage of being able to carry larger payloads. These findings suggest that shape may play an important role in the efficiencies of nanoparticle therapeutics.

1.2.3 Surface properties

The addition of biocompatible polymers, such as PEG, on the surface of nanoparticles can function to add stability to the nanoparticle dispersions, and can also act to increase circulation times *in vivo*. Moreover, nanoparticles have the ability to actively target tumor tissue through the covalent addition of multiple targeting ligands on the particle surface (Figure 1.2). These targeting ligands selectively bind to cell-surface receptors predominantly seen on tumor cells. One unique characteristic of nanoparticles is that they can contain multiple targeting ligands and have the ability to control the density of targeting ligands on their surface. Another advantage of using nanoparticles is that targeting ligands with low affinities

for their cell surface receptors can now be included, as the density of targeting ligands can be finely controlled to ensure overall high targeting efficiencies. In addition, modern day nanoparticles allow for fine tuning of the matrix composition such that the release kinetics of the drug from the nanoparticles can be altered for optimal impact. With all of these favorable characteristics, it is clear that nanoparticles are well suited for application in cancer therapeutics.

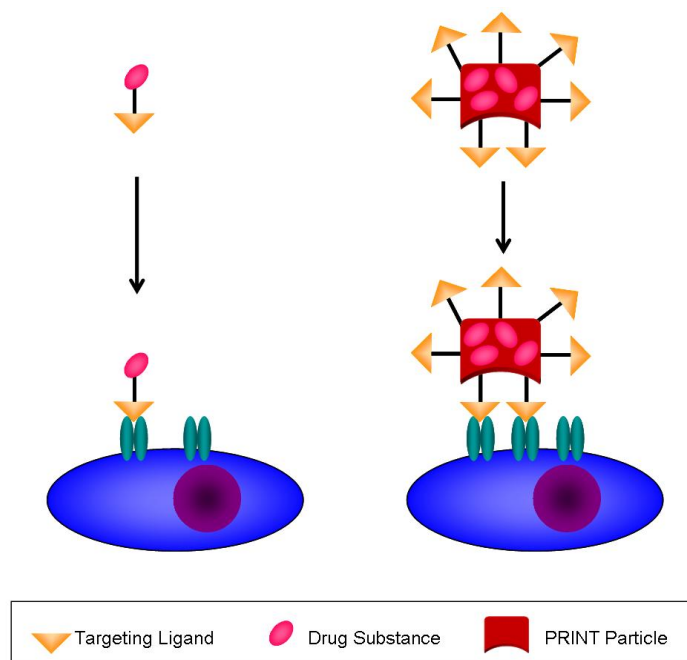


Figure 1.2 Ligand-receptor interactions on cancer cells. Molecular conjugates and multivalent particles are equally efficient at targeting when the surface density of the receptor is low. However, targeted nanoparticles are much more efficient at targeting cancer cells with the surface density of the receptor on the cancer cell is high (for example, the transferrin receptor). Adapted from [4].

1.3 Challenges with polymer conjugates as nanoparticle-based therapeutics

Polymer-conjugates offer additional alternatives in the field of nanomedicine but they also struggle with some challenges. For example, the conjugates need to be comprised of a high molecular mass, biodegradable polymeric matrix so they can better exploit the EPR effect. Also, the drugs to be delivered need to be covalently attached to the polymeric carrier, which sometimes requires a slight variant of the desired drug to facilitate such covalent conjugation. In addition, the linker between the drug and the carrier needs to be degraded to release the drug at the right time or in the desired location in order to optimize the efficacy of the system [18,19].

1.4 Challenges with liposomes as nanoparticle-based therapeutics

To date, liposomes have proven to be among the most successful therapeutic delivery agents. Despite the many advantages posed by these nanoparticle-based systems, some significant challenges still exist. These include restricted payload size, lack of robustness, fast elimination from the blood, and accumulation in the liver. Additionally, these self-assembled structures are limited to spherical shapes and offer limited control over size and dispersity. Although liposomal vectors exhibit promising *in vitro* transfection efficiencies when used in gene therapy applications, they often exhibit poor *in vivo* pharmacokinetics profiles and formulation instability. The pharmacokinetics of the *in vivo* administration of cationic liposome–DNA complexes indicate that

the complexes are rapidly eliminated from plasma [20]. The elimination is triggered by serum opsonin protein binding to the vector followed by reticuloendothelial system uptake. Covalent addition of hydrophilic flexible polymers, such as PEG, to the surface of liposomes decreases protein binding, thereby increasing the *in vivo* circulation times. Many of these systems, however, still have unacceptable formulation stability. In addition to these contemporary delivery systems, the ability to incorporate a variety of imaging beacons that are both shape and site specific, while simultaneously monodisperse, has proven to be unattainable [21].

Additionally, liposomal systems can be very misleading probes since they are dynamic, constantly equilibrating, self-assembled entities whose shape and surface chemistry is ill-defined especially when placed into the biological milieu where equilibration reactions occur with naturally occurring lipidic membranes. Beyond liposomes, most all other nanoparticle systems that have been reported have essentially no ability to control the size or shape of particles in a defined way, thus making it difficult to determine the design rules for biodistribution or cellular internalization and intracellular trafficking [22]. In addition, there is no ability with liposomes and many traditional nanoparticle systems to systematically hold particle size and shape constant and iterate on the range of surface characteristics such as ligand type, spatial distribution of ligands and the stoichiometry of the ligands so as to understand the issues of multifunctional or multiplexed particles. On top of these shortcomings, there is certainly no way of using traditional particle or liposomal systems to better understand how a

deformable particle or object of precisely defined size, shape and surface chemistry can dynamically circumvent various biological barriers. Understanding the role that mechano-biology plays as a function of size, shape and surface chemistry certainly lies at the core of how biological “particles” like neutrophils and red blood cells navigate the barriers that confront them [23]. Ascertaining definitive biodistribution maps by utilizing precisely defined particle probes containing appropriate imaging beacons useful for quantification will undoubtedly lead to a set of rules that will be of immense use to science and to the application of nanocarriers for improved human health, treatment and diagnosis.

1.5 Imparting size, shape, and composition control of materials for nanomedicine

In an effort to impart ultimate control over particle size and shape to optimize nanoparticles for therapeutic applications, lithographic techniques have been employed. The top-down approach of imprint lithography offers an engineering alternative to produce monodisperse size- and shape-specific nanocarriers. However, the replication of submicron features is a challenging materials problem. The past few decades have witnessed the emergence of soft lithography as an important tool for low cost pattern replication on the micron and nanometer scale [24]. Imprint lithography refers to the patterning of materials such as polymers, organics, and biological molecules into continuous arrays of patterned features using molds made from either hard materials (quartz/glass, glassy polymers) or soft elastomeric materials to generate features that form on top of an interconnecting

flash layer [24-26]. The field of soft lithography describes the subset of imprint lithography where soft elastomeric materials are used as the stamping material. Soft lithography has traditionally been dominated by the elastomer poly(dimethylsiloxane), or PDMS [27,28]. Despite the advantage of PDMS for use in soft lithography, it has been shown to suffer from serious drawbacks including swelling in common organic solvents, and is known to leave cyclic silicone derivatives on surfaces being molded or patterned [29]. A recent breakthrough by Rolland *et al.* exploits the excellent solvent resistance and the inherent release properties of highly fluorinated perfluoropolyether (PFPEs) elastomers as an exceptional molding material [30]. The unique range of material properties of PFPE-based elastomers—chemical resistance, extremely low surface energy, high gas permeability, solvent resistance, high elastic recovery and good mechanical strength—translates into the ability of PFPEs to mold most organic and aqueous liquids to generate useful materials in the form of isolated particles, arrays of particles and arrays of patterned features for a number of applications in nanomedicine.

Embossing is the process of creating a three-dimensional image or design in paper and in ductile materials. It is typically accomplished with a combination of heat and pressure. Unlike embossing, PFPE-based molding opens up unique approaches that exploit wetting, partial wetting and non-wetting phenomena instead of relying on heat and pressure associated with traditional embossing approaches. The performance of PFPEs in soft lithography was first demonstrated using replica molds generated from master templates created at IBM's Almaden Research Center in California that had features with a width of

140 nm, a depth of ~50 nm and a separation of 70 nm. The molds cast using the PFPE-based fluoroelastomer materials maintained preservation of the nanoscale features of the patterned silicon wafer master. The features on the PFPE-based mold as determined by AFM had an average height of 51 nm, which was in excellent agreement with measured 54 nm height of the features in the silicon master [30]. As a result of the very low surface energy and high gas permeability of PFPE-based fluoroelastomers, materials are able to be molded by exploiting the ability to “dead end” fill recessed cavities in PFPE molds with a wide range of organic liquids. Depending on the exact details of how the filling process is completed (Figure 1.3), including the exact nature of the liquid to be molded, isolated particles, arrays of particles and arrays of patterned features can be uniquely fabricated using a combination of cavity filling and free meniscus coating concepts.

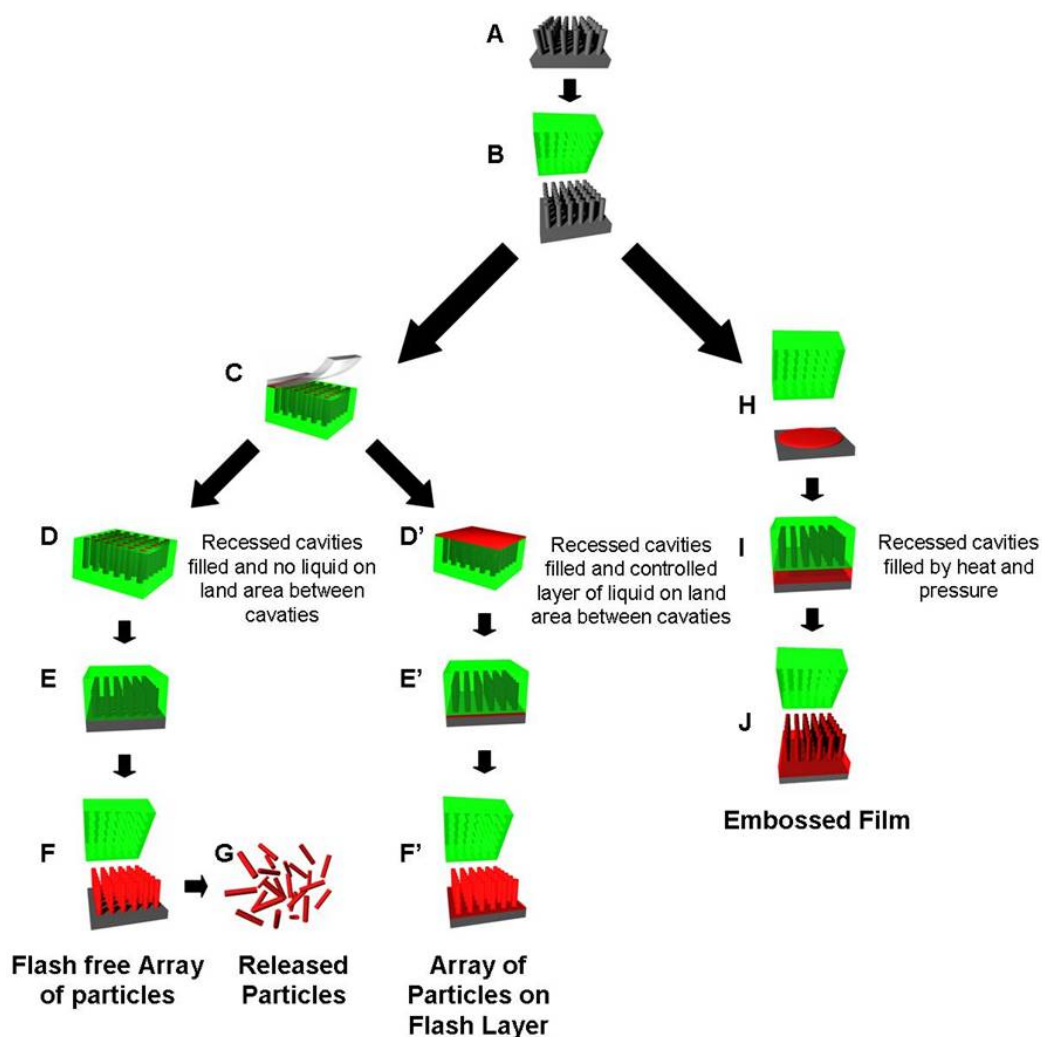


Figure 1.3 Schematic illustration of the PRINT process and traditional embossing processes: (A) Silicon master template; (B) mold release from master template; (C) mold filling via capillary fill with counter sheet having a higher surface energy than the PFPE mold. Depending on the exact nature of the liquid to be molded and the details of the process, (D) one can fill the cavities only and not wet the land area around the cavities or (D') one can fill the cavities and have a thin layer of liquid on the land area around the cavities. The thickness of the layer of connecting flash layer liquid is determined from the principles associated with free meniscus coating processes with the resulting (E and E') pattern transfer to substrate; (F and F') mold release from array of isolated features; and (G) dissolution of the harvesting film to yield free particles. As an alternative to PRINT, one can use PFPEs using traditional embossing processes where pressure and heat are applied (H and I) to form an embossed film (J) after the mold is removed.

In addition to the unprecedented resolution enabled by the use of PFPE-based materials in molding processes, recessed cavities within the PFPE molds can be filled with most organic and aqueous liquids without wetting the land area between the cavities (Figure 1.3). As such, once the liquid contained in the cavities is solidified, discrete objects in the mold can be achieved without the formation of the ubiquitous “flash” or “scum” layer. The flash layer is common to traditional embossing or soft lithography techniques where applied forces are used [22,30-32]. With PFPE-based molds, harvestable, flash-free objects, or particles can be fabricated using a process called PRINT (Particle [or Pattern] Replication In Non-wetting Templates). The PRINT process begins with the formation of a master template, typically an etched silicon wafer formed using advanced lithographic techniques (Figure 1.3A), which is coated with a photocurable liquid PFPE that is evenly distributed across the surface of the master template. Once the liquid fluoropolymer has completely wet the master template, it is photochemically crosslinked and subsequently peeled away to generate a precise mold having nanoscale cavities (Figure 1.3B). For the fabrication of 2-dimensional arrays of particles or free particles, the PFPE mold is filled with an appropriate liquid via capillary filling without wetting the land area around the cavities (Figure 1.3C). The liquid in the mold cavities is then converted to a solid using a wide range of methods including curing chemistries, evaporation, lyophilization, or liquid to solid phase transitions (Figure 1.3E, E'). The resultant particles can be removed from the mold and transferred to another surface to generate a 2-dimensional array or to yield free particles (Figure 1.3F, F', G). The key to making uniform particles of a specific

shape using PRINT is to have robust master templates that contain the repetitive features of interest. Currently, the repetitive features have sizes ranging anywhere from 70 nm to 500 μm , where the length can be varied in all three dimensions. The features are placed far enough apart so that sufficient room is left in between them in order to ensure enough space is available to manage excess liquid in the final PRINT process. This is also balanced with the goal of closely packing as many features into an area as possible to increase the throughput of PRINT. Using PRINT, features ranging in size from 2 nm to tens of microns have been fabricated, demonstrating the ability to accurately mold and replicate nanometer-scale features with a resolution of 0.4 nm [33].

PRINT is unique over the imprint lithography techniques promulgated by Whitesides *et al.* in that PRINT uses elastomeric fluoropolymers instead of silicones which results in three important distinctions: i) perfluoropolyether elastomers have a lower surface energy which enables the selective filling of nanoscale cavities in the mold with almost any organic liquid *without* wetting the land area around the cavities, enabling distinct objects or particles to be formed even at the micro- and nanoscale; ii) organic liquids do not swell fluoropolymers like they do silicones, allowing for the fabrication of a wide range of organic particles with desired attributes (surface chemistries, degradation characteristics, deformability) and iii) the TeflonTM-like characteristics of the fluoropolymer mold allow the resultant organic particles to be easily harvested or removed from the mold [24,27,34].

To demonstrate the scale-up possibilities with the PRINT process, a permanently etched master was made by transferring a repetitive, uniform shape

from an epoxy based resist onto a silicon wafer using conventional photolithography and reactive ion etching processes. The pattern, now permanently etched into the wafer with well resolved entities (Figure 1.4A), can be used repeatedly to make a large number of identical elastomeric PFPE replica molds by photochemically curing the dimethacrylate functionalized PFPE oligomer (Figure 1.4B) [30]. The PFPE replica molds were used to fabricate individual, monodisperse particles using the PRINT process (Figure 1.4C), which were then harvested to produce colloidal suspensions.

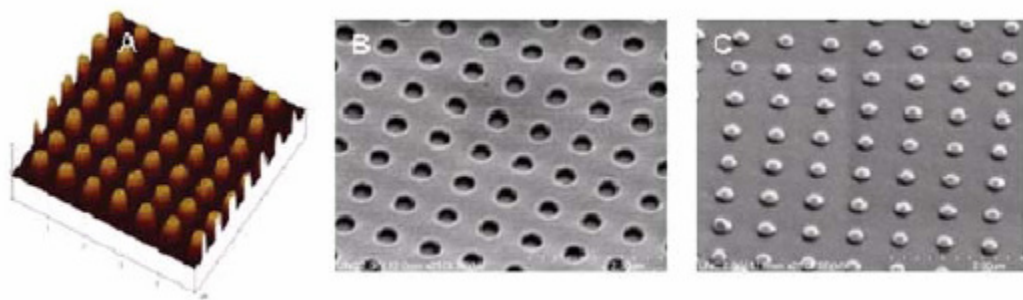


Figure 1.4 A) Atomic force micrograph of a 160nm post master; B) scanning electron micrograph of an unused, empty PFPE mold with 160 nm features (aspect ratio = 1: 1); and C) a scanning electron micrograph of harvested PEG-composite particles on the medical adhesive sacrificial layer.

To date, monodisperse particles from a wide range of particle matrix materials have been fabricated using PRINT. PRINT can be used to make such particles from poly (D-lactic acid) (PLA) and derivatives thereof such as poly(lactide-co-glycolide) (PLGA). It is well known that PLA and PLGA have had a considerable technological impact on the drug delivery and medical device industries because they are bioabsorbable and non-toxic [35]. Monodisperse

PLGA PRINT particles were fabricated by melt filling pre-formed PGLA polymers into 200 nm cavities of the PFPE mold (Figure 1.5).

Additionally, monodisperse, shape-specific 200 nm trapezoidal particles from poly(pyrrole) (Ppy) were generated. Ppy has been used in a variety of applications, ranging from electronic devices and sensors to cell-scaffolds [36]. The Ppy particles were fabricated in a one-step polymerization by placing a drop of a 1:1 v/v solution of THF: pyrrole and perchloric acid into the molding apparatus, followed by vacuum evaporation of the solvent. Monodisperse 200 nm Ppy trapezoidal particles were fabricated and harvested in an array (Figure 1.5).

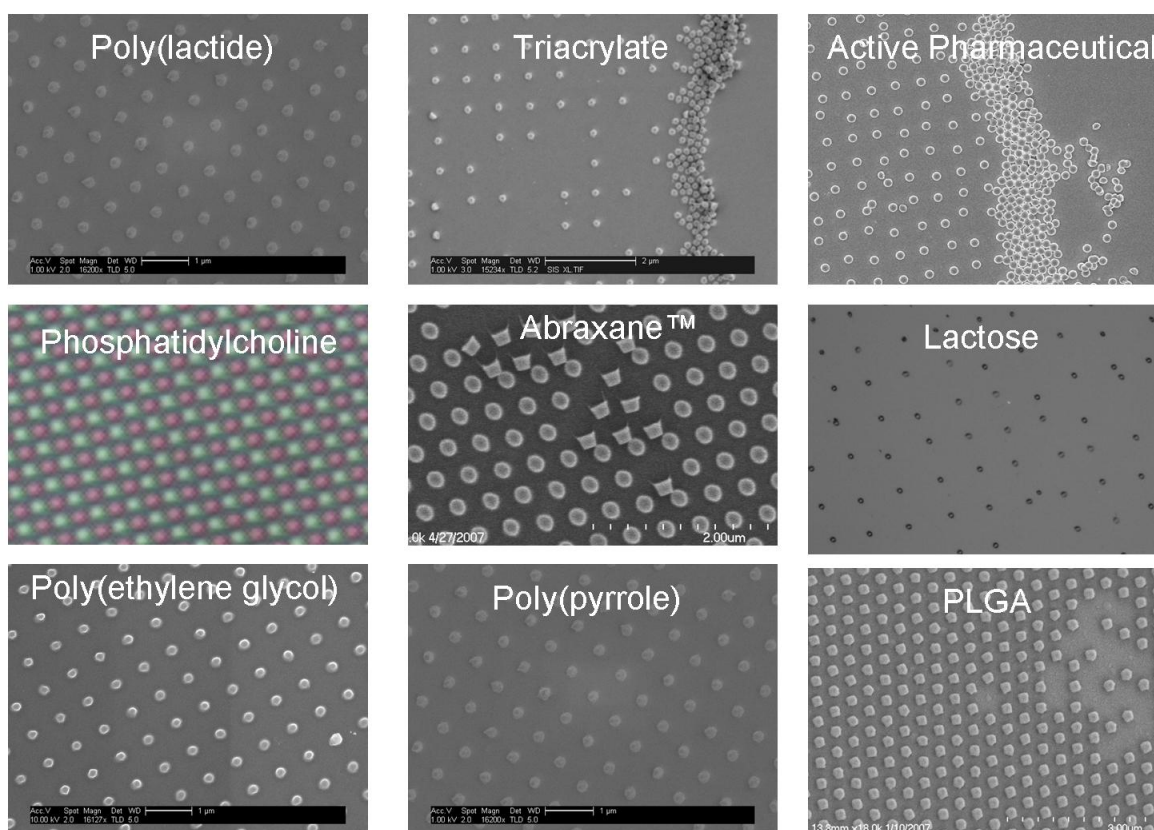


Figure 1.5 SEM micrographs of 200 nm monodisperse, shape-specific particles made from a wide range of materials; bioabsorbable, biocompatible, proteins and active pharmaceuticals.

As stated previously, PEG is a material of tremendous interest to the biotechnology community due to its commercial availability, non-toxic nature, and biocompatibility (Figure 1.5). PRINT can be used to produce monodisperse, nanometer and larger scale PEG particles in a wide range of compositions (e.g. with various crosslink densities of the hydrogel, with incorporation of cationically charged monomers, linking groups, etc.) by molding PEG-diacrylate liquid monomer followed by room temperature photopolymerization. Because the morphology of the particles is controlled by the master, it is possible to generate any of the aforementioned monomer systems into particles on a variety of length scales (Figure 1.6).

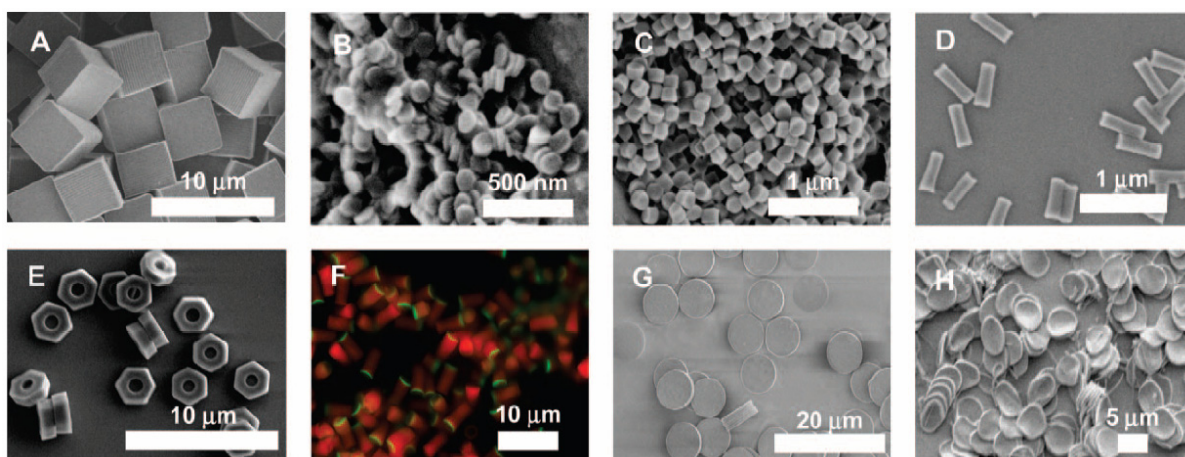


Figure 1.6 PRINT particles varying in size, shape, surface chemistry and deformability. The particle composition for all of these particles was approximately the same and included PEG (bulk of the matrix), a cross-linker, and a linker group for conjugation of stabilizing groups (such as PEG) or targeting ligands (such as peptides, antibodies, etc). A) Scanning Electron Micrograph (SEM) of cubic-shaped particles with a cube side length = 5 μm ; B) SEM of cylindrical nanoparticles having diameter = 110 nm and height = 35 nm; C) SEM of cylindrical nanoparticles having diameter = 200 nm and height = 200 nm; D) SEM of rod-like PRINT particles having diameter = 100 nm, height = 300 nm; E) SEM of 3 μm “hex nut” particles; F) Cylindrical PRINT particles containing a covalently attached red fluorophore that have been functionalized on one face with a generic linker group (green fluorophore) that will allow the conjugation of targeting peptides, antibodies and aptamers region-specifically onto the particle probes; G) and H) Particles for mechano-biology studies having approximately the same dimensions as red blood cells (cylinders with a diameter = 7 μm and a height of 1.7 μm made from (G) a non-deformable, highly cross-linked hydrogel; and (H) lightly cross-linked, deformable hydrogel.

By taking advantage of the delicate nature of PRINT, it is possible to incorporate a myriad of materials into the precursor PRINT solution prior to particle formation, including imaging contrast agents (superparamagnetic iron oxide particles), therapeutics (doxorubicin / paclitaxel / bortezomib), organic dyes (rhodamine), antibodies, proteins, and/or nucleic acids. These cargos may be encapsulated within the matrices of the PRINT particles and locked inside the particles once the particles are cured, or they can be pre-mixed with polymers

and incorporated into the particle matrix using the gentle, non-reactive methods for forming particles via solvent evaporation.

PRINT methodology is a versatile and flexible method for the direct fabrication and harvesting of monodisperse, shape-specific nano-biomaterials. Unlike other particle fabrication techniques, PRINT is delicate and general enough to be compatible with a variety of important next generation cancer therapeutic, detection and imaging agents, including various cargos (e.g. DNA, proteins, chemotherapy drugs, biosensor dyes, radio-markers, contrast agents), targeting ligands (e.g. antibodies, cell targeting peptides) and functional matrix materials (e.g. bioabsorbable polymers, stimuli responsive matrices, etc). PRINT is the first general, singular method capable of forming particles that: i) are monodisperse in size and uniform shape; ii) can be molded into any shape; iii) can be comprised of essentially any matrix material; iv) can be formed under extremely mild conditions; v) are amenable to post functionalization chemistry for the bioconjugation of targeting ligands; vi) and which initially fabricates particles in an addressable array (which opens up combinatorial approaches since the particles can be “bar-coded” using methods similar to DNA array technologies). In contrast to the present methods that utilize microfluidics techniques for particle fabrication, PRINT has the ability for more breadth of sizes (>100 nm) and is more amenable to scalability.

1.6 The future of nanomedicine

Nanomedicine will be extensively exploited in the clinic once a nanoparticle system attains targeted delivery of a therapeutic agent as well as localization of the therapeutic agent within the cell. Indeed, great progress has already been made toward this goal. For example, liposomal nanocarriers such as Doxil[®], AmBisome[®], and DaunoXome[®] are already in clinical use in lieu of their free-drug counterparts in part because they offer enhanced effectiveness and lower side effects.

As with any newly emerging technology, there are important questions that must be addressed as this technology progresses. For example, “what role does size and shape play on the biodistribution of these nanoparticles?” and, “how can size, shape and/or composition influence the efficacy of nanocarriers *in vivo*?” Perhaps most importantly, the questions regarding the safety of delivery of nanoparticles *in vivo* need to be investigated thoroughly due to the fact of complete control over dispersity in size and shape is now possible. Industry-wide, this need has been recognized as indicated by the formation of a voluntary program which aims at collecting data on existing nanomaterials and subsequently assessing their risks [37]. Strategies are being discussed to fully and consistently characterize all aspects of nanoparticles such as size, shape, dispersity, composition, surface chemistry and more [38]. Not only does such a strategy need to be reliably implemented, but researchers from across the scientific spectrum, from materials and engineering to pharmacology and

toxicology must fully collaborate to evaluate the safety and efficacy of these nanomaterials.

Nanotechnology brings exciting new possibilities to the field of medicine. One can envision nanocarriers that can be targeted to a specific tissue or cells to simultaneously detect and diagnose diseases as well as to treat them through the delivery of therapeutics. It is our expectation that nanomedicine will lead to more efficacious detection, diagnosis, and treatment of disease strategies than traditional methods in use today. The ideal nano-carrier will be one that is size- and shape-specific, has the ability to encapsulate fragile cargos, and has the flexibility to be functionalized with surface targeting ligands. Bottom-up approaches intrinsic to the synthesis of organic materials lack precise control over shape but offers excellent control over functionality. The top-down approach of microfluidics and photolithography can offer some shape control but with limited opportunities for shapes below 1 micron in size. Alternatively, the new emerging technique, PRINT combines some of the best elements from both bottom-up and top-down synthesis strategies, offering a highly versatile method for the production of isolated, monodisperse organic particles of nearly any size and shape that can contain delicate organic functional agents. The ability to exploit such control over nanoparticle properties makes these particles extremely promising for optimizing and manipulating therapeutics for a variety of disease applications.

1.7 References

- (1) Brydson, R. M.; Hammond, C. *Generic methodologies for nanotechnology: classification and fabrication*; Wiley: Chichester, UK, 2005.
- (2) Freitas, R. A. *Dm Disease-a-Month* **2005**, *51*, 325-341.
- (3) Zhang, I.; Gu, F. X.; Chan, J. M.; Wang, A. Z.; Langer, R. S.; Farokhzad, O. C. *Clinical Pharmacology & Therapeutics* **2008**, *83*, 761-769.
- (4) Davis, M. E.; Chen, Z.; Shin, D. M. *Nature Reviews Drug Discovery* **2008**, *7*, 771-782.
- (5) Lukyanov, A. N.; Elbayoumi, T. A.; Chakilam, A. R.; Torchilin, V. P. *Journal of Controlled Release* **2004**, *100*, 135-144.
- (6) Miller, C. R.; Bondurant, B.; McLean, S. D.; McGovern, K. A.; O'Brien, D. F. *Biochemistry* **1998**, *37*, 12875-12883.
- (7) Maeda, H. *Advances in Enzyme Regulation* **2001**, *41*, 189-207.
- (8) Maeda, H.; Wu, J.; Sawa, T.; Matsumura, Y.; Hori, K. *Journal of Controlled Release* **2000**, *65*, 271-284.
- (9) Vicent, M. J.; Duncan, R. *Trends in Biotechnology* **2006**, *24*, 39-47.
- (10) Malik, N.; Evagorou, E. G.; Duncan, R. *Anti-Cancer Drugs* **1999**, *10*, 767-776.
- (11) Choi, H. S.; Liu, W.; Misra, P.; Tanaka, E.; Zimmer, J. P.; Ipe, B. I.; Bawendi, M. G.; Frangioni, J. V. *Nature Biotechnology* **2007**, *25*, 1165-1170.
- (12) Yuan, F.; Dellian, M.; Fukumura, D.; Leunig, M.; Berk, D. A.; Torchilin, V. P.; Jain, R. K. *Cancer Research* **1995**, *55*, 3752-3756.
- (13) Geng, Y.; Dalhaimer, P.; Cai, S. S.; Tsai, R.; Tewari, M.; Minko, T.; Discher, D. E. *Nature Nanotechnology* **2007**, *2*, 249-255.
- (14) Gratton, S. E. A.; Ropp, P. A.; Pohlhaus, P. D.; Luft, J. C.; Madden, V. J.; Napier, M. E.; DeSimone, J. M. *Proceedings of the National Academy of Sciences of the United States of America* **2008**, *105*, 11613-11618.
- (15) Jiang, W.; Kim, B. Y. S.; Rutka, J. T.; Chan, W. C. W. *Nature Nanotechnology* **2008**, *3*, 145-150.
- (16) Decuzzi, P.; Gentile, F.; Granaldi, A.; Curcio, A.; Causa, F.; Indolfi, C.; Netti, P.; Ferrari, M. *International Journal of Nanomedicine* **2007**, *2*, 689-696.

- (17) Decuzzi, P.; Lee, S.; Bhushan, B.; Ferrari, M. *Annals of Biomedical Engineering* **2005**, 33, 179-190.
- (18) Greish, K. *Journal of Drug Targeting* **2007**, 15, 457-464.
- (19) Muggia, F. *Clinical Cancer Research* **1999**, 5, 7-8.
- (20) Xia, Y. N.; Whitesides, G. M. *Angewandte Chemie-International Edition* **1998**, 37, 551-575.
- (21) Bontempo, D.; Maynard, H. D. *Journal of the American Chemical Society* **2005**, 127, 6508-6509.
- (22) Euliss, L. E.; DuPont, J. A.; Gratton, S.; DeSimone, J. *Chemical Society Reviews* **2006**, 35, 1095-1104.
- (23) Chien, S. *Annual Review of Physiology* **1987**, 49, 177-192.
- (24) Xia, Y. N.; Rogers, J. A.; Paul, K. E.; Whitesides, G. M. *Chem. Rev.* **1999**, 99, 1823-1848.
- (25) Chou, S. Y.; Krauss, P. R.; Renstrom, P. J. *Science* **1996**, 272, 85-87.
- (26) Gates, B. D.; Xu, Q. B.; Stewart, M.; Ryan, D.; Willson, C. G.; Whitesides, G. M. *Chem. Rev.* **2005**, 105, 1171-1196.
- (27) Xia, Y. N.; Whitesides, G. M. *Angew. Chem. Int. Ed.* **1998**, 37, 551-575.
- (28) Whitesides, G. M.; Ostuni, E.; Takayama, S.; Jiang, X. Y.; Ingber, D. E. *Annual Review of Biomedical Engineering* **2001**, 3, 335-373.
- (29) Lee, J. N.; Park, C.; Whitesides, G. M. *Anal. Chem.* **2003**, 75, 6544-6554.
- (30) Rolland, J. P.; Hagberg, E. C.; Denison, G. M.; Carter, K. R.; DeSimone, J. M. *Angewandte Chemie-International Edition* **2004**, 43, 5796-5799.
- (31) Rolland, J. P.; Maynor, B. W.; Euliss, L. E.; Exner, A. E.; Denison, G. M.; DeSimone, J. M. *Journal of the American Chemical Society* **2005**, 127, 10096-10100.
- (32) Rolland, J. P.; Van Dam, R. M.; Schorzman, D. A.; Quake, S. R.; DeSimone, J. M. *Journal of the American Chemical Society* **2004**, 126, 2322-2323.

- (33) Maynor, B. W.; Larue, I.; Hu, Z.; Rolland, J. P.; Pandya, A.; Fu, Q.; Liu, J.; Spontak, R. J.; Sheiko, S. S.; Samulski, R. J.; Samulski, E. T.; DeSimone, J. M. *Small* **2007**, 3, 845-849.
- (34) Xia, Y. N.; Whitesides, G. M. *Annual Review of Materials Science* **1998**, 28, 153-184.
- (35) Dong, Y. C.; Feng, S. S. *Journal of Biomedical Materials Research Part A* **2006**, 78A, 12-19.
- (36) Curran, D.; Grimshaw, J.; Perera, S. D. *Chemical Society Reviews* **1991**, 20, 391-404.
- (37) Gaidos, S. *The Scientist* **2005**, 19, 29.
- (38) Powers, K. W. B., S. C.; Krishna, V. B.; Wasdo, S. C.; Moudgil, B. M.; Roberts, S. M. *Toxicological Sciences* **2006**, 90, 296.

CHAPTER 2

THE EFFECT OF PARTICLE DESIGN ON CELLULAR INTERNALIZATION PATHWAYS

2.1 Introduction

Definitive biodistribution maps that establish the interdependency of the size, shape and surface chemistry of nanoparticles *in vitro* and *in vivo* over length scales ranging from cells to tissues to the entire organism are needed by many different research communities. Environmental regulators, pulmonologists, oncologists, pharmaceutical scientists, toxicologists, cell biologists and dermatologists all need definitive answers related to particle biodistribution, particle permeability and transport using “calibration quality” particles. For example, fungal and bacterial pathogens are first and foremost recognized by their form or shape, however the complete understanding of the role and significance of that form and shape is largely lacking. Indeed, some rod-like bacterial pathogens, including the gram-negative bacteria *Salmonella*, *Shigella*, and *Yersinia* and the gram-positive bacterium *Listeria monocytogenes* can induce their entry into non-phagocytic mammalian cells [1]. As such, nanofabricated tools (e.g. precisely defined particles) hold significant promise to provide insight into the fundamentals of cellular and biological processes. These tools can also yield essential insights into the design of effective vectors for use in nanomedicine, especially for the design of nanoparticles for use as targeted therapeutics and imaging agents. Indeed, very little is known how the interdependency of size, shape and surface chemistry can influence the biodistribution, cellular internalization, and intracellular trafficking of micro- and nanoparticles.

The exploration and utilization of nanocarriers for the delivery of therapeutics *in vivo* has led to dramatic improvements in the efficacy of various therapies. Over

the past few years, intense research and development of novel platforms has resulted in drug delivery vehicles such as polymeric nanoparticles, micelles, immunoconjugates, DNA-polymer conjugates, dendrimers and liposomes [1-18]. These different vehicles have opened new avenues in the development of site-specific targeted drug delivery [4-6, 8-11, 19, 20]. Clinically, the success of these carriers has been limited by the lack of control over size, chemical composition, uniformity, cell targeting and ability to consistently load and release known amounts of cargo [14, 21, 22]. Additional challenges faced by liposomal and micellular structures include the fact that they are dynamic “assemblies” (they are not stable objects) and there is little control over size and shape, especially over time in the biological milieu [19, 23, 24]. In addition, there are many other naturally occurring lipidic membranes present *in vivo* which lead to fusion and membrane reorganization and therefore leakage of cargo. Moreover, it is difficult to dial in the amount of cargo that one can kinetically trap or encapsulate in liposomes and it is even more difficult to have a series of liposomal structures that can release the cargo at will in a controlled time frame. Indeed most liposomal systems do not allow one to systematically vary the percentage of the cargo that can be encapsulated. As a result, in order to study dose dependencies with liposomal systems, researchers are forced to accomplish such critical experiments by physically blending liposomes containing cargo with cargoless liposomes in order to vary the dose of drug at constant liposomal dosing. Controlling the composition, size, shape, functionality and stability both *in vitro* and *in vivo* of nanocarriers is critical to the design of a fully realized delivery vehicle.

Elucidating the mechanisms by which organic particles of controlled size, shape, site-specific surface chemistry, tunable particle matrix composition and tunable modulus undergo endocytosis is of great importance. Understanding the interdependent roles that size, shape and surface and matrix composition have is particularly important. Once mechanisms of internalization are established, it is then possible to use these findings to better engineer the intracellular release of specific cargos. This information, in combination with ongoing efforts to understand the biodistribution of shape controlled particles [25], will help to establish rules towards the rational design of nanocarriers for the effective *in vivo* delivery of various cargos, especially those cargos that need to be internalized into cells such as siRNA and antisense oligonucleotides. The major endocytic pathways used by cells, for example, clathrin-mediated, caveolae-mediated, or macropinocytosis play prominent roles in the uptake and intracellular trafficking of organic particles. Several reports have addressed the role of shape and size on cellular internalization, however, no particle fabrication techniques currently available have the ability to independently alter one variable at a time, and monitor the effect of each variable [10, 13]. These studies focus on extending emerging “top-down” fabrication techniques from the microelectronics industry for the facile synthesis of readily tailorable nanofabricated tools or particles that can allow for the attainment of detailed knowledge of the interdependent effect that key particle variables (such as size, shape, chemical composition and surface charge) have on cellular entry [14-16]. This study utilizes polymer and organic chemistry, biochemistry, and cell biology to investigate these mechanisms using a novel particle fabrication method called PRINT (Particle

Replication In Non-wetting Templates, Figure 2.1) [22, 26]. PRINT takes advantage of the unique properties of elastomeric molds comprised of a low surface energy perfluoropolyether network, allowing for the production of monodisperse, shape-specific particles from an extensive array of organic precursors [22, 25, 27]. Herein, we report the utilization of recent breakthroughs in the nanofabrication of polymeric particles to develop an effective platform delivery system for use in nanomedicine.

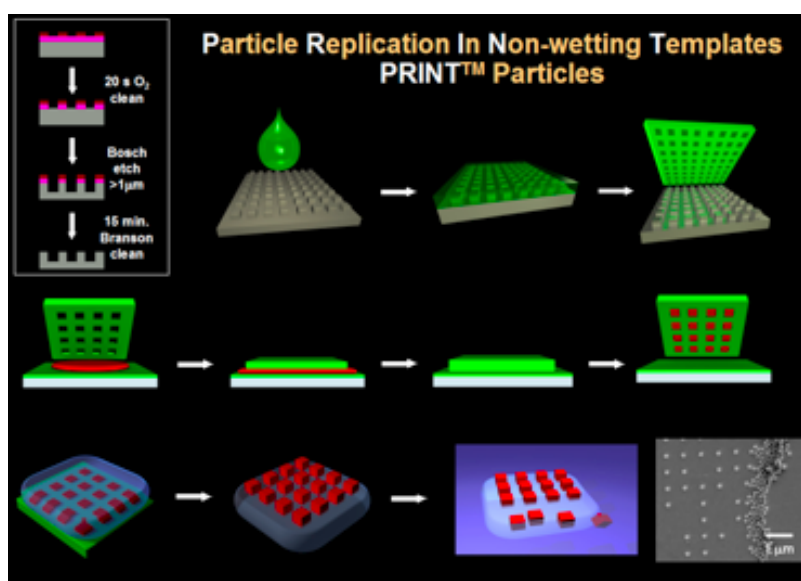


Figure 2.1 Illustration of PRINT. Fabrication of the silicon master template (box, upper left); Wetting of the silicon master with (green) liquid fluoropolymer, followed by curing (top row); PFPE elastomeric mold produced with nanoscale features from the master (upper right); Confining (red) organic liquid to cavities by applying pressure between mold and a PFPE surface (middle row); Removal of organic particles from mold with adhesive layer (bottom left); Dissolution of adhesive layer producing free particles (bottom right).

2.2 Experimental

2.2.1 Materials

FluorocurTM, the perfluoropolyether used as the molding material in the PRINT process, was purchased from Liquidia Technologies (Product # 2M-140). Trimethylolpropane ethoxylate triacrylate ($M_n = 428$ g/mol) (Aldrich), was passed through a short plug of alumina prior to use to remove inhibitor. Poly(ethylene glycol) monomethyl ether monomethacrylate ($M_n = 1,000$ g/mol) (Polysciences), fluorescein-*o*-acrylate (Aldrich), 2-aminoethyl methacrylate hydrochloride (Aldrich) and 2,2-diethoxyacetophenone (Aldrich) were used as received without further purification. Polyethylene sheeting was purchased from American Plastics Company. Solvents used in the fabrication and purification of PRINT particles (2-propanol, and acetone) were filtered before use through a 0.22 μ m PTFE syringe filter. Borax buffer was obtained from Ricca Chemical Company. HeLa, NIH 3T3 and RAW 264.7 cell lines were obtained from ATCC. The Lineberger Cancer Center Tissue Culture Facility, at the University of North Carolina Chapel Hill supplied the MCF-7 and OVCAR-3 cell lines. All cell culture media (MEM, OptiMEM) were purchased from the Lineberger Cancer Center Tissue Culture Facility at the University of North Carolina at Chapel Hill. Invitrogen supplied the GlutaMAX-I. Cell Titer 96® AQueous One Solution Cell Proliferation Assay was purchased from Promega. The 1.5G cover slips were obtained from MatTek Corporation, and DRAQ5 was purchased from Biostatus, Ltd.. Molecular Probes supplied the Alexa Fluor-555 labeled wheat germ agglutinin, and Polysciences supplied the Polybed 812 epoxy

resin. Nocodazole, methyl- β -cyclodextrin, Genistein, chlorpromazine, cytochlasin D, and sodium azide were obtained from Sigma-Aldrich. Dynasore was obtained from ChemBridge Corporation.

2.2.2 PRINT particle preparation

Briefly, 15 mL of FluorocurTM resin (Liquidia Technologies) containing 0.1% (w/w) of 2,2-diethoxyacetophenone was poured onto the silicon master template inside an enclosed UV chamber. The chamber was degassed with nitrogen for 2 minutes, then the coated wafer was exposed to UV irradiation ($\lambda = 365$ nm, power > 20 mW/cm²) for 2 minutes to cure the FluorocurTM resin. The elastomeric mold was then removed from the master template by gently peeling it away from the silicon surface.

In these experiments, the PRINT particles were derived from a mixture composed of 67 wt % trimethyloxypropyl ethoxylate triacrylate (MW = 428 g/mol), 20 wt % poly(ethylene glycol) monomethylether monomethacrylate (MW = 1,000 g/mol), 10 wt % 2-aminoethylmethacrylate hydrochloride (AEM·HCl), 2 wt % fluorescein-*o*-acrylate, and 1 wt % 2,2-diethoxyacetophenone (Figure 2.2, Table 2.1). A 10% (w/v) solution of this mixture in 2-propanol was prepared and then sprayed onto a FluorocurTM patterned mold using an air brush. A poly(ethylene) sheet (American Plastics Co.) was then placed over mold and peeled back at a rate of approximately 2.5 cm/min. Following this, the mold was placed in a UV curing chamber, purged with nitrogen for 2 minutes and UV irradiation was applied ($\lambda = 365$ nm, power > 20 mW/cm²) for 2 minutes.

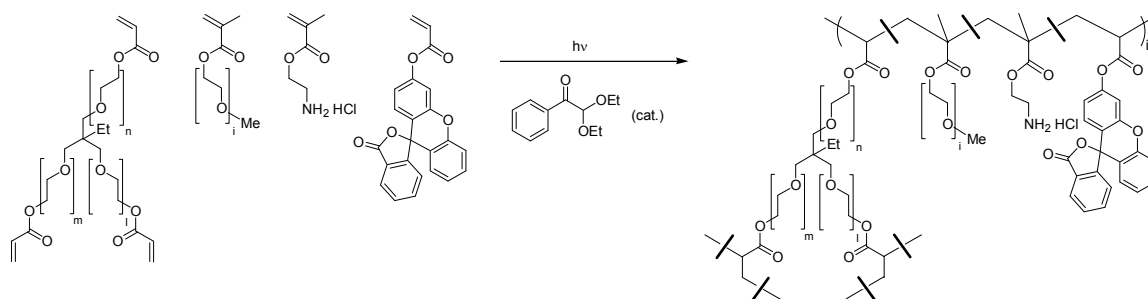


Figure 2.2 Chemical structures of monomers and a partial structure of the PRINT particles.

Monomer	Function	Wt %
PEG ₄₂₈ triacrylate	Cross-linking agent	67
PEG ₁₀₀₀ monomethylether monomethacrylate	Biocompatibility, Stability	20
2-Aminoethyl methacrylate hydrochloride	Chemical handle	10
Fluorescein-o-acrylate	Fluorophore	2
2,2-diethoxyacetophenone	Initiator	1

Table 2.1 Particle composition

A physical means for harvesting the particles was utilized by placing a 2 mL aliquot of acetone (filtered through a 0.22 μm PTFE filter) on the particle-filled mold. This drop of acetone was gently moved along the surface of the mold using a glass slide, facilitating release of the particles from the mold. The suspended particles were collected in a 50 mL Falcon tube, centrifuged using a IEC CENTRA CL2 Centrifuge (Thermo Electron Corporation), and rinsed with fresh acetone four times. The particles were then transferred to a tarred Eppendorf tube, and centrifuged in a microfuge (Fisher Scientific) for 20 minutes. The supernatant was removed, the

pellet was dried in a vacuum oven overnight, massed, and dispersed in the appropriate amount of sterile water to make a 10 mg/mL dispersion of particles.

2.2.3 Particle size analysis of PRINT particles using scanning electron microscopy

The size of PRINT particles was analyzed via scanning electron microscopy (Hitachi model S-4700). Particle dispersions were prepared at concentrations of 0.5 mg/mL, and a drop of this solution was placed on a glass slide. The drop was then allowed to dry, and the glass slide was coated with 1.5 nm of Pd/Au alloy using a Cressington 108 auto sputter coater (Cressington Scientific Instruments Ltd.). The Pd/Au coated glass slide was then adhered to the sample holder using double-sided adhesive tape, and placed inside the vacuum chamber of the SEM and observed under low vacuum (10^{-3} Torr).

2.2.4 Zeta potential measurements

The zeta potential of PRINT particles was measured using a ZetaPlus Zeta Potential Analyzer (Brookhaven Instruments Corporation). The particles were dispersed in water at a concentration of 0.3 mg/mL and the zeta potential was measured.

2.2.5 Cell lines and maintenance

HeLa cells were maintained in MEM supplemented with 10% FBS, 2 mM L-Glutamine, 1 mM sodium pyruvate and non-essential amino acids. NIH 3T3 and

RAW 264.7 cells were maintained in DMEM with 10% FBS, 4.5g/L glucose, 2 mM L-glutamine, and 110 mg/L sodium pyruvate. MCF-7 cells were grown in RPMI 1640 with 10% FBS, 2 mM L-glutamine, 1 mM sodium pyruvate, non-essential amino acids, and 10ug/mL insulin. OVCAR-3 cells were grown in RPMI 1640 supplemented with 10% FBS, 2 mM L-glutamine, 1 mM sodium pyruvate, 10 mM HEPES, 4.5g/L glucose, and 10 µg/mL human recombinant insulin.

2.2.6 Cell uptake and cytotoxicity assay – The effect of charge using 1 µm (AR = 1) particles

HeLa, MCF-7, OVCAR-3 and NIH 3T3 cells were seeded in 96 well plate at 2×10^4 per well, and RAW 264.7 cells were seeded at 5×10^4 per well. Cells were allowed to attach to the plate overnight at 37°C. The next day, 1 µm particles were vortexed and diluted in OPTI-MEM with GlutaMAX-I. Cells were briefly washed using OPTI-MEM with GlutaMAX-I and then dosed with particles for 4 hours (50 µL/well). The particles were removed at the end of dosing. For uptake assays, cells were washed with DPBS and trypsinized. Cells were then treated with 0.1% trypan blue at room temperature for 10 min to quench the extracellular fluorescence from non-internalized particles.[28] Finally, cells were washed and resuspended in DPBS and analyzed on a Cyan flow cytometer (DakoCytomation) with Summit 4.3 software. For the cytotoxicity assays, 100 µL of complete growth medium was replaced in each well, and 20 µL of Cell Titer 96® AQueous One Solution Cell Proliferation Assay reagent was added and incubated at 37°C until color was well developed. The adsorptions at 490 nm were taken for analysis.

2.2.7 *In vitro* cytotoxicity – The effect of size and shape

HeLa cells were seeded in 100 μL of media [Minimum Essential Medium (MEM) containing Earle's salts and supplemented with 1 mM sodium pyruvate and non-essential amino acids] at a density of 5×10^3 cells per cm^2 into a 96-well microtitre plate. Cells were allowed to adhere for 24 h before MEM was replaced with Opti-MEM (90 μL per well) and the particle preparation (10 μL per well in PBS). HeLa cells were incubated with the PRINT particles for 4 h or 72 h at 37 °C in a humidified 5% CO_2 atmosphere. After the incubation period, negative controls were prepared by the addition of 2 μL of lysis solution to a few wells containing cells only. After 2 minutes, the MTS assay solution was added (20 μL per well) into each well. The cells were then incubated for an additional 1 h at 37 °C in a humidified 5% CO_2 atmosphere. The optical density at 492 nm was measured using a BioRad Model 3550 microplate reader (BioRad Laboratories). The viability of the cells exposed to PRINT particles was expressed as a percentage of the viability of cells grown in the absence of particles.

2.2.8 Uptake experiments – The effect of size and shape

The HeLa cell line was employed to investigate the uptake of 5 μm , 3 μm , 2 μm cubic particles and 1 μm , 0.5 μm [aspect ratio (AR) = 2], 0.2 μm (AR = 1), 0.15 μm (AR = 3), and 0.1 μm (AR = 3) cylindrical particles. Particles were incubated with cells over a time course ranging from 15 minutes to 4 hours (37°C, 5% CO_2). Following cell/particle incubation, the cells were washed and detached by trypsinization. After centrifugation, cells were resuspended in a 0.4% trypan blue

(TB) solution in Dulbecco's Phosphate Buffers Saline solution (DPBS) to quench the extracellular FITC fluorescence [17]. This assay is based on the observation that the vital dye TB, while quenching the FITC fluorescence of a non-internalized particle, causes them to fluoresce red while an internalized particle will fluoresce green. Cells were then centrifuged, the TB solution was removed, the cell pellet was resuspended in DPBS, and sample was analyzed by flow cytometry (CyAn ADP, Dako), for green and red fluorescence. There were 10,000 cells measured in each sample.

2.2.9 Confocal laser scanning microscopy

HeLa cells (50,000) were seeded in a T-25 flask for 24 hours (37°C, 5% CO₂). Cells were washed once with D-PBS followed by MEM with supplements containing 1% fetal bovine serum (low serum). Cells were then incubated for 4 hours (37°C, 5% CO₂) with low serum MEM (2 mL) containing 15 µg/ml FITC-labeled PRINT nanoparticles. The cells were then washed by detachment with trypsin, resuspended in complete MEM containing 10% FBS, replated onto 2 35 mm² glass bottom dishes with 1.5G cover slips (MatTek Corporation) and allowed to adhere over night at 37°C. Nuclei were stained with 2.5 µM DRAQ5 (Biostatus Ltd) in complete MEM following the manufacturer's protocol. DRAQ5 is a DNA specific dye with far-red fluorescent properties (Ex: 647 nm, Em: 670 nm) [18] AlexaFluor-555 labeled WGA in D-PBS (2.5 µg/ml; Molecular Probes) was used to visualize plasma membranes. Cells were then fixed with 4% paraformaldehyde. Microscopy was carried out on an Olympus FV500 confocal laser scanning microscope (Olympus Co Ltd) located in the

Microscopy Laboratory Services, a core facility of the Department of Pathology and Laboratory Medicine within the UNC School of Medicine. Z stacks were collected and used for 3D reconstruction and visualization of intracellular particle localization.

2.2.10 Transmission electron microscopy (TEM)

TEM was carried out to further visualize the intracellular internalization and localization of PRINT nanoparticles. $\sim 5 \times 10^5$ HeLa cells were seeded in 60 mm² polystyrene dishes overnight. The following day, cells were treated with either 200 nm \times 200 nm, 1 μ m \times 1 μ m, or 150 nm \times 450 nm particles (15 μ g/mL in reduced serum MEM) for times indicated in the figure legend. Cell monolayers were rinsed with D-PBS and fixed in 2% paraformaldehyde/2.5% glutaraldehyde/0.15M sodium phosphate, at pH 7.4, for several hours or overnight. Following three rinses with sodium phosphate buffer, the monolayers were postfixed for 1 hour in 1% osmium tetroxide/1.25% potassium ferrocyanide/0.15M sodium phosphate buffer. After rinsing in deionized water, the cells were dehydrated using increasing concentrations of ethanol (30 %, 50 %, 75 %, 100 %, 100 %, 10 minutes each) and embedded in Polybed 812 epoxy resin (Polysciences, Inc.). The monolayers were sectioned parallel and perpendicular to the substrate at 70 nm using a diamond knife. Ultrathin sections were collected on 200 mesh copper grids and stained with 4% aqueous uranyl acetate for 15 minutes, followed by Reynolds' lead citrate for 7 minutes. Samples were viewed using a LEO EM910 transmission electron microscope operating at 80kV (LEO Electron Microscopy Inc.) located at the Microscopy Laboratory Services Core Facility. Digital images were acquired using a

Gatan Orius SC1000 CCD Digital Camera and Digital Micrograph 3.11.0 (Gatan, Inc.).

2.2.11 Inhibitor studies

HeLa cells (5×10^4) were seeded in a T-25 flask were treated with 0.1% NaN₃/ 50 mM 2-deoxyglucose, cytochalasin D (5 μ g /mL), Dynasore (80 μ M), or genistein (200 μ M) in serum-free MEM for one hour prior to incubation of particles (15 μ g/mL) with inhibitor in the fresh media for one hour at 37°C/5% CO₂. For the inhibitors methyl- β -cyclodextrin (m β cd) and chlorpromazine, cells were pre-incubated serum-free MEM containing either in 5 mM m β cd or 10 μ g/mL chlorpromazine for 15 minutes at 37°C/5% CO₂. The media was then changed to fresh media containing the inhibitors plus particles (15 μ g/mL) and further incubated for 30 min at 37°C/5% CO₂. Following exposure to particles and inhibitors for the desired time, the cells were washed with D-PBS and then trypsinized and processed for flow cytometry as described in the Uptake Experiments. All inhibitors were obtained from Sigma-Aldrich except for Dynasore which was obtained from ChemBridge Corporation.

2.3 Results and discussion

In the PRINT (Particle Replication In Non-wetting Templates) process (Figure 2.1), the permanent silicon master template is fabricated using advanced lithographic techniques. The liquid PFPE fluoropolymer is then added to the surface of the master template. A positive spreading coefficient allows the

perfluoropolyether to wet the nanoscale features of the master template with extremely high fidelity. After the fluoropolymer has wet the master template it is photochemically cross-linked and peeled away to generate a precise mold having nanoscale cavities. The low surface energy and high gas permeability of the PRINT mold enables the organic liquid precursor to the drug carrier particles to fill the cavities through capillary action, but it does not form an inter-connecting “flash” layer of liquid wetting the land area between the cavities. Such specific wetting and filling enables the fabrication of freestanding and harvestable particles that have the same precise shape of the silicon master template from which they were derived. Once the liquid in the mold cavities is converted to a solid using a wide range of gentle chemistries, the array of organic particles can be removed from the mold either by physical methods or by bringing the mold in contact with an adhesive layer (e.g. surgical adhesive/water soluble excipient layer). PRINT particles generally display a meniscus on one side of the particles, which is a direct result of the PRINT process where capillary action is used to fill the perfluoropolyether molds. Once the liquid in the PRINT molds is polymerized, the meniscus becomes a permanent part of the particle shape.

A series of particles were designed having varying sizes and shapes at a constant chemical composition (i.e. at a constant surface charge) using PRINT [17-19]. The PRINT micro- and nanoparticles were made from cationic, crosslinked poly(ethylene glycol) hydrogels and were designed to study the interdependent effect of size, shape and surface charge (zeta potential) on their internalization by human cervical carcinoma epithelial (HeLa) cells. Three distinct series of cationic

poly(ethylene glycol)-based particles were fabricated, a micron-sized series of cubic-shaped particles (cube side length = 2 μm , 3 μm , and 5 μm , Figure 2.3A-F), a micron-sized cylindrical series with identical heights but varying diameters (diameter = 0.5 μm , aspect ratio (AR) = 2 (Figure 2.3G), or diameter = 1 μm , AR = 1 (Figure 2.3H), and finally, a cylindrical-shaped nanoparticle series (diameter = 200 nm, AR = 1 (Figure 2.3I), diameter = 100 nm, AR = 3 (Figure 2.3J), diameter = 150 nm, AR = 3 (Figure 2.3K)). A characterization of the particle size (by SEM) and surface charge (by zeta potential) can be found in Table 2.2.

Particle Size	Height (μm)	Width (μm)	Zeta Potential (mV)
5 μm Cubes	4.60 ± 0.07	4.67 ± 0.20	$+26 \pm 3$
3 μm Cubes	2.50 ± 0.10	2.63 ± 0.09	$+21 \pm 3$
2 μm Cubes	1.56 ± 0.09	1.86 ± 0.04	$+21 \pm 3$
1 μm Cylinders (AR=1)	0.58 ± 0.05	0.90 ± 0.01	$+22 \pm 3$
0.5 μm Cylinders (AR=2)	0.38 ± 0.02	0.77 ± 0.09	$+32 \pm 3$
0.2 μm Cylinders (AR=1)	0.217 ± 0.006	0.159 ± 0.007	$+42 \pm 3$
0.15 μm Cylinders (AR=3)	0.479 ± 0.026	0.134 ± 0.026 (top)	$+35 \pm 3$
		0.159 ± 0.012 (bottom)	
0.1 μm Cylinders (AR=3)	0.277 ± 0.014	0.075 ± 0.003 (top)	$+41 \pm 3$
		0.118 ± 0.005 (bottom)	

Table 2.2 Particle size and surface charge characterization as determined by scanning electron microscopy and zeta potential measurements (respectively). Particle labels describe master cavity size.

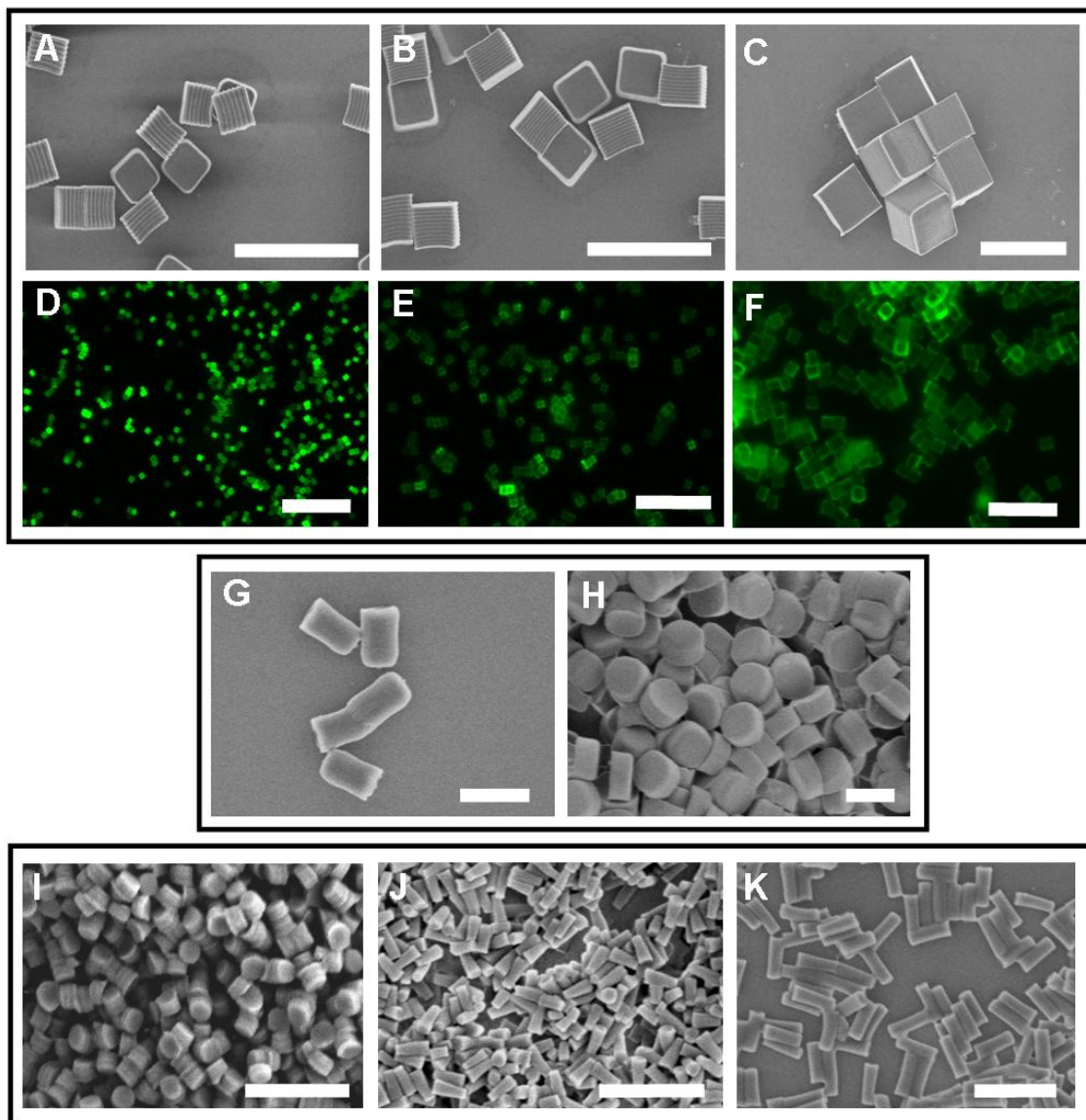


Figure 2.3 Micrographs of PRINT particles varying in both size and shape. Top Row (A-C) Scanning electron micrograph of the cubic series of particles {Diameters equal to 2 μm (A), 3 μm (B), and 5 μm (C)}. Second Row (D-F) fluorescence micrographs of the cubic series of particles {Diameters equal to 2 μm (D), 3 μm (E), and 5 μm (F)}. Third Row (G,H) Scanning electron micrographs of the cylindrical series of microparticles having the same height (1 μm), but varying diameters (Diameter = 0.5 μm (G) and 1 μm (H)). Last Row (I-K) Scanning electron micrographs of a series of cylindrical nanoparticles {Diameter = 200 nm, Height = 200 nm (I), diameter = 100 nm, height = 300 nm (J), diameter = 150 nm, height = 450 nm (K)}. Scale bars = 20 μm (A-F), 1 μm (G-K).

The cellular internalization of the three sets of particles was examined using HeLa cells, with particles being dosed at a constant particle mass (15 $\mu\text{g/mL}$). The kinetics of particle internalization were evaluated using a flow cytometry method in which internalized particles were differentiated from membrane-bound particles with a trypan blue fluorescence quench [17]. The time course of particle internalization was studied from 15 minutes to 4 hours (Figure 2.4). Cellular internalization of PRINT particles exhibited a strong dependence on particle size and shape. No significant internalization of the cubic particles with side lengths of 3 and 5 μm was seen in contrast to cubic particles with a side length equal to 2 μm which were significantly internalized by a large fraction of the cells. Cylindrical particles having diameters equal to 500 nm and 1 μm , both having heights of 1 μm , displayed similar internalization profiles, internalizing particles at a higher percentage ($\sim 75\%$) than cubic shaped 2 μm particles ($\sim 45\%$).

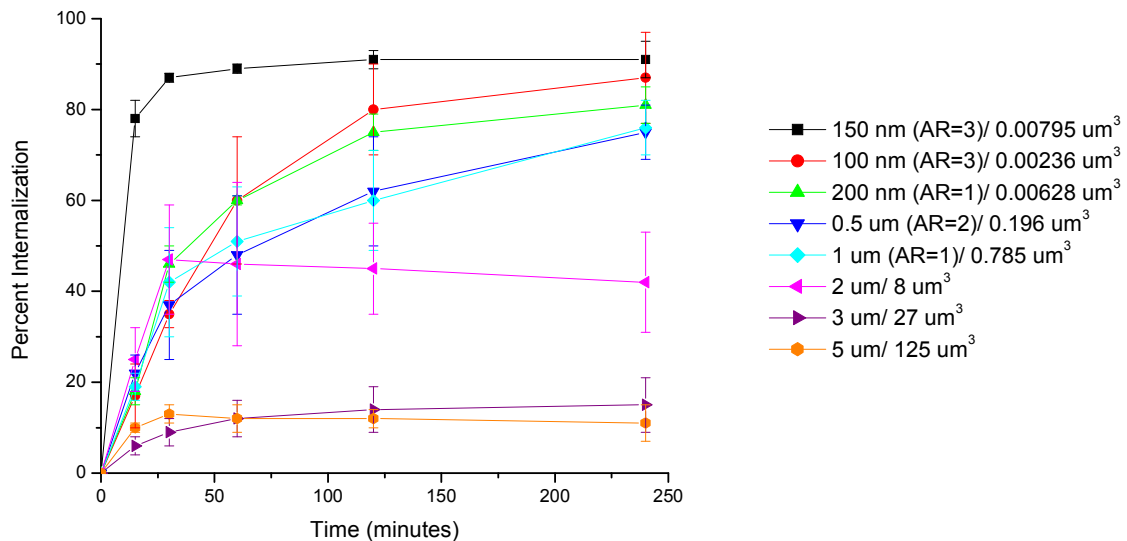


Figure 2.4 Internalization profile of PRINT particles with HeLa cells over a 4 hour time period at 37°C. Legend depicts the particle diameter/particle volume.

It was found that HeLa cells internalized all three nanoparticle shapes in the cylindrical series to a very high degree, however the kinetics of internalization were quite varied among the members of this series. While the low aspect ratio cylindrical particles having a diameter = 200 nm and a height = 200 nm and the high aspect ratio cylindrical particles having a diameter = 150 nm and a height = 450 nm have similar volumes ($6.3 \times 10^{-3} \mu\text{m}^3$ and $7.9 \times 10^{-3} \mu\text{m}^3$ respectively), their rates of internalization were quite different. The high aspect ratio particles ($d = 150 \text{ nm}$, $h = 450 \text{ nm}$) were internalized by HeLa cells approximately 4 times faster than the more symmetric low aspect ratio particles ($d = 200 \text{ nm}$, $h = 200 \text{ nm}$) (5.2 % of the cell population/min versus 1.2 % of the cell population/min). Cylindrical particles having a diameter of 100 nm, an aspect ratio of 3, and a volume of $2.4 \times 10^{-3} \mu\text{m}^3$ were internalized to a lesser extent than the larger cylindrical particles having a diameter of 150 nm with the same aspect ratio. The internalization kinetics of the nanoparticles by HeLa cells thus appears to be dependent not only on the effective rod-like character (aspect ratio) but also on the absolute size and/or volume of the particle. A possible explanation for this behavior could be attributed to the multivalent cationic interactions with cells that are available with the higher aspect ratio particles due to larger surface areas in contact with the cell membrane.

High molecular weight, positively charged polyelectrolytes such as poly(lysine) are known to exhibit cytotoxicity *in vitro* due to interactions between the polyelectrolytes and cell membrane phospholipids resulting in disruption of the cellular membrane structure [19, 20]. Therefore, the cytotoxicity of each particle

series was determined using the MTS cell viability assay (Figure 2.5). No toxicity was evident from the assays suggesting that cationic PRINT particles used in this study were non-toxic at the concentration ranges used in the study. Furthermore, as nanoparticles are likely candidates for *in vivo* studies, we evaluated the low aspect ratio cylindrical particles ($d = 200$ nm, $h = 200$ nm) for long term cytotoxic effects (72 h) (Figure 2.5) [21]. Even under extended incubation times, PRINT nanoparticles exhibited no cytotoxicity.

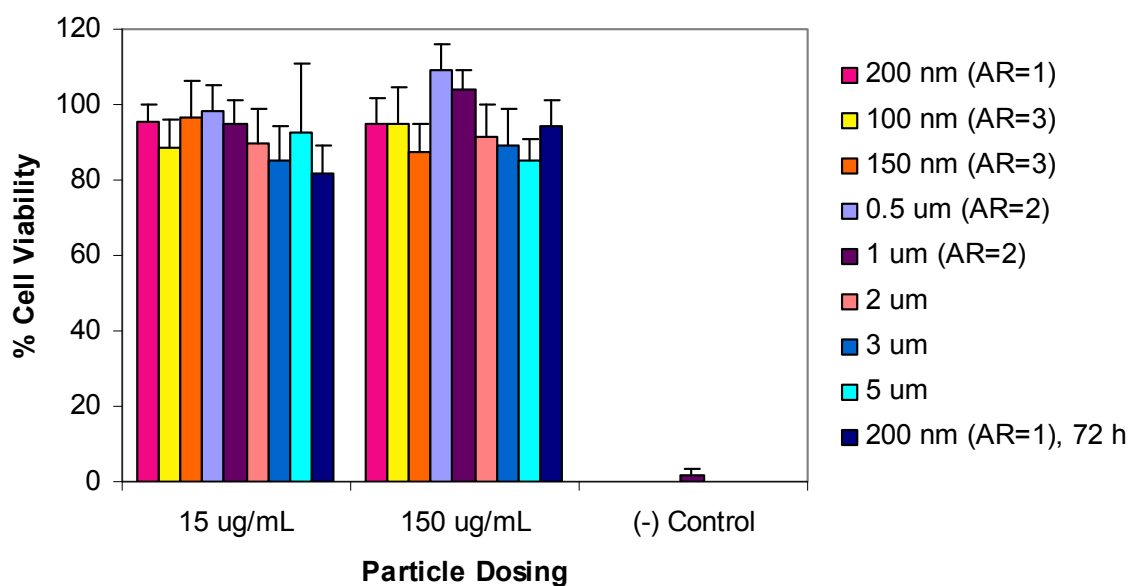


Figure 2.5 MTS Assay showing the cytotoxicity of all particles under investigation. All experiments were carried out with a 4 h incubation with HeLa cells, except the final bar, where the 200 nm particles were tested for cytotoxicity out to 72 hours.

The effect that charge has on cellular internalization pathways has been studied [32]. It has been shown that positively charged D,L-poly(lactide) particles are internalized into HeLa cells using clathrin-mediated pathways whereas negatively charged D,L-poly(lactide) particles do not utilize the clathrin-mediated endocytotic

pathway. Despite this study, little is known about the mechanism of the endocytotic machinery involved with internalized non-spherical particles, especially as a function of size, as well as the intracellular trafficking that takes place with non-spherical particles. Dependence of surface charge on cellular internalization of PRINT nanoparticles was investigated using rapidly internalized high aspect ratio cylindrical nanoparticles ($d = 150 \text{ nm}$, $h = 450 \text{ nm}$). These particles were treated with acetic anhydride to passivate the surface amine groups, thereby changing the zeta potential from $+ 34.8 \pm 3.0 \text{ mV}$ to $- 33.7 \pm 2.3 \text{ mV}$ upon conversion of the protonated surface amine groups to amides (Figure 2.6). Here, the negatively charged particles have retained the exact shape of the positively charged particles used in these studies, which showcases the ease of transformations of the surface chemistry on PRINT particles. The charge effect on cellular internalization was dramatic. Positively charged nanoparticles were internalized in 84 % of cells after a 4 h incubation period whereas the identically shaped negatively charged particles were not internalized to any significant amount ($< 5 \%$), thus strongly suggesting that surface charge plays an important role in the cellular internalization of PRINT particles (Figure 2.6).

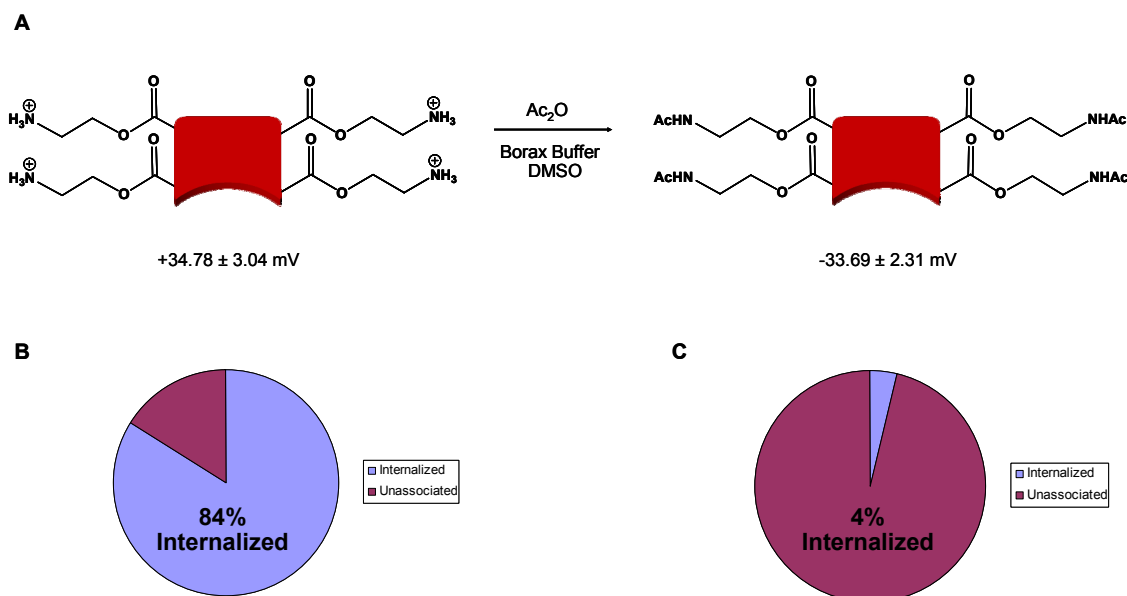


Figure 2.6 Effect of charge on cellular internalization. A) The chemical transformation, leading to changes in surface charge, B) Particle internalization after 4 hours of incubation with HeLa cells with *positively* charged particles C) Particle internalization after 4 hours of incubation with HeLa cells with *negatively* charged particles

To further elucidate the effect of charge on cellular internalization, a focused study on was conducted using 1 μm particles and multiple different types of cells. Treating the surface amine groups of the positively charged particles with acetic anhydride in Borax buffer changed the zeta potential from $+22 \pm 3 \text{ mV}$ to $-19 \pm 3 \text{ mV}$. In order to determine the effect of charge in multiple different cell lines, both positively and negatively charged 1 μm PRINT particles were dosed onto HeLa (human epithelial carcinoma), NIH 3T3 (mouse embryonic fibroblast), OVCAR-3 (human ovarian carcinoma), MCF-7 (human breast adenocarcinoma), and RAW 264.7 (mouse leukaemic monocyte macrophage) cells. Following several rinsing steps attempting to remove any membrane-bound or non-internalized particles, the

percent of cells with internalized particles was measured on a Dako flow cytometer. In these experiments, HeLa, NIH 3T3, OVCAR-3, and MCF-7 cells all displayed a decreased rate of endocytosis with the negatively charged particles when compared to the identically sized and shaped positively charged particles at all particle concentrations tested (up to 360 $\mu\text{g/mL}$, Figure 2.7). In contrast, the RAW 264.7 macrophage cells showed no preferential uptake of positively charged particles over the negatively charged particles. Specifically, it was found that at a particle concentration of 100 $\mu\text{g/mL}$, positively charged were internalized into $\sim 100\%$ of all the HeLa cells being analyzed, whereas only $\sim 60\%$ of the negatively charged particles were internalized at similar concentrations. When NIH 3T3 cells were investigated at the same particle concentration, a larger discrepancy was seen between the positively and negatively charged PRINT particles. Here, the positively charged particles were internalized by $\sim 100\%$ of the cells, while the negatively charged particles were only internalized by $\sim 40\%$ of the cells. In contrast, OVCAR-3 cells seemed to be less discriminatory, with $\sim 100\%$ of cells possessing an internalized positively charged particle, and $\sim 80\%$ of cells having an internalized negatively charged particle, both at particle concentrations of 100 $\mu\text{g/mL}$. An additional cancer cell line was examined, MCF-7 cells, which showed a more pronounced preference for the positively charged particles. In this case, at 100 $\mu\text{g/mL}$, $\sim 80\%$ of cells contained an internalized positively charged particle, whereas only $\sim 40\%$ of cells contained an internalized negatively charged particle. Finally, the macrophage cell line showed little, if any, effect of charge on particle internalization at all particle concentrations. For example, at 100 $\mu\text{g/mL}$ $\sim 85\%$ of

cells contained an internalized positively charged particle, and ~ 75 % of cells contained an internalized negatively charged particle.

In this series of experiments, both 1 hour and 4 hour particle incubation times were examined, with little difference in cellular internalization observed with increased incubation times. These results suggest that a targeted particle therapy could be achieved at the appropriate particle dosing levels (~ 15 µg/mL) using negatively charged particles with a targeting ligand thereby avoiding non-specific uptake and increasing targeting efficiencies into the desired cells.

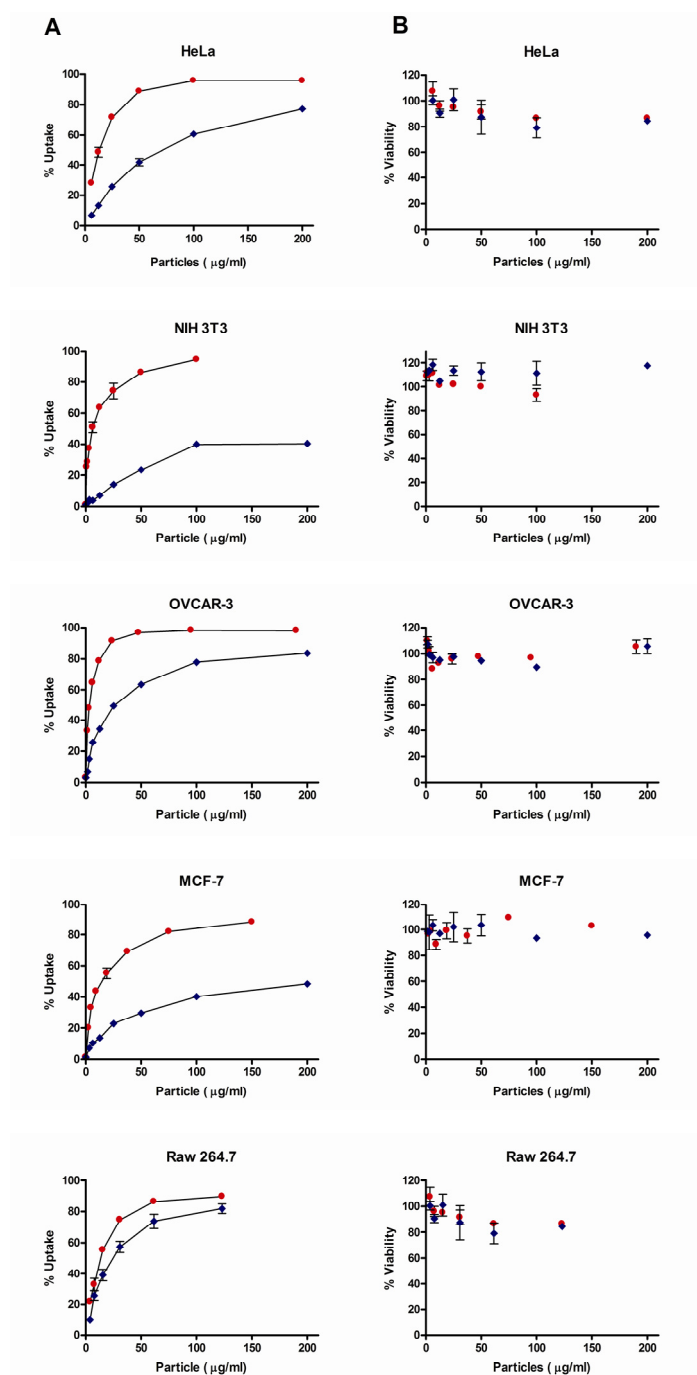


Figure 2.7 Internalization of 1 μ m PRINT particles by various cell lines. Cells were dosed with various concentrations of particles for 4 h at 37°C. (A) Cellular internalization profiles; (B) Cytotoxicity of particles. Red circles represent positively charged particles; blue circles represent negatively charged particles. The data shown were representative of more than three separate experiments.

Since it is known that positively charged particles can induce cytotoxic effects, all particles used in this study were examined for cytotoxicity. It is thought that positively charged particles can disrupt the cellular membrane through electrostatic interactions with the cell membrane phospholipids [33, 34]. Therefore, the cytotoxicity of the PRINT particles used herein was evaluated using HeLa, NIH 3T3, OVCAR-3, MCF-7, and RAW 264.7 cells after 4 hours of incubation with both positively and negatively charged 1 μm PRINT particles. In all five cell lines tested, no significant amount of cytotoxicity was observed (Figure 2.7). Moreover, no observable cell death was seen for particles having either positive or negative zeta potentials. However, several cells lines showed a slight decrease in cell viability with an increase in particle concentration, while remaining relatively non-toxic. For example, HeLa cells show a $\sim 12\%$ decrease in cell viability once both positively and negatively charged particle concentrations were increased to 200 $\mu\text{g/mL}$ and RAW 264.7 cells showed a decrease in cell viability ($\sim 13\%$) for both charged particles at concentrations of 125 $\mu\text{g/mL}$. For the remaining cell lines, i.e. NIH 3T3, OVCAR-3 and MCF-7, both surface charges showed no observable cell death at particle concentrations as high as 200 $\mu\text{g/mL}$. For all cell lines, cytotoxicity tests were performed with extended times (out to 72 hours), with no significant amount of cell death observed.

Further insight into the cellular internalization of the cationic hydrogel particles based on size and shape was gained by confocal microscopy (Figure 2.8). Monitoring particle internalization by confocal microscopy gave a more complete understanding of particle intracellular localization. Confocal micrographs revealed

that all internalized PRINT particles consistently migrated to the perinuclear region of the cells over time. Z series images were obtained and used to construct 3-D representations which clearly show that PRINT particles as large as 3 μm are internalized by HeLa cells, and that the particles ultimately translocate to the perinuclear region of the cell. These data are consistent with intracellular translocation of either endosomal and/or lysosomal vesicles from the plasma membrane along microtubules in the minus direction toward the centrosome/microtubule organizing center of the cell [23].

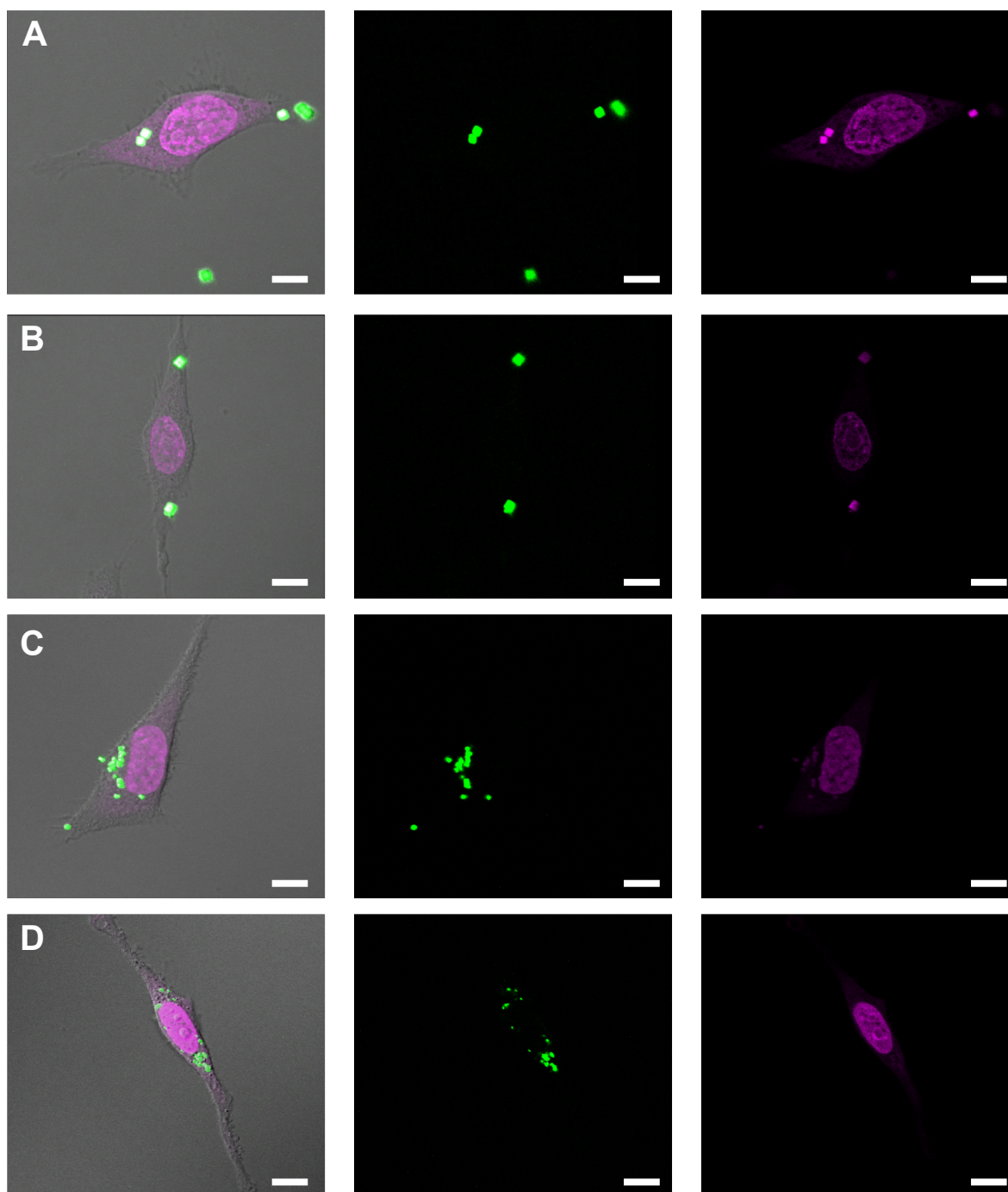


Figure 2.8 Confocal laser scanning microscopy images of HeLa cells after a 1 h incubation period at 37°C with A) 3 μm cubes, B) 2 μm cubes, C) 1 μm (AR = 1) cylinders, D) 200 nm (AR = 1) cylindrical particles {scale bar = 10 μm }.

Transmission electron microscopy (TEM) was used to gain additional understanding of the mechanism of PRINT particle internalization by HeLa cells (Figure 2.9). Cylindrical PRINT particles having a diameter of 200 nm ($AR = 1$) were readily internalized by HeLa cells through multiple modes of non-specific endocytosis (Figures 2.9B-D). TEM micrographs of the low aspect ratio cylindrical particles ($d = 200$ nm, $h = 200$ nm) clearly shows that the internalization of these particles occurs and that internalization is by a combination of mechanisms most notably energy-dependent phagocytosis and a clathrin-mediated mechanism. At early times both mechanisms are observed. A clathrin-coated pit is clearly associated with an internalized particle as seen in Figure 2.9B and Figure 2.9C. Internalization at the surface is associated with actin rearrangement near the plasma membrane and extension into the extracellular space (Figure 2.9B). Furthermore, high aspect ratio nanoparticles ($d = 150$ nm, $h = 450$ nm) were rapidly internalized into HeLa cells and translocated close to the nuclear membrane (Figures 2.9E-F). At 1 hour, these rod-like particles had traversed significantly further into the cells when compared to both the low aspect ratio cylindrical nanoparticles ($d = 200$ nm, $h = 200$ nm) and the $1\text{ }\mu\text{m}$ ($AR = 1$) cylindrical particles at similar times. This observation qualitatively supports the rate data obtained using flow cytometry. Figures 2.9G-I clearly show the internalization and translocation of cylindrical $1\text{ }\mu\text{m}$ ($AR = 1$) PRINT particles deep within the cell over the time frame examined.

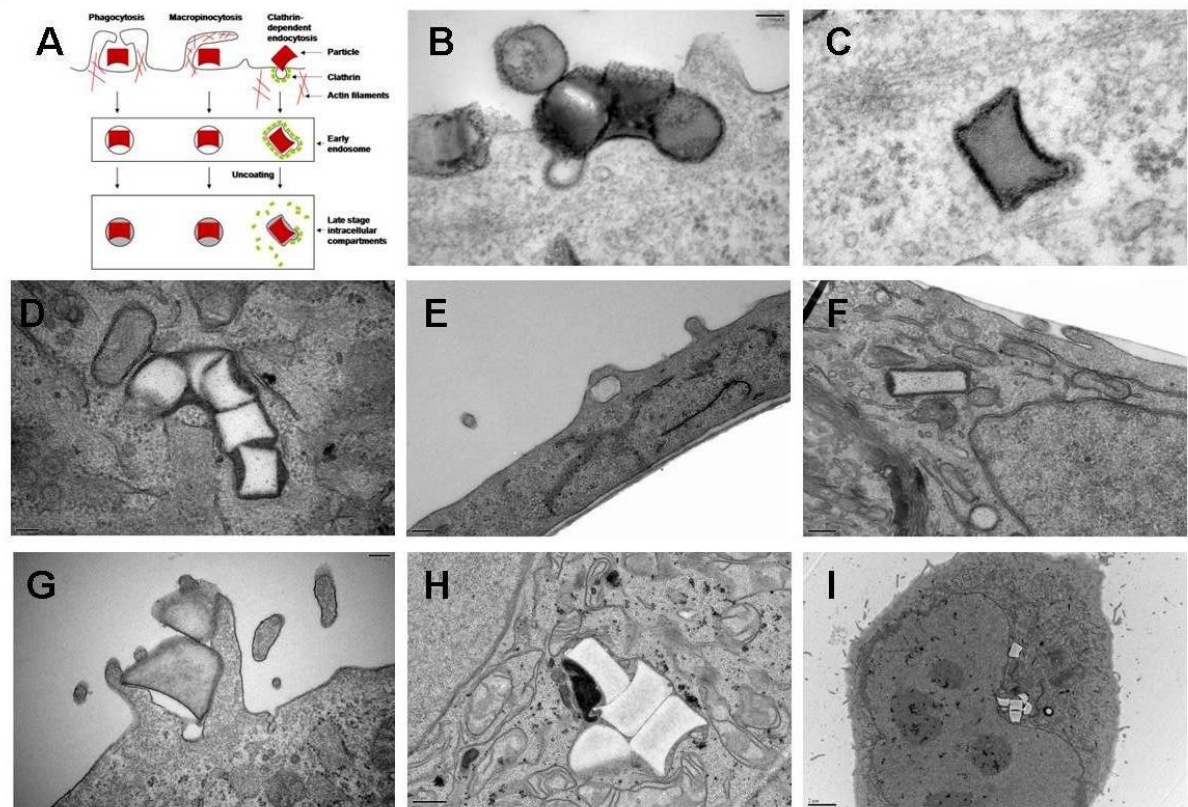


Figure 2.9 Transmission electron microscopy images of HeLa cells at 37°C (incubation times in parenthesis) with B-D) 200 nm x 200 nm cylindrical particles (AR = 1) (B,C – 15 minutes, D - 4 hours), E-F) 150 nm x 450 nm cylindrical particles (E-F – 1 hour), G-I) 1 µm cylindrical particles (G – 1 hour, H,I – 4 hours)

To more clearly delineate the role of specific endocytotic pathways involved in PRINT particle cellular internalization, HeLa cells were treated with known biochemical inhibitors of energy-dependent processes, clathrin-mediated processes, caveolae-mediated processes, and macropinocytotic endocytosis (Figure 2.10). To investigate energy-dependence, cells were pre-incubated in the presence of $\text{NaN}_3/2$ -deoxyglucose (NaN_3/DOG) and then treated with PRINT particles. NaN_3/DOG , which blocks cellular ATP synthesis, resulted in a marked decrease in the cellular internalization of all particle sizes (68-84 % compared to non-treated cells) indicating

that internalization is an energy dependent process, with the smaller PRINT particles showing a slightly higher tendency for energy dependence (78 % for 200 nm (AR = 1); 84 % for 150 nm (AR = 3) than the larger 1 μ m (AR = 1) (68 %)). Complete inhibition was not seen and is most likely due to the presence of exogenous ATP and glucose in the serum-free media. Similarly, internalization of the smaller PRINT particles was markedly decreased in the presence of cytochalasin D (63 % and 77 % for 200 nm and 150 nm, respectively), an inhibitor of actin polymerization as compared to the larger 1 μ m particles (24 %). While cytochalasin D is generally classified as an inhibitor of macropinocytosis/phagocytosis, both clathrin- and caveolae-mediated pathways have recently been shown to require actin for formation and invagination of both coated pits and caveosomes [24]. Due to the fact that HeLa cells are considered as non-phagocytosing cells, the inhibition of particle internalization by cytochalasin D may reflect inhibition of either clathrin-mediated or caveolae-mediated pathways, or a combination of the two. Indeed, comparison of the cytochalasin inhibition to the inhibition of clathrin-mediated endocytosis using the dynamin-GTPase inhibitor Dynasore and inhibition of caveolae-mediated endocytosis with the natural isoflavone tyrosine kinase inhibitor genistein shows an almost identical inhibition pattern [25]. The importance of actin involvement is also demonstrated in TEMs of all three sizes of particles (Figure 2.10). Surprisingly, chlorpromazine, a cationic amphipathic drug also used to probe clathrin-mediated endocytosis, showed significant inhibition when compared to internalization in the presence of Dynasore with the 200 nm (AR = 1) and 1 μ m (AR = 1) particle sizes being inhibited by 92 %

compared to ~ 60 % and 87 % compared to ~ 36 %, respectively. No change was observed between the two inhibitors for the 150 nm (AR = 3) particles. Due to the amphipathic nature of the drug, chlorpromazine is readily capable of incorporating into the lipid bilayer of the plasma membrane increasing lipid fluidity which in turn may inhibit or block the formation of membrane invaginations thus leading to a decrease in particle internalization. Nonetheless, both chlorpromazine and Dynasore demonstrated the importance of the clathrin-mediated pathway for the internalization of the 150 nm (AR = 3) and 200 nm (AR = 1) cylindrical PRINT particles, where ~ 70 % inhibition of internalization was seen for the 150 nm (AR = 3) particles, and ~ 60 % inhibition was seen for the 200 nm (AR = 1) particles. The exact role of this pathway in the internalization of 1 μ m (AR = 1) cylindrical PRINT particles is not clearly delineated since only ~ 35 % of internalization was inhibited in the presence of Dynasore but more than 85 % was observed with chlorpromazine. To discern any role that caveolae-mediated endocytosis may play in nanoparticle uptake two inhibitors, genistein, a tyrosine kinase inhibitor, and methyl- β -cyclodextrin, a cyclic heptasaccharide known to sequester and alter cholesterol-rich domains within the plasma membrane were used. For both inhibitors, caveolae-mediated endocytosis was observed to be a prominent internalization pathway for the 150 nm (AR = 3) and 200 nm (AR = 1) cylindrical PRINT particles (~ 60 % inhibition seen with both particles with both inhibitors) with very little inhibition detected with the larger 1 μ m (AR = 1) PRINT particles (~ 10-25 %). These data are consistent with the current view that caveolae generally can only endocytose nanoparticles in the range of 50-100 nm [26]. All of these experiments strongly

suggest that clathrin-mediated, and caveolae-mediated endocytosis and to a much lesser extent macropinocytosis are involved with both the nano- and microparticles internalization, but these mechanisms play a larger role with the internalization of the smaller (150 nm (AR = 3) and the 200 nm (AR = 1)) PRINT nanoparticles. It should be noted that none of the specific chemical inhibitors led to greater than 95 % inhibition of internalization. This observation is most likely indicative of the role of non-clathrin, non-caveolae mediated pathways for internalization. Interestingly, the rapidly internalizing 150 nm (AR = 3) particles utilize all internalization pathways to a large extent, possibly pointing to the reason why these particles are internalized to such a high degree relative to the other shapes.

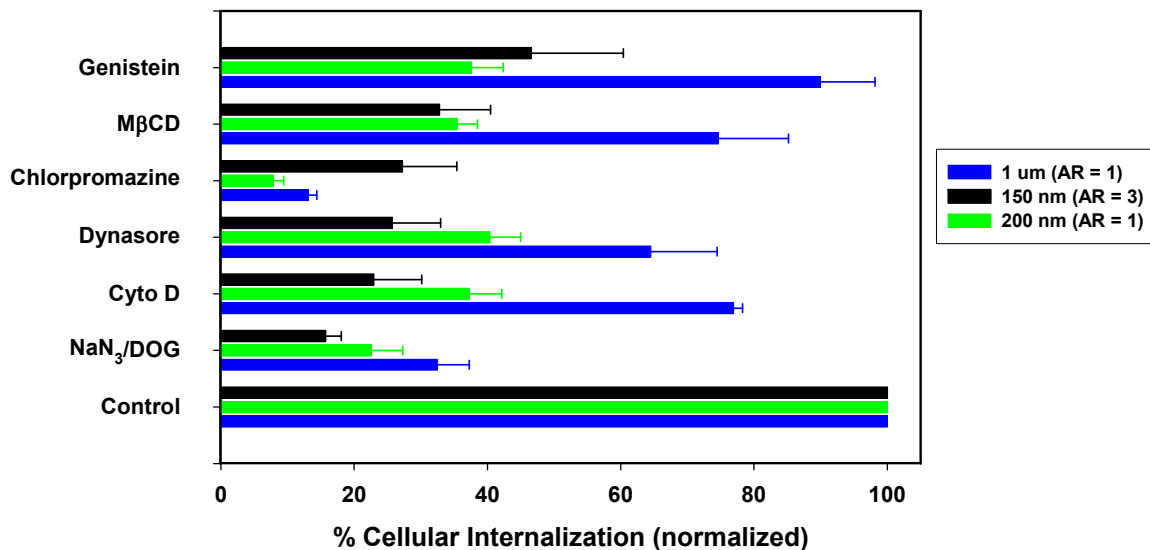


Figure 2.10 Probing the mechanisms of cellular internalization using inhibitors of endocytosis. HeLa cells were incubated with the indicated inhibitors in the graph as outlined in the experimental methods. Percent internalization was normalized to particle internalization in the absence of inhibitors.

2.4 Conclusions

The biochemical inhibitory studies, the confocal microscopy data, the TEM data, and the flow cytometry analysis of the precisely defined and shaped PRINT particles reveal a number of interesting results and a couple of surprises. First, current scientific thought is that the upper limit of the size of any nanoparticle internalized into non-phagocytotic cells by means of non-specific endocytosis is 150 nm; thus any particle larger than 150 nm would be excluded from cellular internalization altogether [27-29]. The results suggest that this upper size limit convention needs to be raised significantly as we clearly see the internalization of 3 μm , 2 μm and 1 μm sized particles. To the best of our knowledge this is the first report of the intracellular uptake and transport of biologically-relevant nanoparticles greater than 200 nm into non-phagocytic mammalian cells. Second, our data reveals that internalized PRINT particles of any size appear to follow multiple pathways into the cell. Third, there was a significant diminution of particle internalization in cells when the particles had a negative zeta potential versus particles that had a positive zeta potential. The dramatic switch in the internalization of particles with the sign of the zeta potential points to a potential strategy for enhancing the specificity of particle targeting to cells of interest. It will be interesting to conjugate ligands capable of stimulating specific receptor mediated endocytosis to particles having a negative zeta potential as a strategy to enhance the specificity of cell targeting objectives. Fourth, it was surprising to find that the internalization of the rod-like, high aspect ratio nanoparticles ($d = 150 \text{ nm}$, $h = 450 \text{ nm}$) occurs much more rapidly and efficiently than would be expected based on size considerations alone, suggesting a

special role associated with the shape of the particles. Specifically, these high aspect ratio, rod-like PRINT particles were internalized faster than their more symmetric 200 nm (AR = 1) cylindrical particle counterpart, even though both particles are substantially equal in volume. Furthermore, rod-like nanoparticles having the same aspect ratio and smaller dimensions (cylindrical particles with $d = 100$ nm and $h = 300$ nm vs cylindrical particles with $d = 150$ nm and $h = 450$ nm) did not increase the amount of particles internalized into HeLa cells. Thus the interplay between particle shape and size at constant surface chemistry will undoubtedly play a role in numerous areas of interest including particle targeting strategies in therapeutic applications, environmental fate of nanoparticles, and may even shed some light on the rationale behind bacterial pathogen sizes and shapes.

3.5 References

- (1) Cossart, P., *J. Clin. Invest.* **1997**, 99, (10), 2307-2311.
- (2) Lukyanov, A. N.; Elbayoumi, T. A.; Chakilam, A. R.; Torchilin, V. P., *J. Controlled Release* **2004**, 100, (1), 135-144.
- (3) Torchilin, V. P., *Cellular and Molecular Life Sciences* **2004**, 61, (19-20), 2549-2559.
- (4) Kabanov, A. V.; Felgner, P. L.; Seymour, L. W., *Self-assembling Complexes for Gene Delivery. From Laboratory to Clinical Trial* Eds.; Wiley: Chichester, 1998.
- (5) Sarciaux, J. M.; Acar, L.; Sado, P. A., *Int. J. Pharm.* **1995**, 120, (2), 127-136.
- (6) Duncan, R.; Izzo, L., *Adv. Drug Delivery Rev.* **2005**, 57, 2215-2237.
- (7) Barth, R. F.; Adams, D. M.; Soloway, A. H.; Alam, F.; Darby, M. V., *Bioconjugate Chem.* **1994**, 5, (1), 58-66.
- (8) Bianco, A.; Kostarelos, K.; Prato, M., *Curr. Opin. Chem. Biol.* **2005**, 9, (6), 674-679.
- (9) Metraux, G. S.; Mirkin, C. A., *Adv. Mater.* **2005**, 17, (4), 412-+.
- (10) Geng, Y.; Dalhaimer, P.; Cai, S. S.; Tsai, R.; Tewari, M.; Minko, T.; Discher, D. E., *Nature Nanotechnology* **2007**, 2, (4), 249-255.
- (11) Rejman, J.; Oberle, V.; Zuhorn, I. S.; Hoekstra, D., *Biochem. J.* **2004**, 377, 159-169.
- (12) Zauner, W.; Farrow, N. A.; Haines, A. M. R., *J. Controlled Release* **2001**, 71, (1), 39-51.
- (13) Champion, J. A.; Mitragotri, S., *Proc. Natl. Acad. Sci. U.S.A.* **2006**, 103, (13), 4930-4934.
- (14) Xia, Y.; Whitesides, G. M., *Angew. Chem.* **1998**, 110, (5), 568-594.
- (15) Euliss, L. E.; DuPont, J. A.; Gratton, S.; DeSimone, J., *Chem. Soc. Rev.* **2006**, 35, (11), 1095-1104.
- (16) Rolland, J. P.; Maynor, B. W.; Euliss, L. E.; Exner, A. E.; Denison, G. M.; DeSimone, J. M., *J. Am. Chem. Soc.* **2005**, 127, (28), 10096-10100.

- (17) Fattorossi, A.; Nisini, R.; Pizzolo, J. G.; Damelio, R., *Cytometry* **1989**, 10, (3), 320-325.
- (18) Smith, P. J.; Blunt, N.; Wiltshire, M.; Hoy, T.; Teesdale-Spittle, P.; Craven, M. R.; Watson, J. V.; Amos, W. B.; Errington, R. J.; Patterson, L. H., *Cytometry* **2000**, 40, (4), 280-291.
- (19) Garnett, M. C., *Crit. Rev. Ther. Drug Carrier Syst.* **1999**, 16, (2), 147-207.
- (20) Zauner, W.; Ogris, M.; Wagner, E., *Adv. Drug Delivery Rev.* **1998**, 30, (1-3), 97-113.
- (21) Gratton, S. E. A.; Pohlhaus, P. D.; Lee, J.; Guo, I.; Cho, M. J.; DeSimone, J. M., *J. Controlled Release* **2007**, 121, (1-2), 10-18.
- (22) Miller, C. R.; Bondurant, B.; McLean, S. D.; McGovern, K. A.; O'Brien, D. F., *Biochemistry* **1998**, 37, 12875-12883.
- (23) Matteoni, R.; Kreis, T. E., *J. Cell Biol.* **1987**, 105, 1253-1265.
- (24) Kaksonen, M.; Toret, C. P.; Drubin, D. G., *Nature Reviews Molecular Cell Biology* **2006**, 7, (6), 404-414.
- (25) Macia, E.; Ehrlich, M.; Massol, R.; Boucrot, E.; Brunner, C.; Kirchhausen, T., *Developmental Cell* **2006**, 10, (6), 839-850.
- (26) Simionescu, N.; Simionescu, M.; Palade, G. E., *Journal of Cell Biology* **1975**, 64, (3), 586-607.
- (27) Conner, S. D.; Schmid, S. L., *Nature* **2003**, 422, (6927), 37-44.
- (28) Gary, D. J.; Puri, N.; Won, Y. Y., *J. Controlled Release* **2007**, 121, (1-2), 64-73.
- (29) Oupicky, D.; Konak, C.; Ulbrich, K.; Wolfert, M. A.; Seymour, L. W., *J. Controlled Release* **2000**, 65, (1-2), 149-171.

CHAPTER 3

NANOFABRICATED PARTICLES FOR ENGINEERED DRUG THERAPIES: A PRELIMINARY BIODISTRIBUTION STUDY OF PRINT NANOPARTICLES

3.1 Introduction

Despite continued progress in the identification, characterization, and synthesis of advanced therapeutics, the full potential of such innovations can only be achieved with the concomitant realization of *in vivo* profiles ideal for pharmacological intervention. In the realm of drug discovery, the hindrance to obtaining such a profile may be as simple as poor solubility in biological media. For instance, it has been reported that ten percent of marketed drugs suffer from solubility problems, over a third of pipeline drugs are poorly soluble, and almost two-thirds of drugs coming from early pre-clinical development have low solubility [1]. As such, almost forty percent of all possible drug targets fail early due to poor solubility characteristics. More complex problems with drug candidates may include unfavorable pharmacokinetics, and high systemic toxicity. Particular attention must also be given when considering the delivery of biochemically labile substances such as siRNA and other oligonucleotides for gene therapy, as these sensitive cargos need to be protected during circulation. In addition, they need to be delivered to the appropriate tissue or organ, and released intracellularly into the cytosol or nucleus to be effectively used as therapeutics. Finally, the efficient delivery of detection and imaging agents is an extremely important step in the early diagnosis and treatment of disease.

The development and utilization of nanocarriers in response to many of the aforementioned problems encountered *in vivo* has led to dramatic improvements in the biological profile of important therapies. Intense research in drug delivery over the past few decades has seen the design and construction of valuable nanocarriers such as liposomes, micelles, dendrimers, polymer particles, and colloidal

precipitates [2-9]. However, only a handful of drugs and imaging agents delivered using these classical approaches have made it into the clinic [1,2]. One underlying reason for the delayed development is that none of these approaches offers the ability to comprehensively, simultaneously, and independently address several different design criteria. The ability to meet such demanding parameters is quintessential to the design of effective delivery vectors and has been the focus of intense research in our laboratory. In this report, the first *in vivo* study of PRINT particles administered intravenously into healthy mice is described. The promising biodistribution profile and blood pharmacokinetics of 200 nm non-targeted radiolabeled PEG-based nanogels fabricated using PRINT methodology are discussed.

3.2 Experimental

3.2.1 Materials

FluorocurTM, the perfluoropolyether used as the molding material in the PRINT process, was purchased from Liquidia Technologies (Product # 2M-140). Trimethylolpropane ethoxylate triacrylate ($M_n = 428$ g/mol) (Aldrich), was passed through a short plug of alumina prior to use to remove inhibitor. Poly(ethylene glycol) monomethyl ether monomethacrylate ($M_n = 1,000$ g/mol) (Polysciences), *para*-hydroxystyrene (Alfa Aesar, 10% (w/w) in propylene glycol) and 2,2-diethoxyacetophenone (Aldrich) were used as received without further purification. Iodogen® pre-coated tubes were purchased from Pierce Biotechnology, Inc., and

radioactive iodine (Na^{125}I) was purchased from Perkin Elmer Life and Analytical Sciences, Inc. as 100 mCi/mL in 10^{-5} M NaOH. HeLa cells and all cell culture media (MEM, OptiMEM) were purchased from the tissue culture facility at The University of North Carolina at Chapel Hill. CellTiter 96* AQueous One Solution Cell Proliferation Assay (MTS) was purchased from Promega Corporation. The lysis agent used for negative controls in *in vitro* viability studies with HeLa cells was 9% w/v solution of Triton® X-100 in water. Silicon templates used as masters were obtained from Benchmark Technologies. C57BL/6J mice were purchased from The Jackson Laboratory. Ketamine HCl (100 mg/mL) was purchased from Abbott Laboratories. Cholesterol and 1,2-Distearoyl-*sn*-Glycero-3-Phosphocholine (DSPC) were purchased from Avanti Polar Lipids, Incorporated. All animal experiments were conducted in accordance with guidelines set forth by The University of North Carolina at Chapel Hill, and approval was obtained for the completion of these experiments.

3.2.2 Preparation of PRINT nanoparticles

The fabrication of patterned Fluorocur™ molds has been described elsewhere [3]. Briefly, 20 mL of Fluorocur™ resin containing 0.1% (w/w) of 2,2-diethoxyacetophenone was pooled in the center of an 8 inch patterned master (with feature sizes of 200 nm) which was set up inside an enclosed UV chamber. Ten minutes was allowed to pass so that the Fluorocur™ resin was spread out over the entire 8 inch wafer. The entire system was then purged with nitrogen for 3 minutes. Following this, the coated wafer was exposed to UV irradiation ($\lambda = 365$ nm, power >

20 mW/cm²) for 2 minutes to cure the Fluorocur™ resin. The elastomeric mold was then removed from the master template by gently peeling it away from the silicon surface.

In these experiments, the PRINT particles were derived from a mixture composed of 78% (w/w) PEG₄₂₈ triacrylate, 20% (w/w) PEG₁₀₀₀ monomethyl ether monomethacrylate, 1% (w/w) 2,2-diethoxyacetophenone, and 1% (w/w) *para*-hydroxystyrene. A 10% (w/v) solution of this mixture in 2-propanol (filtered through a 0.22 µm PTFE filter) was prepared. This solution (1 mL) was then sprayed onto a Fluorocur™ patterned mold using an air brush and residual 2-propanol was allowed to evaporate over 10 minutes. A poly(ethylene) sheet (American Plastics Co.) was then placed over the 8 inch (diameter) mold ensuring that the entire active area was covered. This poly(ethylene) sheet was then peeled back at a rate of approximately 2.5 cm/min. Following this, the mold was placed in a UV curing chamber. The chamber was purged with nitrogen for 3 minutes and UV irradiation was applied (λ = 365 nm, power > 20 mW/cm²) for 2 minutes.

Monomer	Function	Wt %
PEG ₄₂₈ triacrylate	Cross-linking agent	78
PEG ₁₀₀₀ monomethylether monomethacrylate	Biocompatibility, Stability	20
<i>para</i> -hydroxystyrene	Chemical handle	1
2,2-diethoxyacetophenone	Initiator	1

Table 3.1 Particle composition

To facilitate removal of the particles from the mold, a physical means for harvesting the particles was utilized. Specifically, a 2 mL aliquot of acetone (filtered

through a 0.22 μm PTFE filter) was placed on the particle-filled mold and this drop of acetone was gently moved along the surface of the mold using a glass slide. The movement of the glass slide facilitated release of the particles from the mold. The suspended particles were collected in a 50 mL Falcon tube and diluted to the 50 mL mark with filtered acetone after particle collection was complete. The suspension was vortexed for 10 minutes and was centrifuged at 3200 rpm for 30 minutes using a IEC CENTRA CL2 Centrifuge (Thermo Electron Corporation). The supernatant was removed via aspiration and the particle pellet was redispersed in 50 mL of fresh acetone by vortexing for 10 minutes followed by centrifugation for an additional 30 minutes. This process was repeated once more and after aspiration the particles were redispersed in 5 mL of distilled water by sonicating the dispersion for 15 minutes. The particle dispersion was filtered through a 20 μm filter into a fresh 50 mL Falcon tube, and diluted to the 50 mL mark with acetone. This particle suspension was then centrifuged for one hour. The supernatant was removed via aspiration and the particle pellet was redispersed in 50 mL of fresh acetone by vortexing for 10 minutes followed by centrifugation for an additional 30 minutes. This washing process was repeated once more (with acetone) and after aspiration the particles were redispersed in a minimal amount of acetone, transferred to a tarred Eppendorf tube, and centrifuged in a microfuge (Fisher Scientific) for 20 minutes. The supernatant was removed and the pellet was dried in a vacuum oven overnight, massed, and dispersed in the appropriate amount of sterile water to make a 10 mg/mL dispersion of particles.

3.2.3 Preparation of liposomes

Lipids (DSPC:Cholesterol, 55:45 mol) were dissolved in chloroform and evaporated to dryness in a rotary evaporator under reduced pressure at 50 °C. After leaving the lipid film overnight under reduced pressure, the film was hydrated with PBS at pH 7.0. Unilamellar liposomes were formed by extrusion with 20 passes through a double-stacked polycarbonate membrane (Whatman Nucleopore) with a pore size of 200 nm, resulting in a liposome diameter of 177 nm with a polydispersity of 0.026 as determined by dynamic light scattering [4,5].

3.2.4 Particle size analysis of PRINT nanoparticles using scanning electron microscopy (in the dry state)

The size of PRINT nanoparticles was analyzed via scanning electron microscopy (Hitachi model S-4700). Particle dispersions were prepared at concentrations of 0.5 mg/mL, and a drop of this solution was placed on a glass slide. The drop was then allowed to dry, and the glass slide was coated with 1.5 nm of Pd/Au alloy using a Cressington 108 auto sputter coater (Cressington Scientific Instruments Ltd.). The Pd/Au coated glass slide was then adhered to the sample holder using double-sided adhesive tape, and placed inside the vacuum chamber of the SEM and observed under low vacuum (10^{-6} Torr).

3.2.5 Particle size analysis of PRINT nanoparticles, and liposomes, using dynamic light scattering (in suspension)

The size and polydispersity of PRINT nanoparticles was analyzed via dynamic light scattering (DLS) using a 90Plus Particle Size Analyzer (Brookhaven Instruments Corporation). The particles were dispersed in PBS at a concentration of 0.5 mg/mL and measured without filtration at 25 °C and 37 °C. The DSPC:CHOL liposomes were diluted with PBS to a concentration of 0.5 mg/mL, and were measured under the same conditions as PRINT particles.

3.2.6 Zeta potential measurements

The zeta potential of PRINT nanoparticles was measured using a ZetaPlus Zeta Potential Analyzer (Brookhaven Instruments Corporation). The nanoparticles were dispersed in water at a concentration of 0.3 mg/mL and the zeta potential was measured.

3.2.7 Radiolabeling of PRINT nanoparticles with ^{125}I

PRINT nanoparticles were radiolabeled using IodogenTM solid phase oxidant in the presense of Na¹²⁵I. Briefly, 10 mg of PRINT particles in 1 mL of H₂O, 53 μL of phosphate buffered saline, and 1 mCi of Na¹²⁵I in 10 μL of 10⁻⁵ M NaOH were added to an IodogenTM pre-coated tube (50 μg of IodogenTM reagent) and the tube was swirled every other minute for 15 minutes. The radiolabeled particle solution was then transferred to a pre-weighed 1.5 mL Eppendorf tube. The original reaction tube was rinsed with one 20 μL portion of 1 mM KI and with two 100 μL portions of water

and the rinsing solutions were added to the tube containing radiolabeled particles followed by the addition of NaHSO₃ (1 μmol/10 μL). The particle dispersion was then centrifuged for 10 minutes at 15,000 x g using an Eppendorf centrifuge 5415 D (Eppendorf). The supernatant was removed and the particles were washed with four 500 μL portions of water (until the radiation in the supernatant was no greater than the background, ensuring complete removal of non-specifically bound ¹²⁵I) and evaporated to dryness in a SpeedVac SC100 (Savant Instruments). The total mass recovered was 9.45 mg. The specific activity was measured with a Beckman Gamma 5500B gamma counter (Laboratory Technologies) and found to be 5.5 μCi/mg PRINT particles.

3.2.8 In vitro cytotoxicity

HeLa cells were seeded in 100 μL of media [Minimum Essential Medium (MEM) containing Earle's salts and supplemented with 1 mM sodium pyruvate and non-essential amino acids] at a density of 5×10^3 cells per cm² into a 96-well microtitre plate. Cells were allowed to adhere for 24 h before MEM was replaced with Opti-MEM (90 μL per well) and the particle preparation (10 μL per well in PBS). Positive controls contained PBS alone. HeLa cells were incubated with the PRINT particles for 4 h at 37 °C in a humidified 5% CO₂ atmosphere. After the 4 h incubation period, negative controls were prepared by the addition of 2 μL of lysis solution to a few wells containing cells only. After 2 minutes, the MTS assay solution was added (20 μL per well) into each well. The cells were then incubated for an additional 1 h at 37 °C in a humidified 5% CO₂ atmosphere. The optical density at

450 nm was measured using a BioRad Model 3550 microplate reader (BioRad Laboratories). The viability of the cells exposed to neutral PRINT particles was expressed as a percentage of the viability of cells grown in the absence of particles.

3.2.9 Biodistribution of [¹²⁵I]-labeled PRINT particles

C57Bl/6J mice were housed under specific pathogen-free conditions for one week and were used at 8 weeks of age (~18 g). Animals were injected intravenously via bolus tail vein administration with 0.32 mg of [¹²⁵I]-labeled PRINT particles with a specific activity of 4.3 μ Ci/mg in 100 μ L of PBS (phosphate buffered saline, Sigma-Aldrich). At 10 min, 30 min, 1, 3, and 8 h after dosing, groups of four mice were anesthetized by intraperitoneal injection of 100 μ L of ketamine HCl solution in PBS (50 mg/mL). Blood was collected via cardiac puncture. Samples of blood and organs harvested (liver, kidneys, spleen, lungs, and heart) were weighed and counted to determine the total radioactivity in a Beckman Gamma 5500B gamma counter (Laboratory Technologies). An additional four animals were kept in a metabolic cage after injection of the [¹²⁵I]-labeled PRINT nanoparticles. At 24 h post-injection, the accumulated urine and feces were collected for radioactivity measurements. After these animals were sacrificed (as described above) the blood as well as the organs were removed, weighed, and assayed for radioactivity.

3.3 Results and discussion

The particle composition was engineered to produce biologically relevant delivery vectors. Several monomers were added to introduce specific functionality

into the hydrogel nanoparticles: poly(ethylene glycol) triacrylate, poly(ethylene glycol) monomethyl ether monomethacrylate, and *p*-hydroxystyrene (PHS) (Figure 3.1). Poly(ethylene glycol) derivatives have long been known to impart biocompatibility, solubility, stability, and increased circulation times to proteins, liposomes, and particles [6-10]. The phenol-containing monomer, PHS, was selected as a chemical handle so that gentle radioiodination of the particles was possible. Since mPEG₁₀₀₀ monomethacrylate is a solid, 2-propanol was used to obtain a homogeneous solution of the monomer precursors, so that a thin film of monomer mixture could be sprayed onto the PFPE mold. To this point, any solvent (or combinations of solvents) can be used in the PRINTing process, as long as the contact angle of the resultant solution onto the PFPE mold is less than 90°. Alternatives to this method include a melt PRINT process, where the monomers are heated to above their melting point, and the PRINT process is carried out, allowing a solvent-free process.

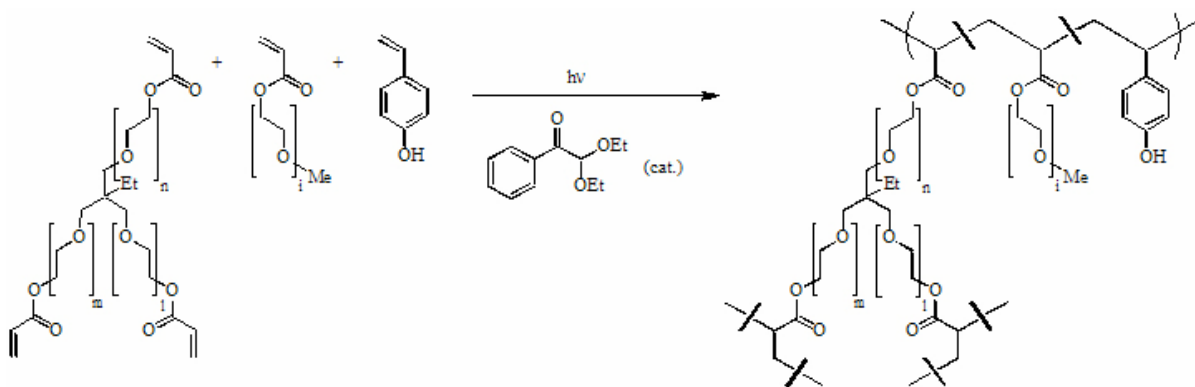


Figure 3.1 Chemical structures of monomers and a partial structure of the PRINT nanogel. *p*-Hydroxystyrene was introduced for radioiodination at 1% (w/w). Throughout the present study, it is assumed that iodinated PRINT nanogels behave the same as unmodified particles.

The uniformity of size and shape of the hydrogels was confirmed using scanning electron microscopy (SEM, Figure 3.2). The micrographs show the isolation of thousands of virtually identical cylindrical particles, thus verifying PRINT's ability to copy the nanoscale features of a patterned wafer with high precision. The diameter of the particles in the dry state was determined from the scanning electron micrographs to be 201 ± 10 nm and the height was determined to be 155 ± 10 nm. A dry sample is required for SEM and thus the micrographs obtained do not represent the dispersion the particles have once in solution.

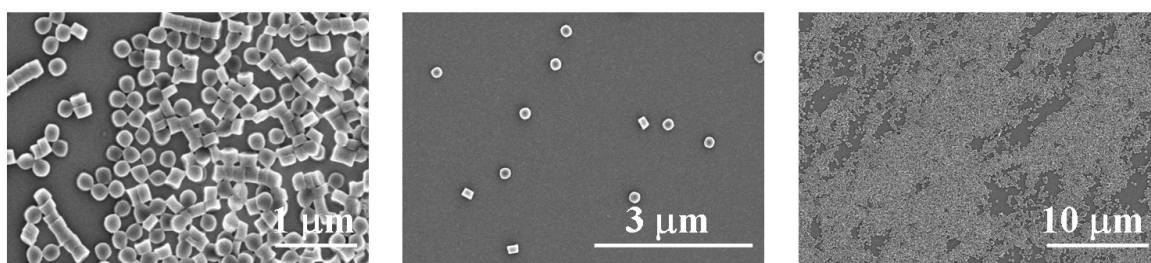


Figure 3.2 Scanning electron micrographs of 200 nm PRINT particles used in the present study

Method	Parameter
SEM	Height: 155 ± 10 nm Width: 201 ± 10 nm
DLS	Diameter: 234 ± 12 nm
Zeta Potential	-30.4 ± 1.5 mV

Table 3.2 Particle characterization

The nanocarriers used most frequently today for the delivery of therapeutics in the clinic can best be classified under the general heading of self-assembled structures. Nanovectors fitting this description include micelles, liposomes, and protein aggregates. As a result of their inherent dynamic nature, these nanoparticles derived from the self-assembly of small molecules would be expected to undergo structural changes once *in vivo*. As such, it is difficult to make a direct connection between the particle formulation prior to administration and the therapeutic outcome. As an example of this behavior, the size and polydispersity of liposomes and PRINT particles in water were investigated via dynamic light scattering at room temperature (25 °C) and then at physiological temperature (37 °C) over the course of several hours (Figure 3.3). At 25 °C both liposomes and PRINT particles have a low polydispersity immediately upon formation or dispersion. Upon heating to 37 °C, the mean diameter and polydispersity of liposomes changes dramatically as a function of time. Over the time course of 6 h at physiological temperature, the PRINT particles remain stable as observed by a steady size and polydispersity (234 ± 12 nm, PDI = 0.005). This could be an important attribute in the design of nanocarriers, since it is expected that the size and polydispersity of dynamic structures may change even more rapidly once in the serum. The zeta potential of these PRINT nanoparticles was measured to be -30.4 ± 1.5 mV.

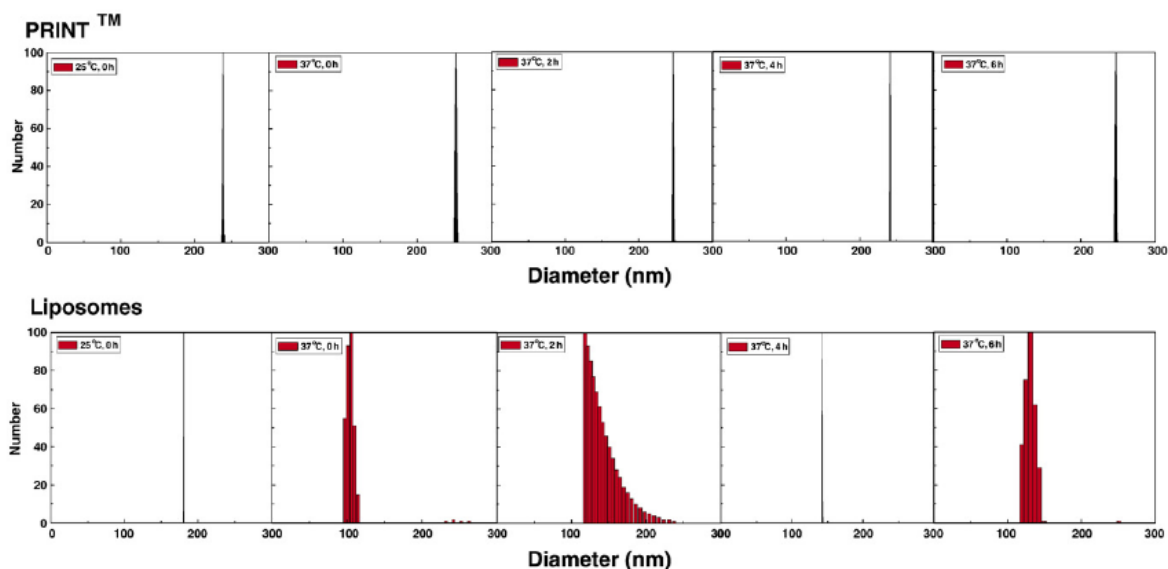


Figure 3.3 A time-dependent study of the mean diameter, polydispersity and stability of PRINT particles (top), and liposomes (bottom) using dynamic light scattering

The cytotoxicity of the PRINT nanoparticles was assessed in a cursory manner using a MTS cell viability assay [11]. This particular assay is a colorimetric evaluation that determines the number of living cells by quantifying the amount of formazan product present, which is directly proportional to the number of viable cells. Figure 3.4 shows high viability relative to the negative control, supporting the non-toxic nature of the nanoparticles, even at high concentrations (100 $\mu\text{g/mL}$ is equivalent to 800,000 particles/cell). Based on the toxicity data obtained, the PRINT nanoparticles appear biocompatible and suitable for future *in vivo* studies.

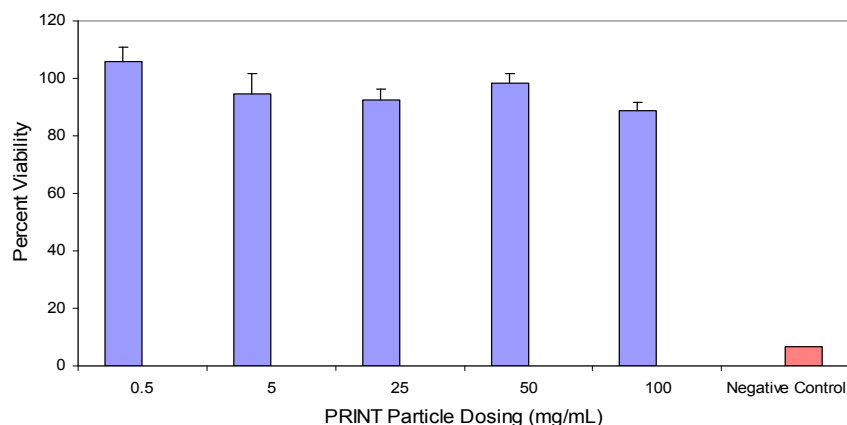


Figure 3.4 MTS assay depicting the non-toxic nature of 200 nm PRINT particles incubated with HeLa cells. Approximately 10^3 cells were plated per 1 cm^2 . Cells were exposed to varying concentrations of PRINT particles in 0.1 mL media for 4 h at 37 °C before the MTS assay was performed. Control wells, where the cells were exposed to only PBS serve as 100% in normalization. Vertical bars stand for one SD with $n = 5$

In this study, 200 nm [^{125}I]-labelled PRINT particles were administered into healthy C57BL/6J mice via tail vein bolus injection at a dose of 20 mg/kg. The particles were radiolabeled using Iodogen® following the procedure recommended by the supplier (Pierce). The tissue distribution was monitored using a gamma counter, and the percent recovery of injected dose was calculated from the measured radioactivity. Figure 3.5 shows the tissue distribution of 200 nm PRINT nanoparticles at 10 min, 30 min, 1 h, 3 h, 8 h, and 24 h post-injection. Throughout the time-course of the study, the 200 nm PRINT particles were distributed mainly in the liver and spleen. The total recovery from these two organs amount to as much as 30% over the 24 h study period. This observation is consistent with the fact that the sinusoidal walls of these organs are lined with discontinuous endothelium that allows for passive entrapment of foreign particulates [12,13]. Although the present

study does not provide any direct evidence for or against it, it is likely that these particles are eventually taken up by the resident macrophages possibly subsequent to opsonization with serum proteins [14].

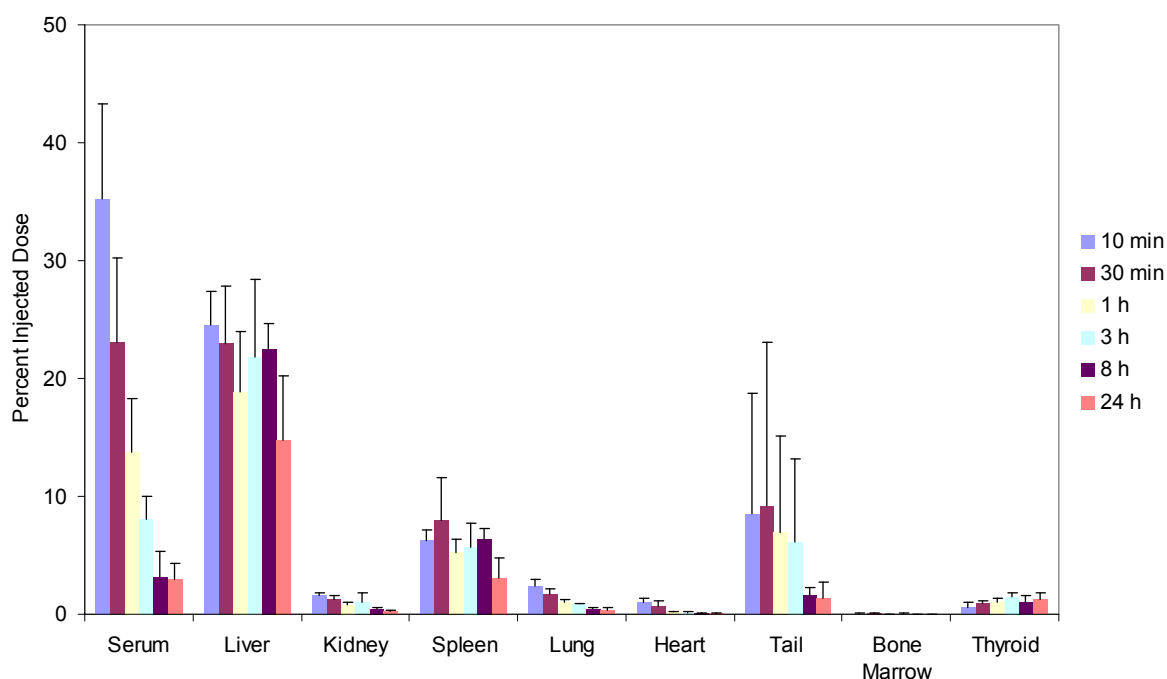


Figure 3.5 Biodistribution of 200 nm [^{125}I]-labeled PRINT particles in healthy mice subsequent to bolus tail vein injection at a dose of 20 mg/kg. The organ accumulation is expressed as a percent of injected dose after animals were sacrificed at 10 min, 30 min, 1, 3, 8, and 24 h post-intravenous injection. The organ data is presented as the mean \pm SD with $n = 4$. The recovery found in the blood assumes a blood volume of 2.18 mL/25 g mouse [15].

The particle accumulation was not significant in other organs harvested, often $\sim 1\%$ of the injected dose was found in the kidneys, heart, and lungs. The extent of particle accumulation reported in these organs may slightly over-represent the actual accumulation since the organs were not thoroughly rinsed to remove residual blood. Tails were collected in an effort to monitor the amount of nanoparticles that were

retained at the injection site. A significant amount of injected particles were found in the tail, especially during the initial 3 h period. This may be due to the rupture of blood vessels upon rapid injection of a large number of fine particles in a short period of time (< 5 seconds), creating endothelial gaps for particle retention. Finally, a trace but significant amount of radioactivity was observed in thyroid gland, possibly indicating the biodegradation of particles, yielding radioactive I_2 . Production of iodine from biochemical degradation of iodinated proteins or peptides is not uncommon and is also consistent with the observation that total recovery decreased steadily over the 24 h period studied (*vide infra*) [16].

Total recovery of the radioiodinated particles was found to decrease with time, beginning with an 81 ± 6 % recovery at 10 minutes post-injection and ending with a 24 ± 7 % recovery after 24 h (data not shown). Here, the total recovery was calculated from radioactivity measured only from the blood, liver, kidneys, spleen, lungs, heart, tail, bone marrow, and thyroid. In an effort to achieve a full mass balance, four mice were kept in metabolic cages for 24 h so that urine and feces could be collected and analyzed. For these mice, additional tissues and body parts such as fat, muscle, head, legs, intestines, and the remainder of the body were also analyzed for additional radioactivity. It was found that with these additional measurements, the total recovery at 24 h post-injection improved from 24 ± 7 %, with the main organs only, to 58 ± 4 %. The appearance of radioactivity in the thyroid gland throughout the study period (approximately 1% of injected dose) and in urine 24 h after dosing (as much as 8.6%) may suggest particle degradation [17]. This is also consistent with a hypothesis that loss of volatile radioactive iodine via the lungs

could have contributed to the time-dependent decrease in total recovery of radioactivity observed.

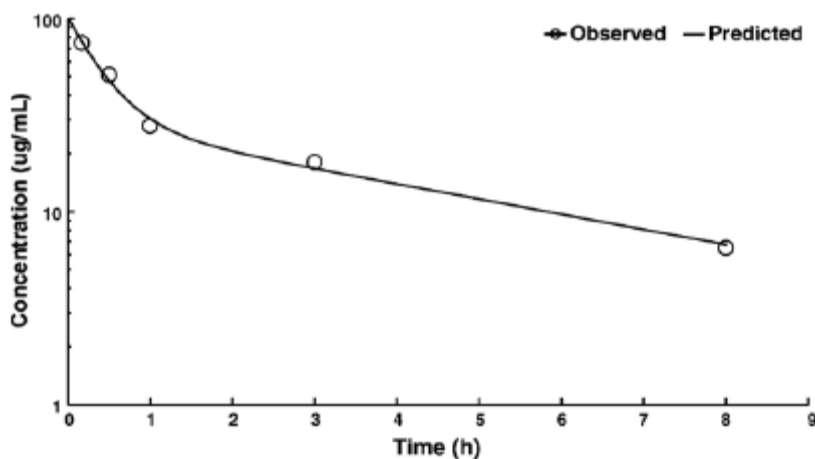


Figure 3.6 Blood pharmacokinetic profile of PRINT particles in healthy C57BL/6J mice. At given time intervals, four animals were sacrificed and blood was collected via cardiac puncture. Radioactivity observed was converted to particle concentration using the specific radioactivity measured and assuming a total blood volume of 2.18 mL/25 g mouse [15]. The data was subject to two-compartmental analysis (WinNonlin) resulting in pharmacokinetic parameters discussed in the text. For simplicity, data obtained 24 h post-injection are not shown in the figure or used for PK parameter determination.

As shown in Figure 3.6, the disappearance of PRINT particles from circulation was bi-exponential. The data set was fitted to a two-compartmental pharmacokinetic model with reversible distribution between central and peripheral compartments and with elimination from the central compartment. The pharmacokinetic parameters obtained using WinNonLin 5.0.1 (Pharsight Corporation) show the initial phase of rapid distribution with an apparent $t_{1/2}$ of 17 min. The rapid distribution is not surprising considering that the steric coat on the PRINT particles is only a low molecular weight PEG chain (9 mol %, 20% w/w of 1-kDa PEG monomethyl ether). It has been suggested that the optimal coating for the creation of long-circulating

liposomes is 3-7 mol % of 2-5 kDa PEG [18]. The shorter PEG chains used in the current particle formulation may not offer a radius of protection that is sufficient to effectively block the adsorption of opsonic proteins. The subtle nuances that both the degree of PEG incorporation and the molecular weight of PEG play in prolonging the circulatory $t_{1/2}$ are well documented for other types of nanocarriers [18-20].

Volumes of distribution of central and peripheral compartments were found to be 3 and 5 mL, respectively. Considering the blood volume of approximately 1.7 mL/20 g mouse, liver of 0.8 g, and spleen < 0.1 g, these values appear to be somewhat exaggerated, however, they certainly rule out any significant extravasation. Since the stability of the radiolabel is not well established in the present study and since it is the radioactivity that is monitored, it is difficult to unambiguously interpret the slow phase of radioactivity decay in the later time-points with an apparent $t_{1/2}$ of 3.3 h. The appearance of radioactivity in urine strongly suggests that these PRINT particles and/or their degradation products must be cleared rapidly from the blood. Thus, the slow elimination phase may well represent slow re-distribution of particles or particle remnants between the blood and organs/tissues.

The AUC, a measure of total availability of particles in the circulation for organ distribution extrapolated to infinite time, was determined to be 191 $\mu\text{g}\cdot\text{h/mL}$. Unmodified, conventional liposomes show dose-dependent pharmacokinetic parameters, including AUC upon i.v. administration. A liposome dose equivalent to the dose in the present study, 20 mg/kg, shows AUC values of approximately 70 to

700 $\mu\text{g}\cdot\text{h}/\text{mL}$. Thus, the present data are certainly in agreement with that reported for liposomes [21].

3.4 Conclusions

This paper is concerned with the characterization of nanofabricated particles that are monodisperse in size and shape. It includes the first pharmacokinetic evaluation of PRINT-derived cylinders of 200 nm. PRINT allows for powerful realizations regarding pharmacokinetics of nanoparticles since intersubject variation can be ascribed fully to the subject and not to variations of the nanocarrier. This is a significant step in pharmacokinetic analysis since it eliminates the effect that polydisperse samples can have on biodistribution. This in turn allows us to be able to precisely demonstrate the effect of size, composition, the addition of cargo, modulus, and functionalization on biodistribution, which has never been possible until now. Current efforts are focused on the creation of long-circulating PRINT particles for the eventual use in engineered drug therapies. Results will be reported in due course.

PRINT is the first general, singular method capable of forming organic nanoparticles in which critical design parameters can be precisely and independently tailored bringing a greater understanding of cause-and-effect to the field of nanomedicine. With the unprecedented ability of PRINT technology to control particle size, shape, composition, modulus, cargo, and surface properties, questions such as “what interrelated role does shape, size and mechano-chemico functionality play on the biodistribution of carriers *in vivo*?” and, “how can this understanding translate into more efficacious detection, diagnosis, therapeutic and prevention

strategies?” can finally begin to be answered. As such, PRINT is a significant scientific and technological breakthrough, which will allow the fabrication of heretofore inaccessible populations of nanobiomaterials which are poised to revolutionize and accelerate our translational understanding, detection, and treatment of disease.

3.5 References

- (1) Riley, S.; Business Insights Ltd.: 2006, p 25-26.
- (2) Duncan, R. *Nature Reviews Drug Discovery* **2003**, 2, 347-360.
- (3) Rolland, J. P.; Maynor, B. W.; Euliss, L. E.; Exner, A. E.; Denison, G. M.; DeSimone, J. M. *J Am Chem Soc* **2005**, 127, 10096-10100.
- (4) Huang, Z.; Guo, X.; Li, W.; MacKay, J. A.; Szoka, F. C., Jr. *Journal of the American Chemical Society* **2006**, 128, 60-61.
- (5) Grit, M.; Crommelin, D. J. A. *Chemistry and Physics of Lipids* **1992**, 62, 113-22.
- (6) Woodle, M. C. *Adv Drug Deliv Rev* **1998**, 32, 139-152.
- (7) Papisov, M. I. *Adv Drug Deliv Rev* **1998**, 32, 119-138.
- (8) Allen, T. M.; Hansen, C. B.; de Menezes, D. E. L. *Adv Drug Deliv Rev* **1995**, 16, 267-284.
- (9) Gregoriadis, G. *Trends in Biotechnology* **1995**, 13, 527-37.
- (10) Torchilin, V. P. *Journal of Microencapsulation* **1998**, 15, 1-19.
- (11) Barltrop, J. A.; Owen, T. C.; Cory, A. H.; Cory, J. G. *Bioorganic & Medicinal Chemistry Letters* **1991**, 1, 611-614.
- (12) Wisse, E.; De Leeus, A. M. In *Structural Elements Determining Transport and Exchange Processes in the Liver*; Davis, S. S., Illum, L., McVie, J. G., Tomlinson, E., Eds.; Elsevier Scientific: Amsterdam, 1984, p 1-23.
- (13) Senior, J. H. *Crit Rev Ther Drug Carrier Syst FIELD Full Journal Title:Critical reviews in therapeutic drug carrier systems* **1987**, 3, 123-193.
- (14) Chonn, A.; Semple, S. C.; Cullis, P. R. *Journal of Biological Chemistry* **1995**, 270, 25845-25849.
- (15) Kataoka, K.; Matsumoto, T.; Yokoyama, M.; Okano, T.; Sakurai, Y.; Fukushima, S.; Okamoto, K.; Kwon, G. S. *Journal of Controlled Release* **2000**, 64, 143-153.
- (16) Wolf, H.; Marschall, F.; Scheffold, N.; Clausen, M.; Schramm, M.; Henze, E. *European Journal of Nuclear Medicine* **1993**, 20, 297-301.

- (17) Takakura, Y.; Hashida, M. *Pharmaceutical Research* **1996**, 13, 820-831.
- (18) Moghimi, S. M.; Hunter, A. C.; Murray, J. C. *Pharmacological Reviews* **2001**, 53, 283-318.
- (19) Owens, D. E.; Peppas, N. A. *International Journal of Pharmaceutics* **2006**, 307, 93-102.
- (20) Drummond, D. C.; Meyer, O.; Hong, K.; Kirpotin, D. B.; Papahadjopoulos, D. *Pharmacol Rev* **1999**, 51, 691-743.
- (21) Allen, T. M.; Hansen, C. *Biochimica et Biophysica Acta, Biomembranes* **1991**, 1068, 133-141.

CHAPTER 4

EXPLOITING THE ENHANCED PERMEABILITY AND RETENTION EFFECT FOR TUMOR TARGETING

4.1 Introduction

Cancer is the second most common cause of death in the United States, and accounts for one of every four deaths [1]. Since cancer remains a major threat to human life, major research efforts have been undertaken for both cancer treatment and prevention. Despite the last 50 years of research, the standard treatment is not always successful due to the fact that conventional chemotherapy delivers the anticancer agents indiscriminately to both normal and tumor tissue, resulting in severe negative side effects [2]. Therefore, there is a need for cancer therapeutics to target tumor tissue, minimize interaction with normal tissue and thereby avoid any undesirable side effects. One of the most promising ways of avoiding these undesirable side effects is to deliver the anticancer drug selectively to the tumor tissue by taking advantage of the unique anatomical and pathophysiological characteristics of tumor vasculature that are not observed in normal tissue [3,4]. Tumor abnormalities are particularly evident within the tumor vasculature, which displays hypervascularisation, aberrant architecture, extensive production of vascular permeability factors stimulating extravasation within tumor tissues, and a lack of lymphatic drainage [5]. This phenomenon is referred to as the enhanced permeability and retention (EPR, Figure 4.1) effect was first described by Matsumura and Maeda [6-8].

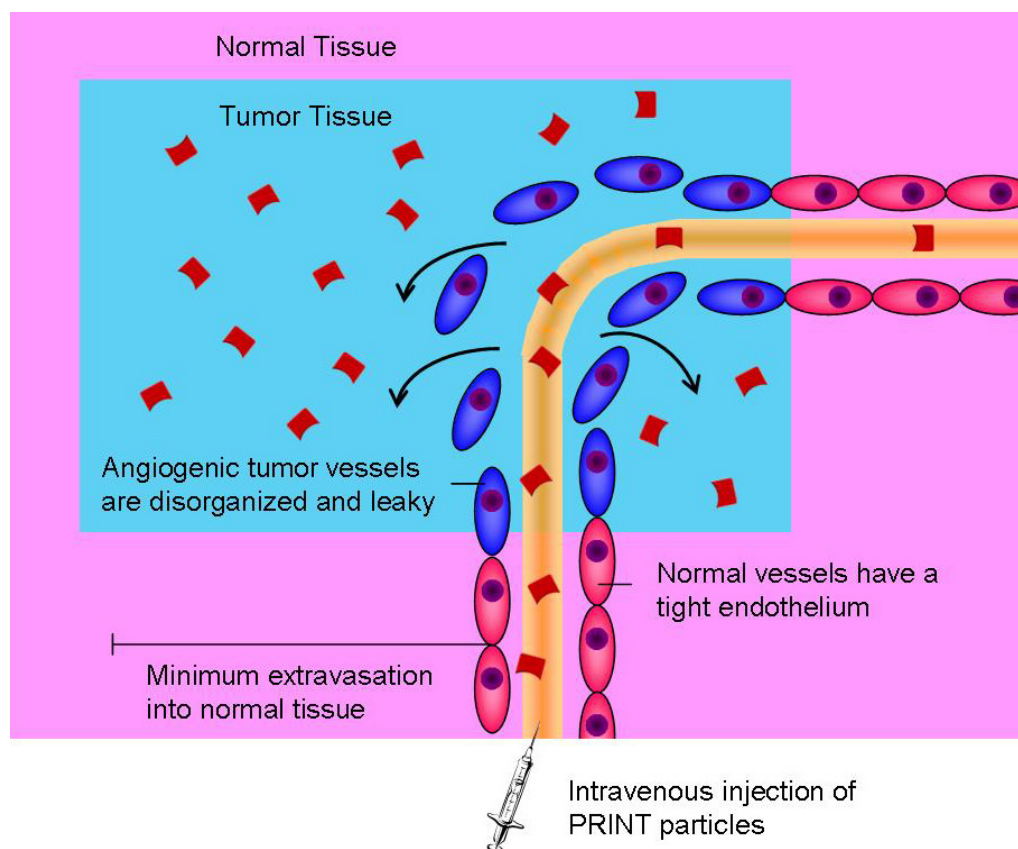


Figure 4.1 Passive tumor targeting of PRINT nanoparticles by EPR effect. Adapted from [9].

Macromolecular delivery vehicles, including micelles, liposomes, polymer conjugates and polymeric particles have taken advantage of the EPR effect as a means to passively target tumor tissue [10-12]. Extensive research is now being conducted to look at the effects of targeted delivery of nanoparticles, in the hopes that targeted delivery will decrease the negative side effects seen on normal tissue, simplify administration protocols, and reduce the cost of the therapies and drug quantities. Currently there are several nanocarriers in the clinic that take advantage passively targeting tumor tissue using the EPR effect, including Doxil® and DaunoXome®, both PEGylated liposomes [13]. In the current studies, the EPR

effect was exploited using cylindrical 200 nm (AR = 1) PRINT particles and a Ramos (Human Burkitt's lymphoma cell line) xenograft model.

4.2 Experimental

4.2.1 Materials

Ramos cells were obtained from the Lineberger comprehensive cancer center tissue culture facility at the University of North Carolina at Chapel Hill. Cell culture media (RPMI 1640) was purchased from GIBCO. CellTiter 96* AQueous One Solution Cell Proliferation Assay (MTS) was purchased from Promega Corporation. The lysis agent used for negative controls in *in vitro* viability studies with Ramos cells was 9% w/v solution of Triton® X-100 in water. Nude mice were purchased from The Jackson Laboratory (nu/nu, stock # 002019). DyLight 800 NHS ester was purchased from Pierce. All animal experiments were conducted in accordance with guidelines set forth by The University of North Carolina at Chapel Hill, and approval was obtained for the completion of these experiments.

4.2.2 Preparation of surface-functionalized PRINT nanoparticles

PRINT nanoparticles (diameter = 200 nm, height = 200 nm) were obtained from Liquidia Technologies, Inc. on raw poly(ethylene terephthalate) (PET) sheeting (50 feet). To facilitate removal of the particles from the raw PET sheet, a physical means for harvesting the particles was utilized. Specifically, a 200 μ L aliquot of water (filtered through a 0.22 μ m Durapore PVDF Membrane) was placed on the

PET sheet and this drop of water was gently moved along the surface of the PET sheet using a cell scraper (Sarstedt cell scraper, 25 cm handle length). The movement of the cell scraper facilitated release of the particles from the PET sheeting. The suspended particles were collected in a Eppendorf tube and spun down on a mini centrifuge (Fisher Scientific) until a particle pellet was visible. After each centrifugation step, the supernatant was removed via aspiration and the particle pellet was redispersed in 1.5 mL of fresh filtered water by vortexing for 10 minutes followed by centrifugation for an additional 30 minutes. This process was repeated once more, then following aspiration, the particles were redispersed in 0.2 mL of anhydrous dimethyl formamide (DMF) by sonicating the dispersion for 5 minutes on a Branson 2510 sonicator (Fisher Scientific). In total, seventeen feet of cylindrical 200 nm (AR =1) particles on raw PET was harvested, yielding 17.51 mg of 200 nm particles in 15 Eppendorf tubes.

Monomer	Function	Wt %
PEG ₇₀₀ diacrylate	Cross-linking agent	78
2-Aminoethyl methacrylate hydrochloride	Chemical handle	20
Fluorescein-o-acrylate	Fluorophore	1
1-Hydroxycyclohexyl phenyl ketone	Initiator	1

Table 4.1 Particle composition

All of the particle dispersions were collected into one 20 mL scintillation vial, using 0.1 mL of anhydrous DMF to rinse the Eppendorf tubes, facilitating optimal transfer between vials. Next, 0.6 mL of triethylamine was added to the particle

dispersion. Separately, a solution of methoxypolyethylene glycol 5000 succinate N-succinimidyl ester (NHS-PEG 5K) was prepared by the addition 60.2 mg of NHS-PEG 5K to 2 mL of anhydrous DMF. This NHS-PEG 5K solution was added to the particle dispersion (total volume of DMF = 6.5 mL), and the solution was placed in the dark on the vortex overnight. The following morning, 0.6 mL of NHS-DyLight 800 (1 mg/mL in anhydrous DMF) was added to the particle dispersion. The particles were then covered in aluminum foil (to protect the fluorophores from photobleaching), placed back on the vortex, and allowed to react for an additional 6 hours.

The particles were purified by transferring the contents of the scintillation vial to 4 Eppendorf tubes. The particle dispersions were spun down on a mini centrifuge for 15 minutes. After each centrifugation step, the supernatant was removed via aspiration and the particle pellet was redispersed in 1.5 mL of fresh filtered acetone by vortexing for 10 minutes followed by centrifugation for an additional 10 minutes. The final two rinses were done with filtered water, in place of the filtered acetone. At this stage, the particle concentration was determined using the thermogravimetric analyzer Pyris 1 TGA (Perkin Elmer) and 10 μ L of the particle dispersion. Finally, the particles were diluted such that the final concentration of particles was 3 mg/mL in PBS with 5 wt % dextrose and 0.1 wt% Pluronic F108.

4.2.3 Particle size analysis of PRINT nanoparticles using scanning electron microscopy (in the dry state)

The size of PRINT nanoparticles was analyzed via scanning electron microscopy (Hitachi model S-4700). Particle dispersions were prepared at

concentrations of 0.5 mg/mL, and a drop of this solution was placed on a glass slide. The drop was then allowed to dry, and the glass slide was coated with 1.5 nm of Pd/Au alloy using a Cressington 108 auto sputter coater (Cressington Scientific Instruments Ltd.). The Pd/Au coated glass slide was then adhered to the sample holder using double-sided adhesive tape, and placed inside the vacuum chamber of the SEM and observed under low vacuum (10^{-6} Torr).

4.2.4 Particle size analysis of PRINT nanoparticles using dynamic light scattering (in suspension)

The size and polydispersity of PRINT nanoparticles was analyzed via dynamic light scattering (DLS) using a 90Plus Particle Size Analyzer (Brookhaven Instruments Corporation). The particles were dispersed in PBS at a concentration of 0.5 mg/mL and measured without filtration at 25 °C.

4.2.5 Zeta potential measurements

The zeta potential of PRINT nanoparticles was measured using a ZetaPlus Zeta Potential Analyzer (Brookhaven Instruments Corporation). The nanoparticles were dispersed in water at a concentration of 0.3 mg/mL and the zeta potential was measured.

4.2.6 *In vitro* internalization

Ramos cells were seeded in 96 well plate at 2×10^5 per well in serum-free RPMI 1640. Following this, 200 nm PRINT particles were vortexed and diluted in

serum-free RPMI 1640. Cells were then dosed with particles at the desired concentrations for 4 hours (50 μ L/well). At the end of dosing cells were spun down at 1200 rpm for 4 minutes and the medium was aspirated off the cells. For uptake assays, cells were treated with 0.1% trypan blue at room temperature for 3 min to quench the extracellular fluorescence from non-internalized particles [14]. Finally, cells were washed and resuspended in DPBS and analyzed on a Cyan ADP flow cytometer (DakoCytomation). Data were analyzed with Summit 4.3 software.

4.2.7 *In vitro* cytotoxicity

Ramos cells were seeded in 25 μ L of serum-free media RPMI 1640 at a density of 2×10^5 cells per well into a 96-well microtitre plate. The particle dispersions, at the appropriate concentrations, were added to the wells (25 μ L per well in PBS with 5 wt% dextrose and 0.1 wt % Pluronic F108). Ramos cells were incubated with the PRINT particles for 4 h at 37 °C in a humidified 5% CO₂ atmosphere. After the incubation period, cells were spun at 1200 rpm for 4 minutes and the medium was replaced with complete growth medium (RPMI 1640 with 10% fetal bovine serum, Penicillin/streptomycin, and 2mM L-Glutamine). The cells were incubated for another 72 hours at 37 °C in a humidified 5% CO₂ atmosphere. For the MTS assay, 100 μ L of fresh complete growth medium was added to replace the old medium, then the MTS assay solution (Cell Titer 96[®] AQueous One Solution Cell Proliferation Assay reagent) was added (20 μ L per well) into each well. The cells were then incubated at 37°C in a humidified 5% CO₂ atmosphere until color was well developed. The optical density at 490 nm was measured using a BioRad Model

3550 microplate reader (BioRad Laboratories). The viability of the cells exposed to the cylindrical 200 nm PRINT particles was expressed as a percentage of the viability of cells grown in the absence of particles.

4.2.8 Hemolysis assay using 200 nm PEGylated PRINT particles

The hemolysis assay used has been described elsewhere [15,16]. Briefly, blood from was collected in Li-heparin tubes to prevent coagulation. The blood was centrifuged for 15 minutes at 800 g, and the supernatant was collected and used to determine the plasma free hemoglobin content (PFB). This assay includes both a positive (Triton X-100, 1 wt % in sterile, distilled water) and negative control (poly(ethylene glycol), MW = 8000 g/mol, 40 wt % in sterile, distilled water). Particles incubated with blood, and particles incubated with PBS were added to the 96 well plate. Next, a calibration curve was measured using prepared hemoglobin standards having concentrations ranging from 0.025 to 80 mg/mL. All of the aforementioned samples were repeated such that n=4. The absorbance at 540 nm was measured and used to determine the hemoglobin concentration. The amount of hemoglobin present in the particle samples was compared to those obtained for the positive and negative controls, and expressed as a percent of hemolysis.

4.2.9 Biodistribution of fluorescently-tagged 200 nm PEGylated PRINT particles

Athymic mice were housed under specific pathogen-free conditions for a total of 3 weeks and were used at 9 weeks of age (~18 g). Mice were given 8 days to

acclimate to the new housing environment, at which point the animals were injected with 1×10^7 Ramos cells subcutaneously in the right flank of the mice. After 14 days, and when the tumors reached $\sim 60 - 100 \text{ mm}^3$, mice ($n=4$) were injected intravenously via bolus tail vein administration with 0.3 mg of DyLight 800-labeled PRINT particles in 100 μL of PBS (phosphate buffered saline, Sigma-Aldrich) with 5 wt % dextrose and 0.1 wt % Pluronic F108. At 10 min, 1 h, and 6 h after dosing, groups of four mice were anesthetized by isoflurane, and imaged on the IVIS-100 Xenogen imaging system (Xenogen Corporation, Caliper Life Sciences). Images were collected with the field of view set to 'B' (where one animal is visible at a time) using a 30 second exposure, with medium binning, the f/stop set to 4, and the ICG filter set (excitation $\lambda = 710 - 760 \text{ nm}$, emission $\lambda = 810 - 875 \text{ nm}$). A background scans was acquired in the absence of mice, but with all of the appropriate settings. Blood was collected using a submandibular bleed. Samples of blood and organs harvested (tumor, liver, kidneys, spleen, lungs, and heart) were counted to determine the total fluorescence using the IVIS-100 Xenogen imaging system. Total fluorescence was calculated on images using the Living Image® 3.0 software, by selecting an area, depicted the region of interest, taking the measurement (under ROI tools), and recording the total photons in that region (in $\text{p/sec/cm}^2/\text{sr}$). Photons are the unit of choice, as they are a calibrated measurement of the photon emission from the subject.

4.2.10 Dosing study using fluorescently-tagged 200 nm PEGylated PRINT particles

The dosing study was completed with the same procedures as above, except particle injections were made via bolus tail vein administration with 0.6 mg of DyLight 800-labeled PRINT particles in 200 μ L of PBS with 5 wt % dextrose and 0.1 wt % Pluronic F108.

4.3 Results and Discussion

In these studies, the particle composition was engineered to produce biologically relevant delivery vectors with the ability to post-functionalize the surface. 2-Aminoethyl methacrylate hydrochloride (AEM) was chosen as a chemical handle for surface modification. Here, both NHS-PEG 5K and NHS-DyLight 800 were added to the particles' surface. The approach used was to react the surface AEM groups with NHS-PEG 5K, then to add to NHS-DyLight 800 to quench any remaining amine groups that remained on the particle surface. The PEG moiety was added to impart biocompatibility and increase circulation times *in vivo*, and the DyLight 800 was added so that visualization by fluorescence was possible. Using a wavelength in the near-infrared proved to be optimal for avoiding high autofluorescence signals that occur when measuring living systems at < 800 nm. Specifically, a near-infrared dye was chosen since it is known that the absorption of light through tissue is low in that region yielding superior signal to noise ratios [17]. Further sensitivity was gained by feeding the mice a low-chlorophyll diet to reduce autofluorescence that was observed in the intestinal region.

For these experiments, post-functionalization was completed in a sequential fashion, such that PEG 5K was reacted with the surface amines, then NHS-DyLight 800 was added to the reaction mixture to react with any remaining amines on the particle surface. This strategy proved useful for many reasons: i) by adding the PEG reagent first, a maximum number of amine groups can be conjugated to the PEG moiety, ii) particles used for *in vivo* studies should possess a negative zeta potential, therefore any remaining surface amine groups must be quenched, and in this chemistry, the remaining amines are quenched with NHS-DyLight 800, iii) this chemistry allows for a sufficient number of fluorophores to bind to the particles surface, such that the particles are visible *in vivo*.

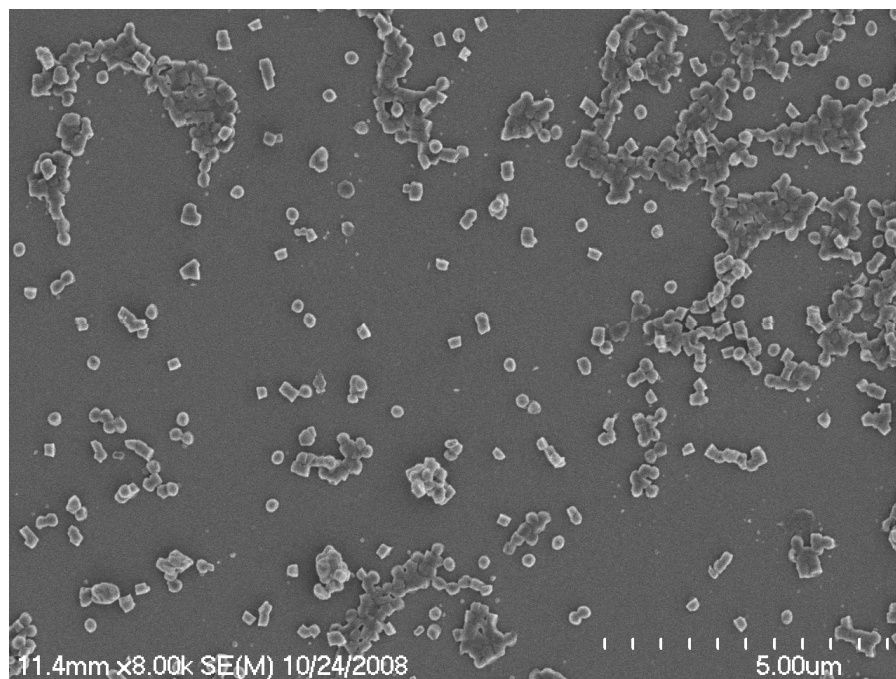


Figure 4.2 Scanning electron micrograph of 200 nm PRINT particles used in the present study

The 200 nm (AR = 1) particles were characterized by SEM, DLS, and zeta potential (Table 4.2). SEM characterization revealed particles with a height of 146 ± 17 nm, and a width of 199 ± 16 nm (Figure 4.2). Dynamic light scattering showed similar sizes, with a mean diameter of 225 nm, and a polydispersity of 0.005 (Figure 4.3). The surface charge of these particles, after PEGylation and reaction with DyLight 800 was found to be -26 ± 2 mV. The zeta potential measured before post-functionalization was 33 ± 3 mV (Figure 4.4).

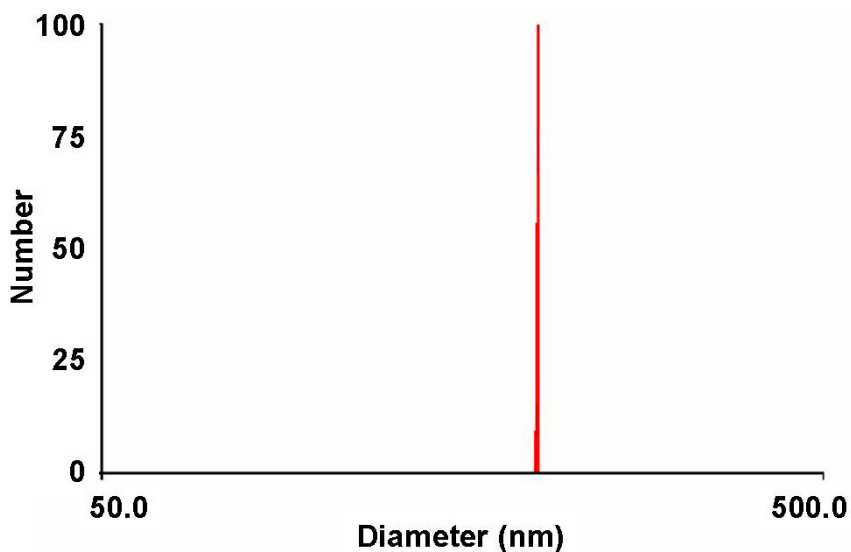


Figure 4.3 Dynamic light scattering of 200 nm PRINT particles that have been post-functionalized with PEG 5K and DyLight 800. The mean diameter was measured at 225 nm, with a polydispersity of 0.005.

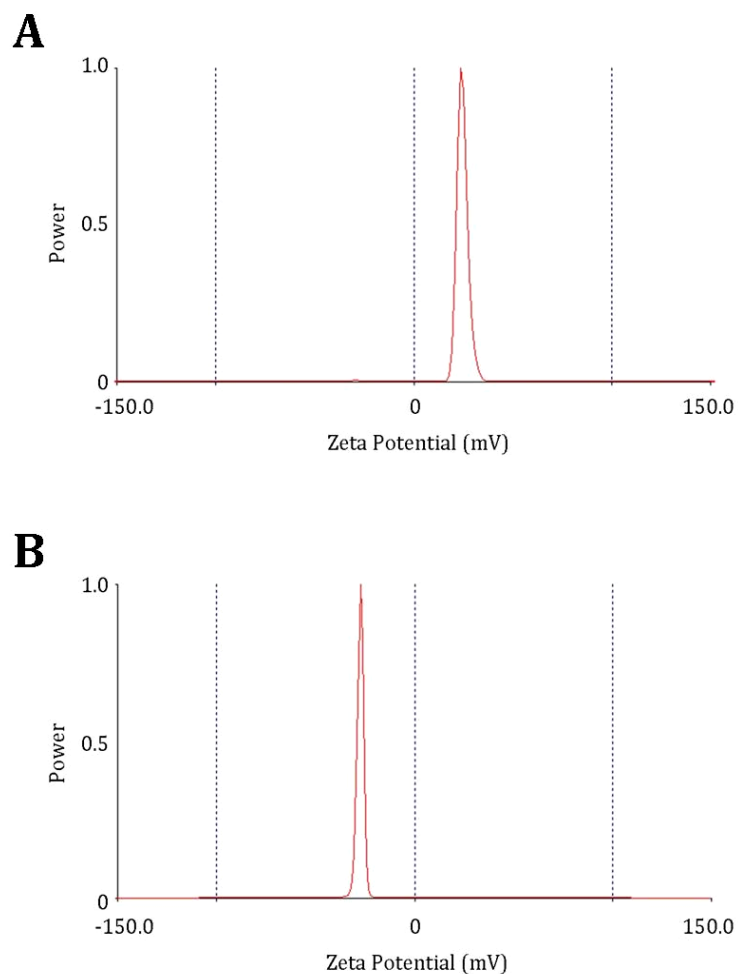


Figure 4.4 Zeta potential analysis of 200 nm PRINT particles. A) Purified particles before any post-functionalization (zeta potential = 33 ± 3 mV). B) Purified particles that have been post-functionalized with PEG 5K and DyLight 800 (zeta potential = -26 ± 2 mV).

Method	Parameter
SEM	Width: 199 ± 16 nm Height: 146 ± 17 nm
DLS	Diameter: 225 ± 11 nm
Zeta Potential	Before post-reactions: 33 ± 3 mV After post-reactions: -26 ± 2 mV

Table 4.2 Particle characterization

The *in vitro* internalization and cytotoxicity of 200 nm (AR = 1) PEGylated PRINT particles was examined using Ramos (Human Burkitt's lymphoma) cells (Figure 4.5). These suspension cells did not appear to internalize the 200 nm particles to any high extent. Two control particles were synthesized, a batch of positively charged particles and a batch of negatively charged particles. The positively charged particles are simply unfunctionalized particles with the surface amines left unreacted (Figure 4.4A), and the negatively charged particles are the acetylated version of these particles (zeta potential = -24 ± 4 mV). As reported previously, the positively charged particles were internalized to the highest extent, the negatively charged particles were internalized less than the positively charged particles, and the PEGylated particles were internalized showing similar trends as the negatively charged particles [18,19]. This follows the expected outcome since the PEGylated particles are negatively charged particles possess a negative zeta potential.

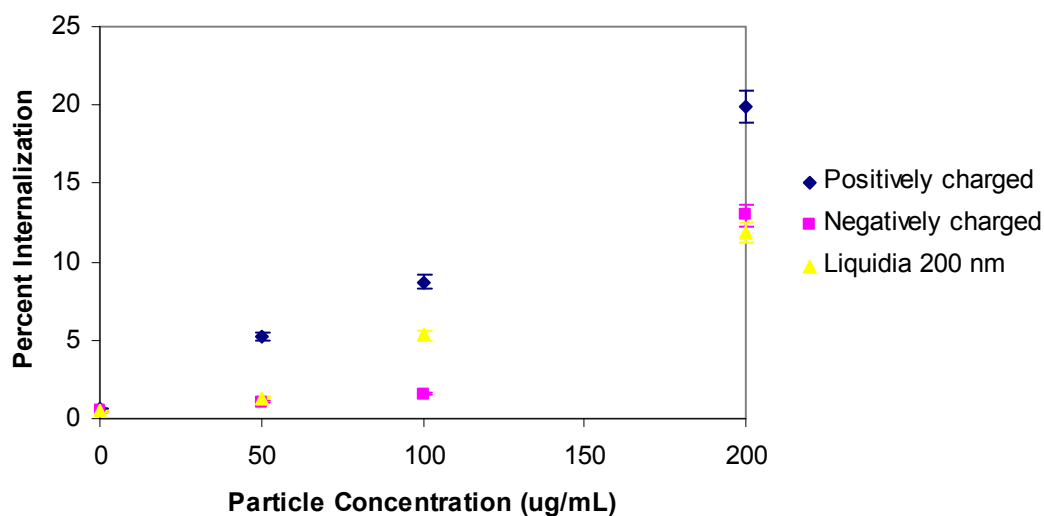


Figure 4.5 *In vitro* internalization profiles of PEGylated 200 nm particles with a negative zeta potential using Ramos cells. Both the positively charged particle and negatively charged particle controls are included. Overall, the internalization of all particle sets was low.

The cytotoxicity of the 200 nm (AR = 1) particles was tested *in vitro* (Figure 4.6) and was found to be low. A very small amount of cell death was observed at high particle concentrations (200 $\mu\text{g/mL}$, which is equal to 1.5×10^5 particles/Ramos cell). Since these particles proved to be non-toxic at concentrations used for *in vivo* studies, whole animal fluorescent studies could be conducted.

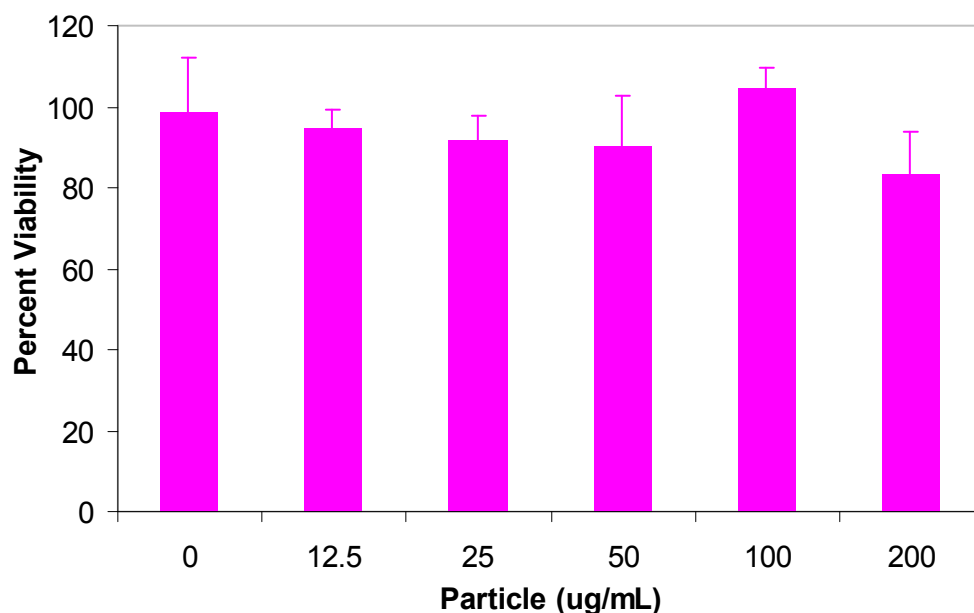


Figure 4.6 *In vitro* cytotoxicity profiles (MTS Assay) of PEGylated 200 nm particles with a negative zeta potential using Ramos cells.

Analyzing the hemolytic properties of nanoparticles is an alternative method for measuring their toxicity. The hemolysis assay is commonly used for preclinical evaluation of nanoparticles used in medical applications [16]. Hemolysis is defined as the destruction of red blood cells. Measuring the hemolytic properties begins to illustrate how nanoparticles interact with blood components. In these studies, Triton-X 100 was used as a positive control since it is known to be hemolytic [20], and PEG (average molecular weight of 8000 g/mol) was used as the negative control, as it is known to be biocompatible. The hemolysis assay conducted with PRINT particles used mouse blood, and showed favorable results (Figure 4.7). The 200 nm post-PEGylated PRINT particles showed hemolytic properties similar to that of PEG, the negative control. This indicates that the particles are not causing any rupturing

of the red blood cells once introduced *in vivo*. In addition, positively charged particles (base particle, unfuntionctionalized) and negatively charged particles (base particles with all the surface amine groups acetylated) were tested for their hemolytic properties. All three PRINT particles examined showed little to no hemolysis of red blood cells.

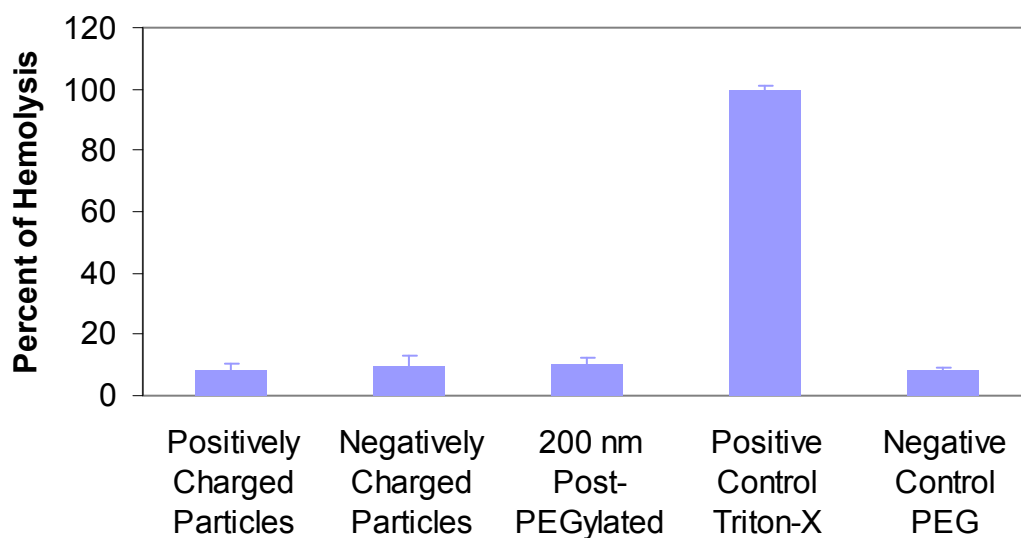


Figure 4.7 *In vitro* hemolysis assay of PEGylated 200 nm particles with a negative zeta potential using human blood. Here, the positive control is Triton-X 100, which is known to lyse red blood cells, and the negative control is poly(ethylene glycol) (MW = 8000 g/mol).

Whole animal imaging was conducted using an IVIS-100 Xenogen imaging system (Figure 4.8). Nude mice bearing Ramos tumors were administered with 200 nm (AR = 1) PRINT particles via a bolus tail vein injection of 20 mg/kg (300 μ g of particles in 100 μ L of PBS with 5 wt % dextrose and 0.1 wt% pluronic F108). The mean tumor size at the time of particle injection was 0.72 cm³ (Figure 4.9, range: 0.2 – 1.2 cm³).

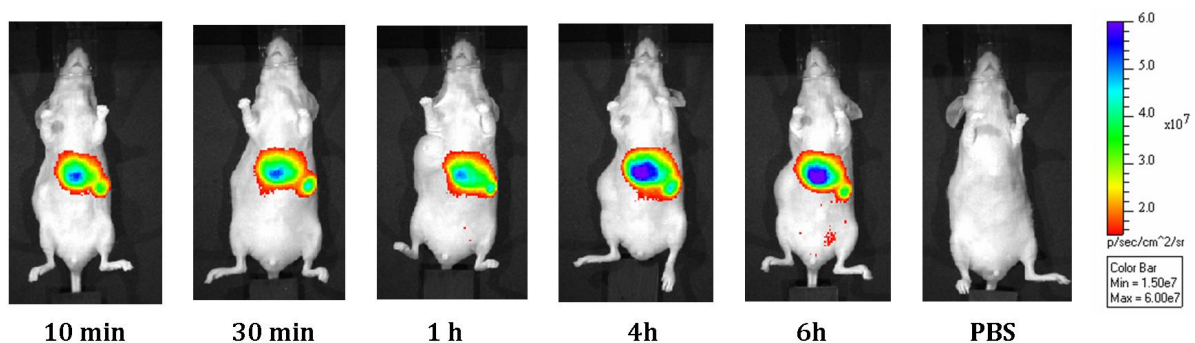


Figure 4.8 Whole animal imaging on the IVIS-100 Xenogen imaging system. 200 nm PRINT particles were injected via the tail vein in nude mice bearing Ramos tumors. The major organs of accumulation (i.e. the liver and spleen) were visible as early as 10 minutes.

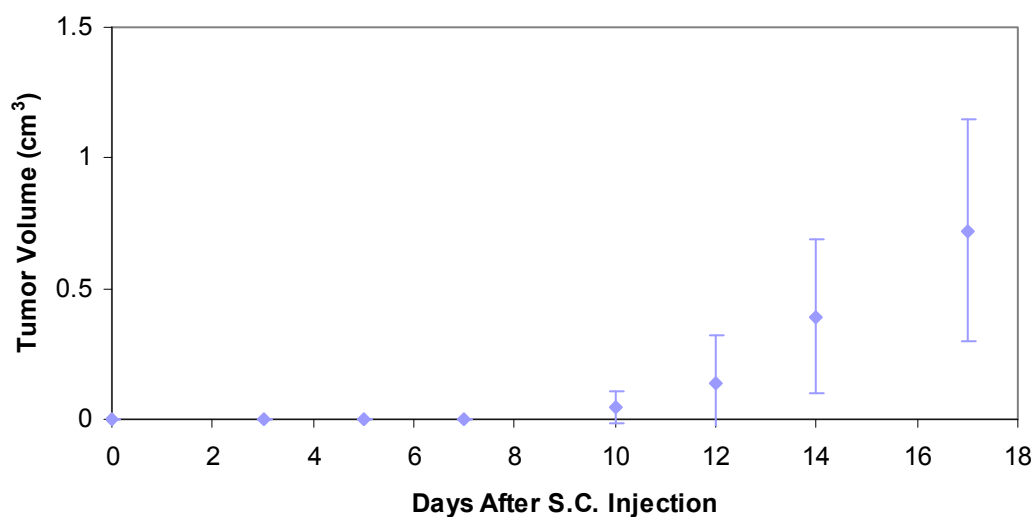


Figure 4.9 Tumor growth rate as a function of time. 10^7 cells were injected subcutaneously into the right flank of nude mice. Experiments were conducted at day 14 post-inoculation, where the average tumor volume was 0.72 cm^3 .

The particle accumulation was measured as a percent of recovered dose at 10 min, 1 h, and 6 h post-intravenous injection (Figure 4.10). The 200 nm (AR = 1)

particles were mainly distributed in the clearance organs (i.e. liver and spleen) throughout the time course of the study. Organ distribution values were obtained from total photon counts calculated from excised organs. Figure 4.11 shows the fluorescence observed from organs removed from a mouse at 6 h post-injection (Figure 4.11A). In addition, organs were removed from a mouse injected with PBS (with 5 wt% dextrose and 0.1 wt% pluronic F108) and were used as a control (Figure 4.11B). The rapid accumulation of the particles in the liver and the spleen indicates that after intravenous administration, the particles were quickly recognized as foreign and removed from systemic circulation by the reticuloendothelial system (RES). The particles used in the present study possess a PEG coating, with a molecular weight of 5000 g/mol. From the breadth of liposomal literature, it is known that in order for a coating on a particle to provide stealth properties, it is not only the molecular weight of the PEG coating, but also the density [21,22]. Since this was the first *in vivo* study of a post-PEGylated particle, it is not surprising that the steric coat on the PRINT particles provided was not sufficient for long-circulating particles. It has been suggested that the optimal coating for the creation of long-circulating liposomes is 2-5 kDa PEG [23,24]. It should be noted that these cylindrical 200 nm PRINT particles are very different from liposomal carriers, and more attention should be given to coatings on the particles' surface in the design and eventual realization of long-circulating particles. The current particle PEG coating may not offer a radius of protection that is sufficient to effectively block the adsorption of opsonic proteins. Once opsonization occurs, the particles are destined to be cleared by Kupffer cells in the liver and splenic macrophages.

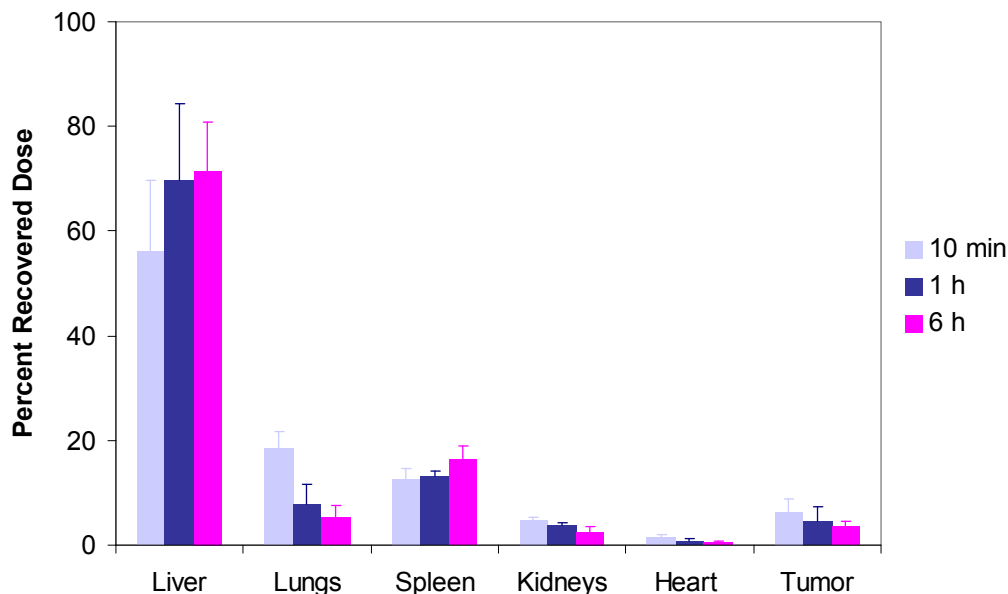


Figure 4.10 Biodistribution of 200 nm PRINT particle in nude mice bearing Ramos tumors. The organ accumulation is expressed as a percent of recovered dose after animals were sacrificed at 10 min, 1 h, and 6 h post-intravenous injection. The organ data is presented as a mean \pm SD with $n=4$.

The particle accumulation seen in the lungs is likely due to capillary trapment of particle aggregates found in the bloodstream upon injection. Nanoparticles will naturally tend to agglomerate into larger particles that are micron in size, and this can occur both prior to injection and also once injected into the bloodstream. The micron sized aggregates tend to get trapped in the vasculature of the lung. It should be noted that if opsonisation occurs on the surface of the particles, this signals to phagocytic macrophages to internalize the particles. The net result of this process is the accumulation of particles in the liver, spleen, and to a lesser extent the lungs (i.e. the reticuloendothelial system (RES) clearance organs) [25]. Therefore, the lung accumulation is likely due to a combination of the macrophage accumulation of particles as well as the particle aggregation and subsequent trapping of the

aggregates in the lung vasculature. The clearance of particles by the RES has the effect of decreasing the circulation time of the nanoparticles *in vivo* and lessens the chances of the particle reaching its target.

Detectable fluorescent signals were not observed in the tumor region based on whole animal imaging profiles. However, once the major organs were excised from the animals, it became apparent that the tumor tissue did indeed produce an observable signal (Figure 4.11). This is probably due to the fact that the signals obtained from the RES clearance organs were so intense that they diminished any signal from being observed from tissues with only a fraction of the accumulation. At any point examined (from 10 minutes to 6 hours), the tumor tissue possessed ~ 3.5-6.5 % of the recovered dose. This finding reinforces the EPR effect of nanoparticles, with PEGylated 200 nm (AR = 1) PRINT particles accumulating in the highly vascularized tumor tissue.

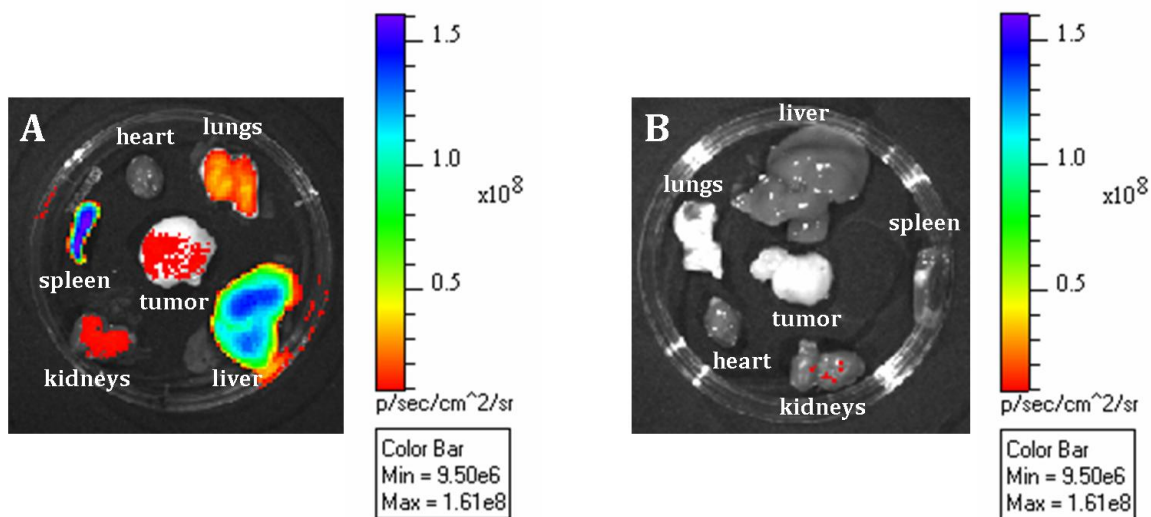


Figure 4.11 Organ distribution of 200 nm (AR = 1) PRINT particles (A) versus the PBS control (B). Organs were excised from both animal groups at 6 h post-injection.

The organ accumulation observed was similar to previous results obtained from a healthy mouse biodistribution study [26]. In our previous work, the particle matrix as well as the surface properties were slightly modified from those presented here, however the distribution remains the same. The healthy mouse biodistribution was performed on particles with 20% (w/w) PEG₁₀₀₀ monomethyl ether monomethacrylate mixed into the particle matrix, whereas the EPR studies were completed with particles that had been post-functionalized on the surface with PEG 5K. These results may suggest that the current size of the particle does not allow for multiple passes through the body and gets trapped in the liver within the initial passes, where fenestrae can be as large as 150 nm [23,27]. This may be independent of particle matrix composition and surface properties, at this size. However, both particle compositions and surface properties were quite similar, and therefore a more in depth examination of size, matrix composition and surface chemistry must be brought forth before any conclusions can be drawn.

A second study was completed to determine the effects of doubling the particle dose. In the previous study, an injection of 300 µg of particles in 100 µL of PBS with 5 wt % dextrose and 0.1 wt% pluronic F108 was made. The dosing study examined the effect of injecting 600 µg of particles in 200 µL of PBS with 5 wt % dextrose and 0.1 wt% pluronic F108, a dosing of 40 mg/kg. The results at 6h post-injection are described in Figure 4.12-4.14. When comparing the two dosages as a function of percent recovered dose, the relative organ accumulation appears to be similar, however, if the data are compared as a function of total fluorescence, a higher than expected accumulation was observed in the lungs, heart, tumor and

kidneys (Figure 4.13, Table 4.3). This observation was an exciting one, as the amount of particle accumulation in the heart, and tumor did not scale linearly with the amount of particles injected, pointing to particles that are remaining in circulation longer and are therefore reaching their target (the tumor tissue) more effectively. Again, the tumor localization is mainly dependent on the EPR effect. In this study, a tumor accumulation of ~ 3.5-5 % of the recovered dose was observed. The non-linear accumulation in the lungs may point to particle aggregation once in the bloodstream, as the same particle solution was injected at the higher dosage, it was simply twice the volume. Unfortunately, the dosing study was only done with 2 mice at the higher dose (40 mg/kg, and n=4 at the 20 mg/kg dose), and therefore a more thorough investigation needs to be completed to assess the effect of dosing on tumor accumulation.

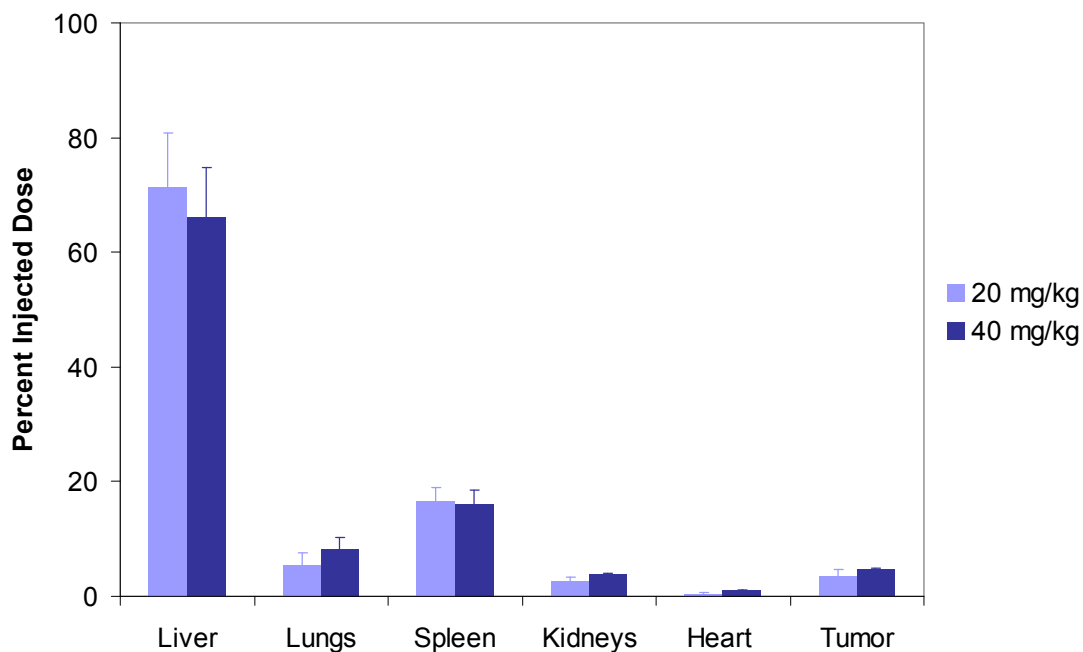


Figure 4.12 The effect of dosage as a function of percent recovered dose at 6 h post-injection.

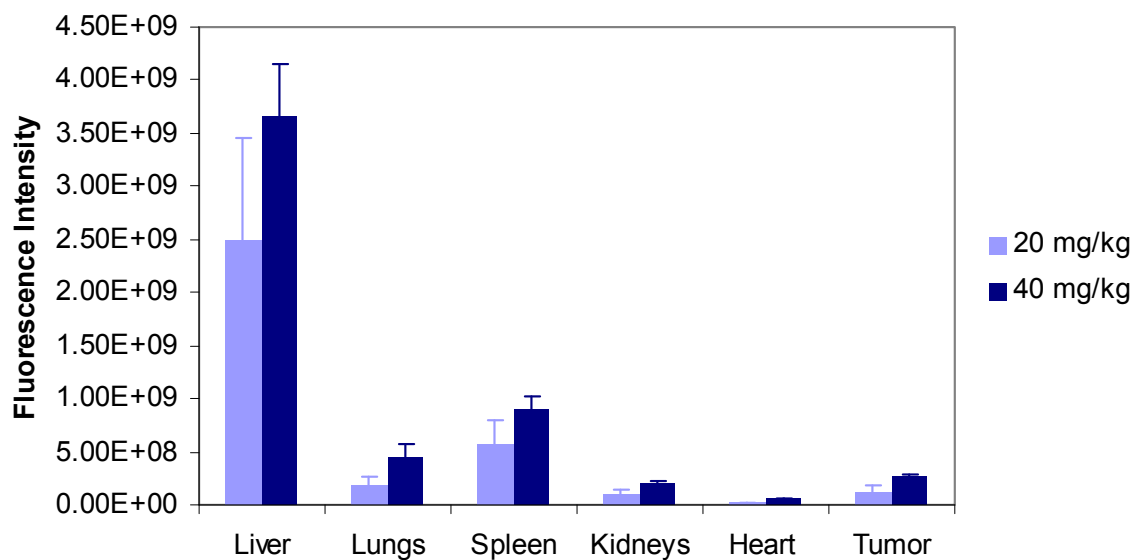


Figure 4.13 The effect of dosage as a function of total fluorescence intensity at 6 h post-injection.

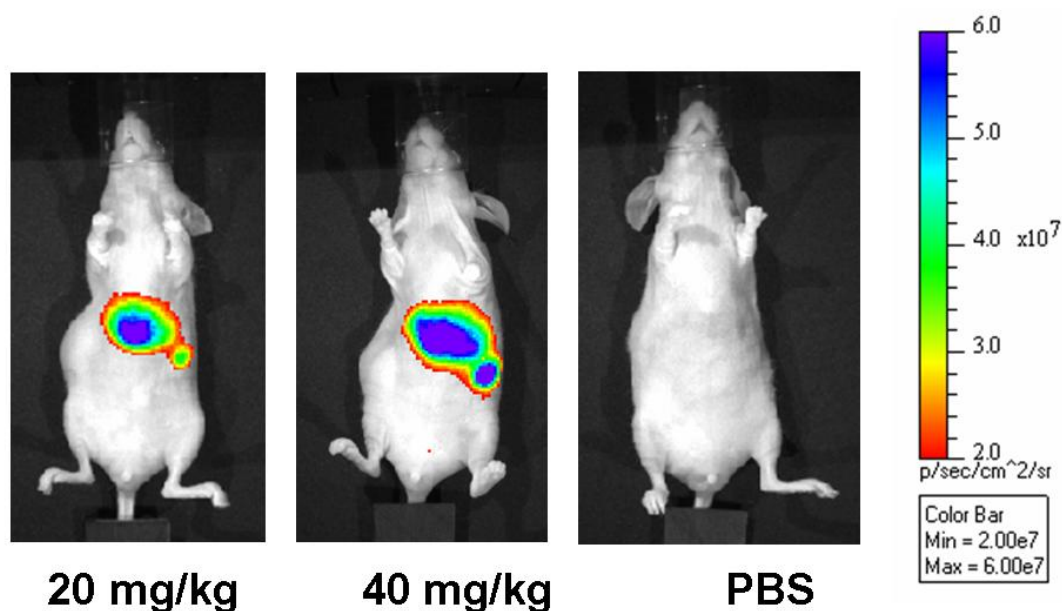


Figure 4.14 Whole animal imaging on the IVIS-100 Xenogen imaging system as a function of dosage.

Tissue	Relative Increase
Liver	1.8
Lungs	3
Spleen	1.8
Kidneys	2.8
Heart	3.8
Tumor	2.6

Table 4.3 The effect of dosing at 6 h post-injection. In these experiments, it was found that not all organ accumulations scaled linearly with a doubling of dose (i.e. lungs, kidneys, heart, and tumor).

4.4 Conclusions

In vivo fluorescent imaging is a powerful tool for detecting the location of fluorescently labeled 200 nm (AR = 1) PRINT particles. Unfortunately, only the

major organs of accumulation were observed based on whole animal imaging. Once organs of interest were excised from the animals, then a total photon count per organ could be quantified. In this work, tumor accumulation due to the EPR effect was observed (~3.5-6.5 % of the recovered dose) using a Ramos tumor model. Based on these results, further studies are required in the search for RES-evading long-circulating PRINT nanoparticles.

4.5 References

- (1) www.cancer.org 11/1/08.
- (2) Leaf, C. *Fortune* **2004**, 149, 84-86.
- (3) Maeda, H.; Wu, J.; Sawa, T.; Matsumura, Y.; Hori, K. *Journal of Controlled Release* **2000**, 65, 271-284.
- (4) Maeda, H. *Advances in Enzyme Regulation* **2001**, 41, 189-207.
- (5) Greish, K. *Journal of Drug Targeting* **2007**, 15, 457-464.
- (6) Matsumura, Y.; Maesa, H. *Cancer Research* **1986**, 46, 6387-6392.
- (7) Maeda, H.; Matsumura, Y. *Critical Reviews in Therapeutic Drug Carrier Systems* **1989**, 6, 193-210.
- (8) Maeda, H.; Seymour, L. W.; Miyamoto, Y. *Bioconjugate Chemistry* **1992**, 3, 357-362.
- (9) Duncan, R. *Nature Reviews Drug Discovery* **2003**, 2, 347-360.
- (10) Li, S.-D.; Huang, L. *Annals of the New York Academy of Sciences* **2006**, 1082, 1-8.
- (11) Muggia, F. *Clinical Cancer Research* **1999**, 5, 7-8.
- (12) Son, Y. J.; Jang, J.-S.; Cho, Y. W.; Chung, H.; Park, R.-W.; Kwon, I. C.; Kim, I.-S.; Park, J. Y.; Seo, S. B.; Park, C. R.; Jeong, S. Y. *Journal of Controlled Release* **2003**, 91, 132-145.
- (13) Iyer, A. K.; Khaled, G.; Fang, J.; Maeda, H. *Drug Discovery Today* **2006**, 11, 812-818.
- (14) Fattorossi, A.; Nisini, R.; Pizzolo, J. G.; Damelio, R. *Cytometry* **1989**, 10, 320-325.
- (15) *Standard practice for assessment of hemolytic properties of materials*; ASTM International: West Conshohocken, PA, 2000.
- (16) Dobrovoiskaia, M. A.; Clogston, J. D.; Neun, B. W.; Hall, J. B.; Patri, A. K.; McNeil, S. E. *Nano Letters* **2008**, 8, 2180-2187.
- (17) Troy, T.; Jekic-McMullen, D.; Sambucetti, L.; Rice, B. *Molecular Imaging* **2004**, 3, 9-23.

- (18) Gratton, S. E. A.; Napier, M. E.; Ropp, P. A.; Tian, S.; DeSimone, J. M. *Pharmaceutical Research* **2007**, *In Press*.
- (19) Gratton, S. E. A.; Ropp, P. A.; Pohlhaus, P. D.; Luft, J. C.; Madden, V. J.; Napier, M. E.; DeSimone, J. M. *Proceedings of the National Academy of Sciences of the United States of America* **2008**, *105*, 11613-11618.
- (20) Duguid, J. G.; Li, C.; Shi, M.; Logan, M. J.; Alila, H.; Rolland, A.; Tomlinson, E.; Sparrow, J. T.; Smith, L. C. *Biophysical Journal* **1998**, *74*, 2802-2814.
- (21) Owens, D. E.; Peppas, N. A. *International Journal of Pharmaceutics* **2006**, *307*, 93-102.
- (22) Pirollo, K. F.; Chang, E. H. *Trends in Biotechnology* **2008**, *26*, 552-558.
- (23) Moghimi, S. M.; Hunter, A. C.; Murray, J. C. *Pharmacological Reviews* **2001**, *53*, 283-318.
- (24) Owens, D. E.; Peppas, N. A. *Int. J. Pharm.* **2006**, *307*, 93-102.
- (25) Gref, R.; Domb, A.; Quellec, P.; Blunk, T.; Muller, R. H.; Verbavatz, J. M.; Langer, R. *Advanced Drug Delivery Reviews* **1995**, *16*, 215-233.
- (26) Gratton, S. E. A.; Pohlhaus, P. D.; Lee, J.; Guo, J.; Cho, M. J.; DeSimone, J. M. *Journal of Controlled Release* **2007**, *121*, 10-18.
- (27) Braet, F.; Dezanger, R.; Baekeland, M.; Crabbe, E.; van der Smissen, P.; Wisse, E. *Hepatology* **1995**, *21*, 180-189.

CHAPTER 5

SUMMARY OF CONCLUSIONS AND RECOMMENDATIONS FOR FUTURE WORK

5.1 Summary of conclusions

Establishing the interdependency of the size, shape, deformability and surface chemistry of micro- and nanoparticles *in vitro* and *in vivo* over length scales ranging from cells to tissues to the entire organism are needed by many different research communities including environmental regulators, pulmonologists, oncologists, pharmaceutical scientists, toxicologists, cell biologists and dermatologists. There is a need for definitive answers related to particle biodistribution maps based on changes in particle size, shape, deformability, and surface chemistry using “calibration quality” particles. These nanofabricated tools (e.g. precisely defined particles) hold significant promise to provide insight into the fundamentals of cellular and biological processes as they can yield essential insights into the design of effective vectors for use in nanomedicine. Beyond understanding the biodistribution of particles delivered via parenteral routes, particle size, shape, deformability and surface chemistry should play a very significant role in understanding the mechanisms associated with particle inhalation, either intentionally for use as a therapeutic or during environmental exposure.

5.1.1 Cellular uptake mechanisms of non-targeted organic PRINT particles

By taking advantage of the versatility of the PRINT process, calibration quality particles can be fabricated with complete control over the surface charge, size, and shape and their internalization can be monitored to determine the impact these parameters have on the mechanism of cellular internalization [1]. Several studies have addressed the role of shape and size on cellular internalization [2-4]. Using

commercial poly(styrene) microspheres and murine B16F10 melanoma cells Rejman and co-workers have shown that spheres with a diameter less than 200 nm utilized a clathrin-mediated mechanism for cellular internalization whereas particles greater than 500 nm were endocytosed using a caveolae-mediated mechanism [3]. No internalization was not observed with particle sizes greater than 1 μm . Furthermore, surface charge was shown to affect particle uptake with net cationically charged particles being internalized by clathrin-coated pits while anionic particles were endocytosed via caveolae when added to HeLa cells [5]. Thus size and charge play critical roles in determining which endocytic pathway is used for particle internalization. Few studies have been conducted examining the intracellular internalization of non-spherical organic nanoparticles [6-8].

Given this, a series of PRINT particles were fabricated to characterize the cellular internalization mechanisms of non-targeted organic nanoparticles as a function of size, shape, and surface charge (cationic, anionic) in HeLa cells. It was found that particle shape greatly affects cellular internalization. Particles with a diameter of 200 nm and a height of 200 nm (200 nm, AR = 1) were taken up at a slower rate (1.2 % of the cell population/minute) than its non-symmetrical rod-like 150 nm x 450 nm counterpart (5.2 % of the cell population/minute). A strong dependence on surface charge was observed, where after 4 hours of incubation with the HeLa cells, positively charged particles were internalized by 84 % of cells and negatively charged particles were not internalized to any significant amount (< 5%). All particles tested possessed minimal toxicity, even at long incubation times (72

hours). Transmission electron microscopy (TEM) clearly showed clathrin-mediated endocytosis as one of many methods of endocytosis for these particles.

The most commonly accepted belief for cellular internalization in the literature suggests that particles larger than 200 nm will not be internalized by non-phagocytic cells; however, using a range of techniques, it was observed that cylindrical PRINT particles as large as 1 μm were internalized into HeLa cells [9-11]. This was the first report of the intracellular uptake and transport of biologically-relevant nanoparticles greater than 200 nm into non-phagocytic mammalian cells. In addition, it was found that rod-like, high aspect nanoparticles can be internalized into non-phagocytic cells much more rapidly and efficiently than would be expected based on size considerations alone, suggesting a special role associated with the shape of the particles. It is hypothesized that the interplay between particle shape and size at constant surface chemistry will undoubtedly play a role in particle targeting strategies and may even shed some light on the rationale behind bacterial pathogen sizes and shapes.

5.1.2 Preliminary biodistribution studies of PRINT particles

Preliminary *in vivo* studies of PRINT particles have now been conducted. Monodisperse 200 nm (AR = 1) PEG-based PRINT particles were fabricated and characterized via scanning electron microscopy, dynamic light scattering, and zeta potential analysis [12]. Incubation with HeLa cells showed no cytotoxicity, even at high particle concentrations. The biodistribution and pharmacokinetics of ^{125}I labeled particles were studied following intravenous (i.v.) administration in non-tumor

bearing C57BL/6J mice. The 200 nm (AR = 1) PRINT particles were distributed mainly in clearance organs (i.e. liver and spleen) throughout the time-course of the study. The degree of particle accumulation reported in the kidneys, heart, and lungs may over represent the actual accumulation since the mice were not perfused to clear these organs of blood. The decline in PRINT particle concentration in serum as a function of time followed a biexponential decay, showing characteristic distribution (half-life = 17 minutes) and elimination phases (half-life = 200 minutes). The rapid accumulation of the particles in the liver and the spleen as well as the relatively short elimination half-life indicates that after i.v. administration the particles were quickly recognized as foreign and removed from systemic circulation by the reticuloendothelial system (RES). This is not surprising considering that the steric coat on the PRINT particles was only a 1000 Da poly(ethylene glycol) (PEG) monomethylether. It has been suggested that the optimal coating for the creation of long-circulating liposomes is 2-5 kDa PEG [13,14]. The shorter PEG chains used in the current particle formulation may not offer a radius of protection that is sufficient to effectively block the adsorption of opsonic proteins. Once opsonization occurs, the particles are destined to be cleared by Kupffer cells in the liver and splenic macrophages.

5.1.3 Taking advantage of the enhanced permeability and retention effect

In these studies, PRINT nanoparticles were successfully conjugated to a near-infrared fluorophore useful for Xenogen imaging systems. This material allowed for whole animal imaging of 200 nm (AR = 1) PRINT particles in mice bearing a

Ramos tumor. In order to conduct imaging experiments, particles with amine handles were designed for the covalent conjugation of both DyLight 800 NHS ester, as well as PEG 5000 g/mol ligands. These experiments were performed using a PEG ligand density of $\sim 10^5$ PEG chains/200 nm particle. The whole animal images suggest a relatively short half-life with most of the particles sequestered in the liver. Once the organs were removed from the animals, and imaged as isolated entities, it was apparent that ~ 3.5 - 6.5 % of the recovered dose was found in the tumor tissue. The tumor accumulation was likely due to the enhanced permeability and retention (EPR) effect, seen in most solid tumors. This study was the first examination of the EPR effect of nanoparticles in Ramos tumors.

5.2 Recommendations for future work

A complete understanding of the molecular mechanisms involved for the internalization of particles into cells, as well as their fate once internalized, is crucial to the development of successful particle therapies. Obtaining knowledge on the endocytic pathway used from calibration quality particles should lead to crucial information required for not only enhancing specific cellular internalization, but also manipulating the intracellular location of particles, and minimizing cytotoxic effects. Future *in vitro* and *in vivo* studies should fully explore the interdependent roles of size, shape, surface chemistry, and modulus on multiple cell types, preferably ones that are clinically relevant. With all of these design parameters available in the engineering of the ideal nanocarrier for medicine, the future of PRINT technology looks very promising and fulfilling. There are a significant amount of studies

required to look at the various fundamental aspects of particles such as their size, shape, modulus, surface chemistry and to optimize those particle design criteria for each target application.

5.2.1 Engineering unique particle shapes and the *in vitro* and *in vivo* implications

Recent progress in fabrication of new master templates has yielded features with very unique sizes and shapes. Hexagonal particles or hex nut particles (diagonal diameter = 3 μm) have been fabricated and were used in preliminary *in vitro* studies using HeLa cells. The hex nut particles had the following composition: 67 wt % trimethyloxypropyl methacrylate triacrylate (MW = 428 g/mol), 20 wt % poly(ethylene glycol) monomethylether monomethacrylate (MW = 1,000 g/mol), 10 wt % 2-aminoethylmethacrylate hydrochloride (AEM·HCl), 2 wt % fluorescein-*o*-acrylate, and 1 wt % 2,2-diethoxyacetophenone. This particle is unique because it is an unfamiliar shape for cells. *In vitro* internalization of these particles was observed by confocal microscopy (Figure 5.1) and confirmed by TEM analysis (Figure 5.2). Additional studies aimed at examining the mode of internalization of these hex nut particles from outside the cells by SEM were performed (Figure 5.3). It was observed that the HeLa cells were using pseudopods to grab the hex nut particles and internalized them within the cells. The TEM microscopy indicated that endosomes form around the hex nut particles, in a hex nut shape. This is due to the endosome forming tightly around the particles.

This is a very unique shape for an endosome to take on and brings about some interesting fundamental questions, such as whether the pH inside an endosome of that size and shape would behave the same as an endosome around a 200 nm particle. These types of findings could help better engineer the ideal carrier for nanomedicine.

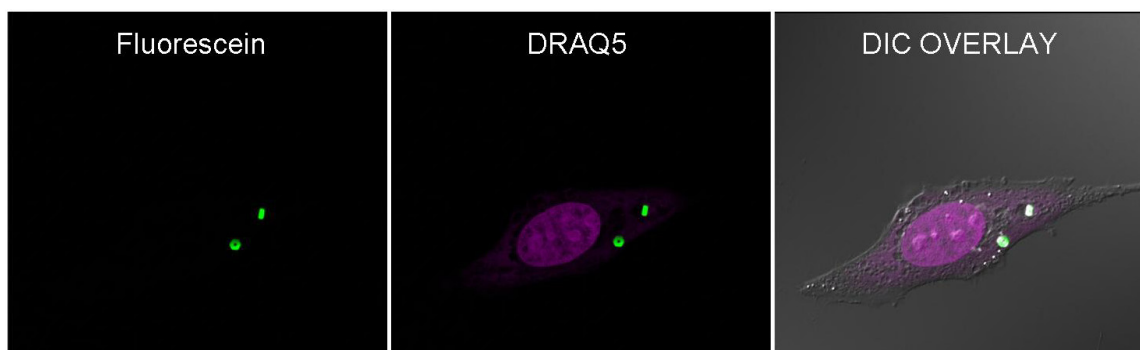


Figure 5.1 *In vitro* internalization of cationically charged hex nut PEG hydrogel particles by confocal microscopy

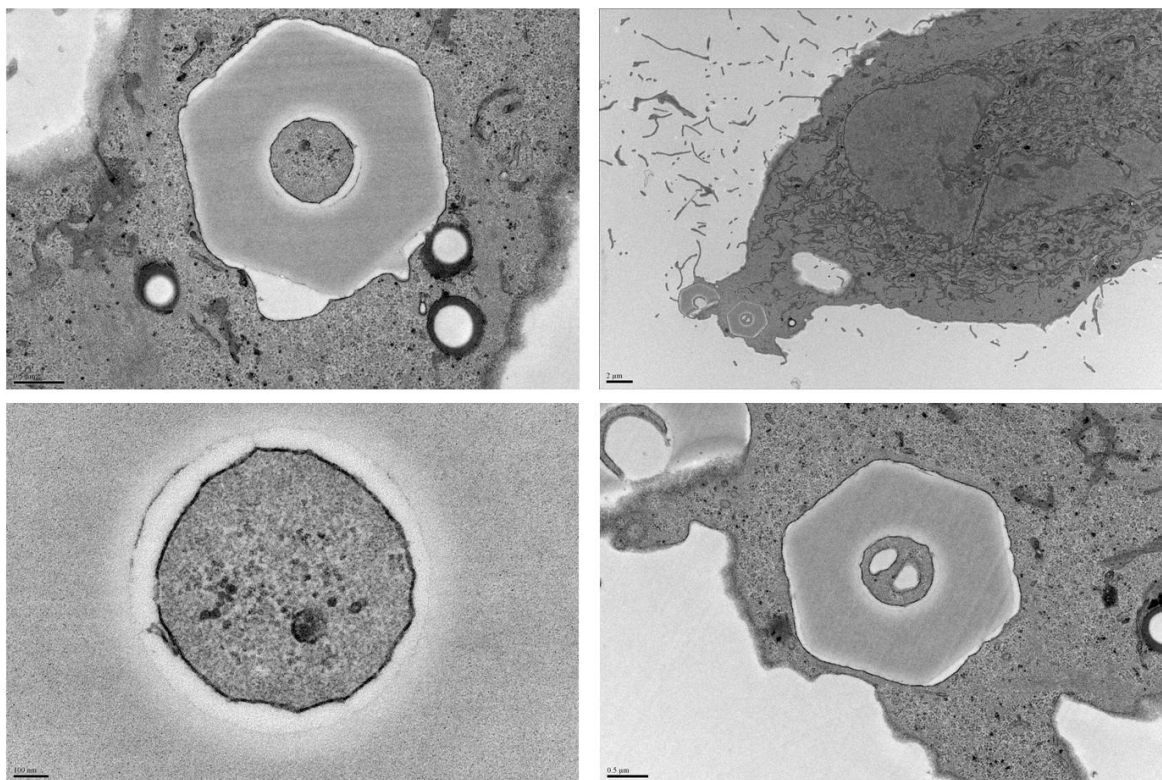


Figure 5.2 *In vitro* internalization of cationically charged hex nut PEG hydrogel particles by transmission electron microscopy

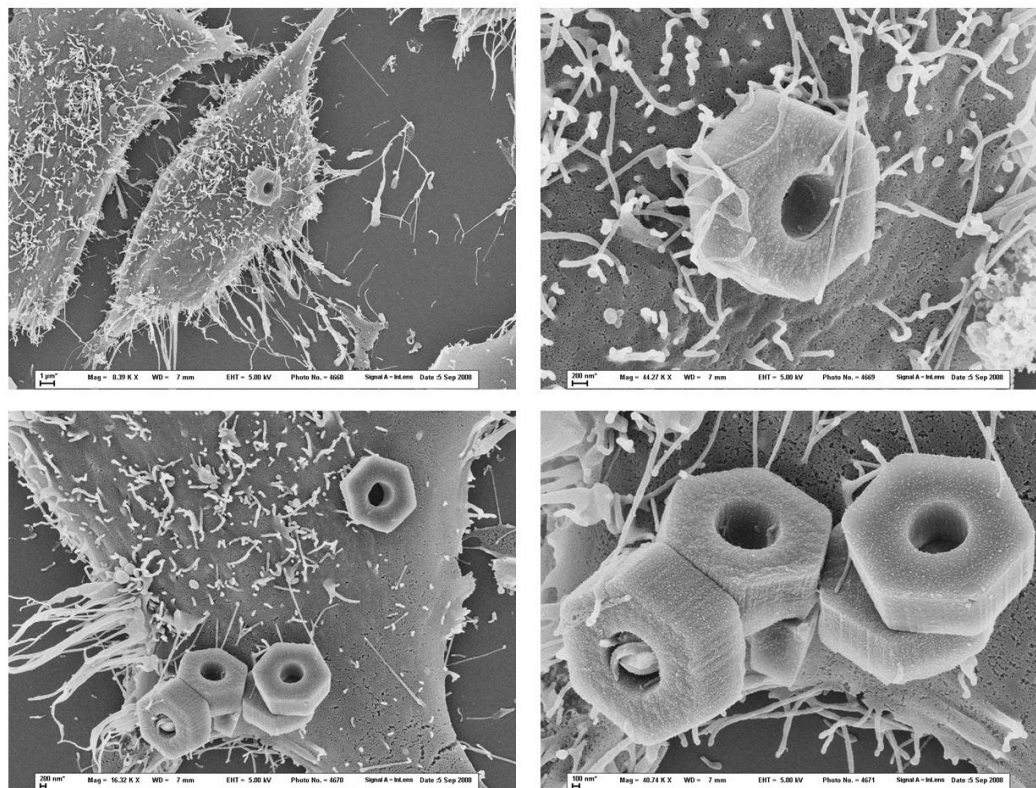


Figure 5.3 *In vitro* examination of cationically charged hex nut PEG hydrogel particles by scanning electron microscopy

5.2.2 Imparting superior control over particle surface chemistry

Advances in the field of nanotechnology, especially as it pertains to the design of particles, have allowed for the fabrication of very sophisticated moieties [15,16]. Controlling the distribution of matter along the surface of particles allows for an extra parameter in the design process beyond the fundamental size and shape considerations. In the field of life science, specifically where particle technologies are utilized, the particles produced are generally spherical in shape and very few examples exist where the particles contain anisotropy [17-23]. In the limited number of examples where the particles being examined *in vitro* or *in vivo* are non-spherical and hence contain shape anisotropy, to the best of our knowledge,

there are no examples of anisotropic particles with regards to shape where the particles also contain anisotropy in terms of their surface chemistry. Preliminary experiments examined labeling the exposed side of 2 μm (AR = 3) rectangular prisms and 3 μm hex nut particles while still in the mold. The particles were subsequently harvested, and purified, yielding particles with one side that have been post-functionalized. In these studies, particles were post-functionalized on one end with a fluorophore, to help visualize the process and for proof of principles purposes.

For the end-functionalized 2 μm (AR = 3) particles, AEM was used as a chemical handle for post-functionalization of the particle surface and was reacted with NHS-rhodamine to yield end-labeled particles. Filled molds with polymerized particles were inverted and placed in a large Petri dish containing 2×10^{-3} mg/mL NHS-rhodamine in borax buffer (pH = 8). The particles were allowed 90 seconds to react, washed with copious amounts of water, and then were subsequently harvested from the mold using a medical adhesive. Once the mold was removed, the adhesive film was transferred to a vial, where the adhesive was dissolved and washed away from the particles, leaving purified particles in solution (Figure 5.4). From our previous work, the matrix composition chosen yields particles with a positive zeta potential, however once a reaction of the surface amine groups occurs with acetic anhydride, the zeta potential switches to a negative potential [1]. Therefore, it was hypothesized that the end-functionalized particles described herein possess a positive surface charge where the particles appear to be green fluorescent due to the unreacted surface amine groups, and a negative zeta potential where the

surface amine groups have been reacted with NHS-rhodamine and now possess a red fluorescence (Figure 5.4).

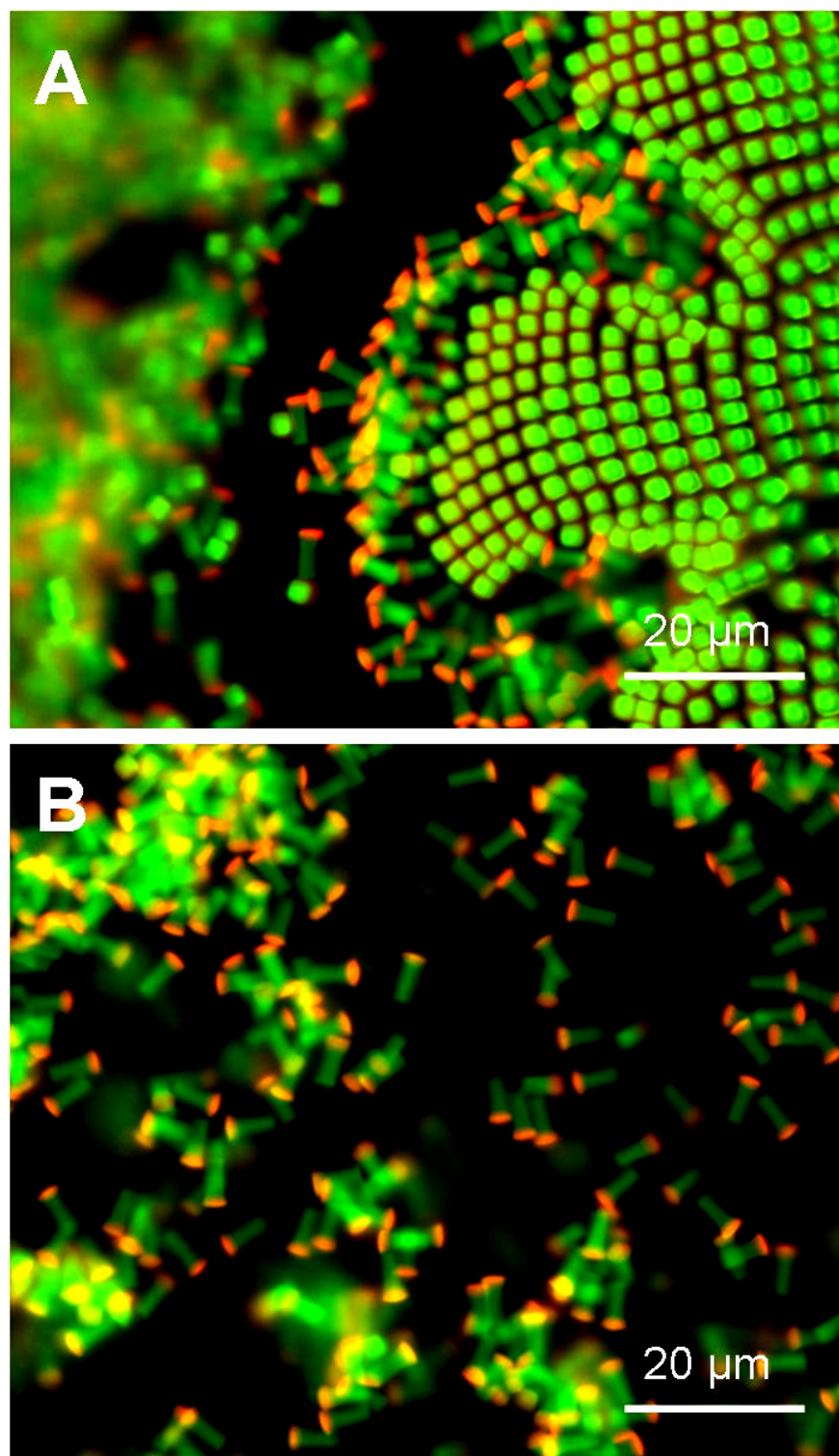


Figure 5.4 Fluorescent micrographs of 2 μm (AR = 3) PEG hydrogel end-functionalized particles. These particles contain fluorescein-o-acrylate in the particle matrix, and have been end-functionalized with NHS-rhodamine. A) Particles coming off the sacrificial adhesive layer, and B) Purified particles dispersed in an aqueous solution.

This concept was tested by performing some *in vitro* screens of the 2 μm (AR = 3) PEG hydrogel end-functionalized particles. In all cases observed, the 2 μm (AR = 3) PEG hydrogel end-functionalized particles associated with the cellular membrane of human cervical carcinoma epithelial (HeLa) cells such that the positively charged surfaces (green) were membrane-bound and the negatively charged surface (red) was the furthest surface from the cellular membrane (Figure 5.5). This electrostatic interaction was expected since it is known that the cell membrane has a negative charge due to the proteoglycans on the surface. Complete internalization of the 2 μm (AR = 3) PEG hydrogel end-functionalized particles was not seen most likely due to the large size of the particles. In these studies, the larger anisotropic 2 μm (AR = 3) particles were chosen to facilitate microscopy studies where the visualization of individual particles was possible.

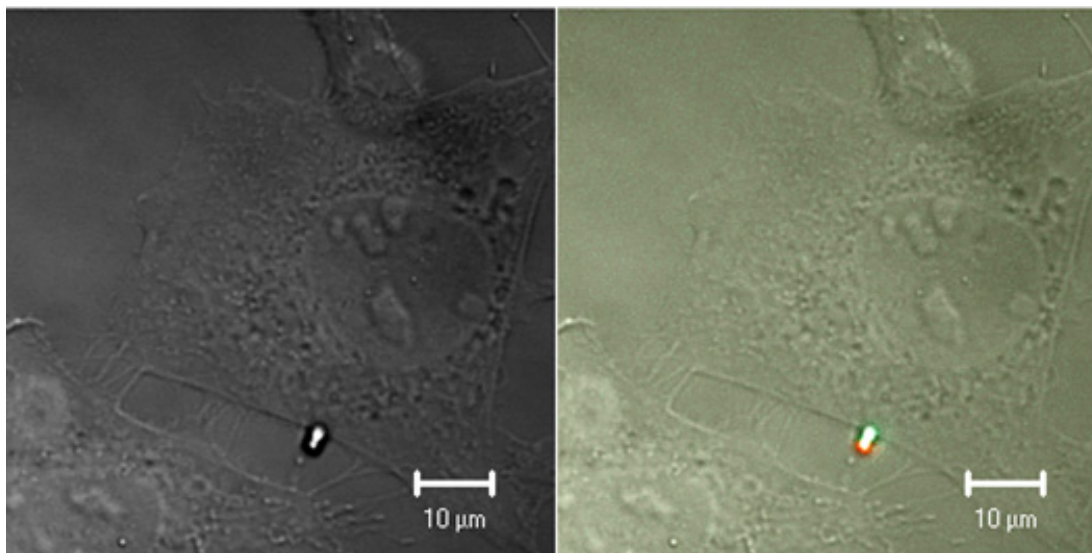


Figure 5.5 Confocal micrographs of 2 μm x 2 μm x 6 μm PEG hydrogel end-functionalized particles interacting with HeLa cells. These particles contain fluorescein-*o*-acrylate in the particle matrix, and have been end-functionalized with NHS-rhodamine. In all cases observed, the positively charged end of the particle interacted with the negatively charged membrane of the cells.

The end-functionalization process was extended to another size and shape, hex nut particles (Figure 5.6). In these experiments, hex nut particles were fabricated, and once polymerized in the mold, the one exposed surface was reacted with NHS-rhodamine such that end-functionalized particles were produced.

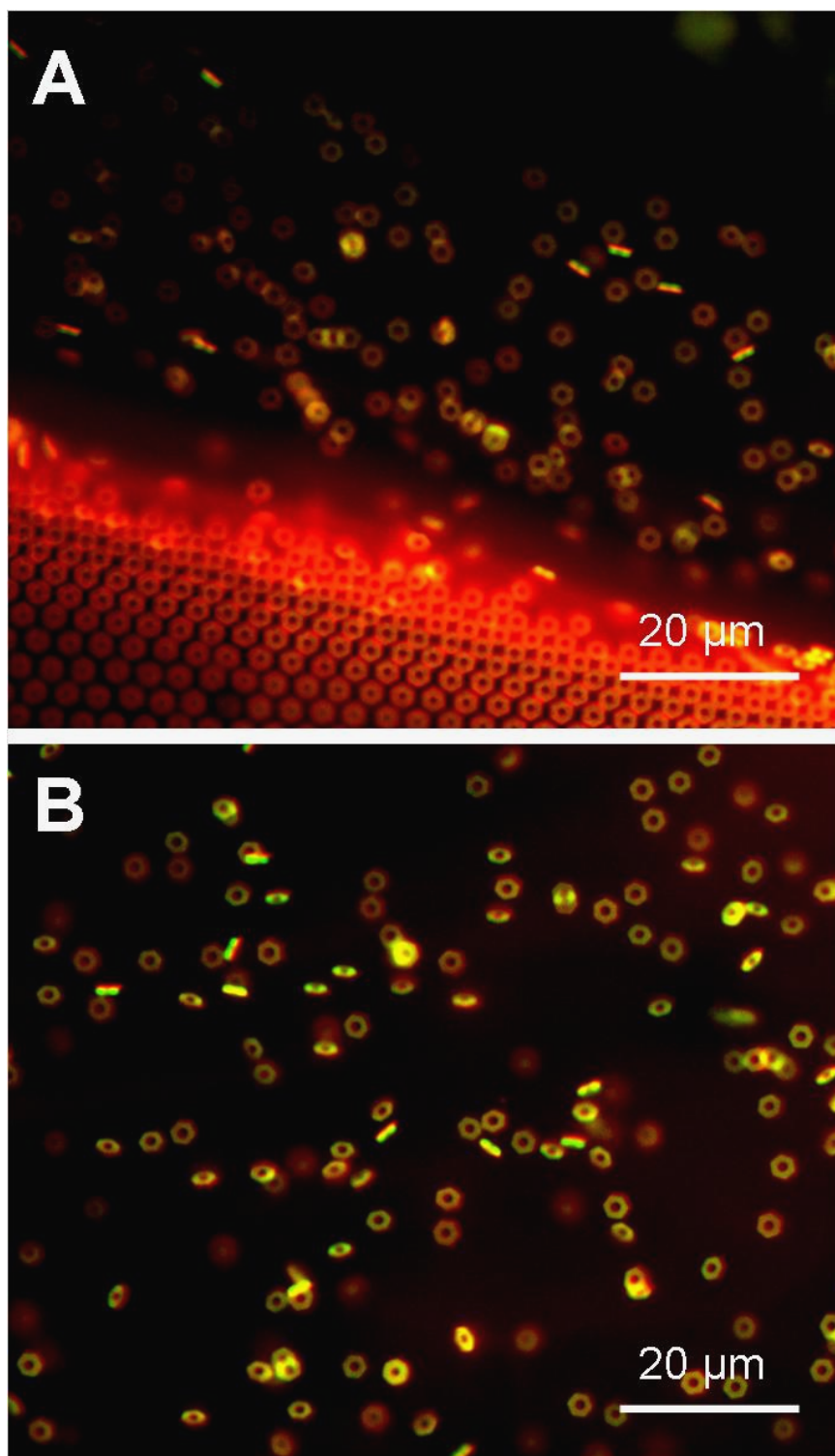


Figure 5.6 Fluorescent micrographs of hex nut PEG hydrogel end-functionalized particles. These particles contain fluorescein-o-acrylate in the particle matrix, and have been end-functionalized with NHS-rhodamine. A) Particles coming off the sacrificial adhesive layer, and B) Purified particles dispersed in an aqueous solution.

The ability to functionalized particles in a controlled site-specific manner adds a new level of control for the design of effective carriers in nanomedicine for the treatment of disease. Early *in vitro* results suggested an enhanced internalization of rod-like nanoparticles over a more symmetrical nanoparticle, having identical particle matrix compositions and roughly equal particle volumes [1]. Moreover, it was found that PRINT particles use multiple pathways of endocytosis for internalization into a cell and that a significant reduction of particle internalization occurred when the particles had a negative zeta potential versus particles that having positive zeta potential [1,24]. From our earlier work, a potential strategy arose for enhancing the specificity of particle targeting to cells of interest by utilizing negatively charged particles with targeting ligands conjugated to the outside of the particles [1]. With this new control over surface chemistry, a new design parameter has unfolded – beyond size and shape – allowing for more in depth studies to be conducted to monitor the effect of directed end-on internalization of anisotropic particles to learn the effects of controlled entry into cells on both targeting efficiencies as well as the modes of endocytosis.

5.2.3 Actively targeting cancer cells using a targeting ligand

The majority of *in vivo* studies conducted thus far have looked at the biodistribution of 200 nm (AR = 1) particles. It is clear that these particles have a relatively short half-life and are predominantly sequestered by the Kupffer cells in the liver. Further studies are required to fully explore the effect of particle matrix, size, shape, surface chemistry, and modulus. By altering these design parameters,

nanoparticles should provide truly engineered materials that circulate for extended times *in vivo*. Future projects should focus on engineering non-spherical particles with a degradable matrix such that the cargo release rate can be tailored for a specific application. Additional levels of sophistication can be designed into the particles through the covalent attachment of targeting ligands to facilitate receptor mediated endocytosis, whether it be in a controlled fashion on one end of the particles, or all over its surface. Determining both spacer length to the targeting ligand, as well as ligand density will require a substantial amount of work, however, these types of studies will allow for the realization of a truly optimized nanocarrier.

5.2.4 Examining the effect of modulus on *in vivo* circulation times

Preliminary *in vivo* experiments were conducted to examine the effect of modulus on 7 μm particles (AR = 0.25) (Figure 5.7). Here, red-blood cell mimics were fabricated in the hopes that these flexible 7 μm particles would behave similarly to red blood cells in their ability to navigate the barriers that confront them in the body [27]. It is known that red blood cells have circulation half-lives of 120 days and are able to circulate for extended times due to their ability to deform and pass through tight junctions [27]. In these experiments a non-crosslinkable PEG moiety (PEG 550 g/mol) was mixed into the monomer matrix (acting as a porogen) in varying amounts to determine if the flexibility of particles would affect circulation times *in vivo*. Early results suggest that highly flexible particles could indeed persist *in vivo* for longer times than their rigid counterpart, however these particles maintained a high amount of accumulation in the lungs (Figure 5.7B and D). The

particles accumulation was measured using a fluorescent detection method at 488 nm, which was not the ideal mode of quantification due to the high amount of autofluorescence that occurs at that wavelength. Future experiments should look into more flexible particles and quantify the *in vivo* distribution based on a more quantitative method (Iodine-125 or fluorescence detection at a higher wavelength to avoid the high background signal obtained from the mouse autofluorescence). The ideal carrier in this case would be a long circulating degradable particle optimal for slow, continual release of a cargo over an extended period of time.

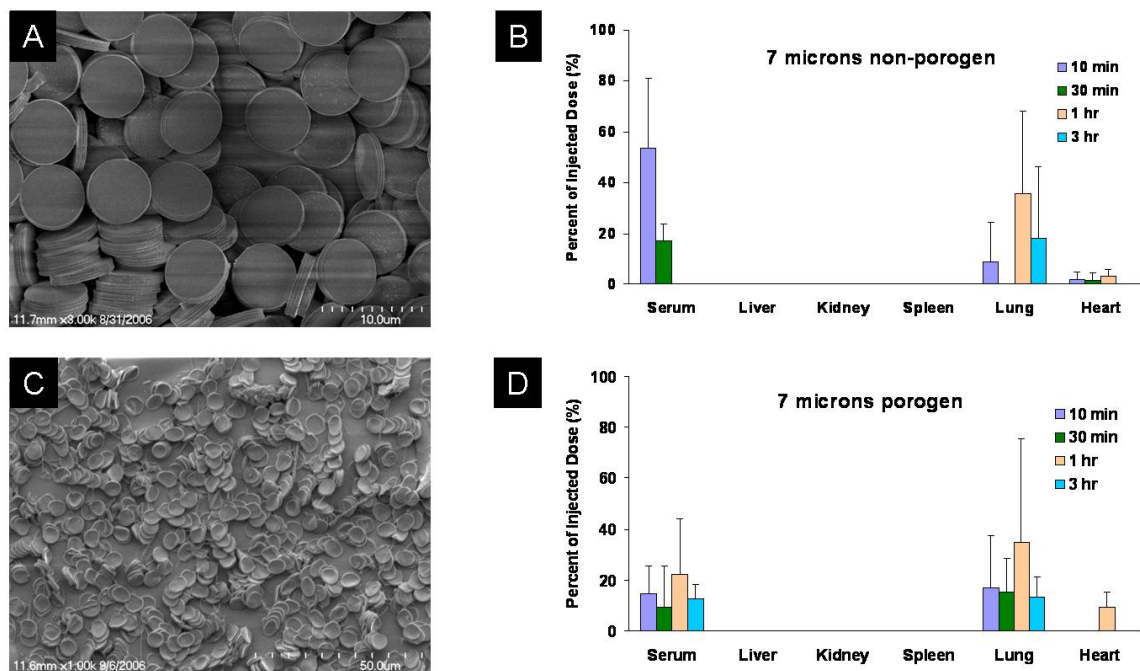


Figure 5.7 The effect of modulus on circulating artificial red blood cells. A) SEM micrograph of rigid 7 µm particles (AR = 0.25, no porogen), B) the biodistribution of rigid 7 µm particles (AR = 0.25, no porogen), C) SEM micrograph of flexible 7 µm particles (AR = 0.25, 50 wt% porogen), D) the biodistribution of flexible 7 µm particles (AR = 0.25, 50 wt% porogen)

5.3 References

- (1) Gratton, S. E. A.; Ropp, P. A.; Pohlhaus, P. D.; Luft, J. C.; Madden, V. J.; Napier, M. E.; DeSimone, J. M. *Proceedings of the National Academy of Sciences of the United States of America* **2008**, *105*, 11613-11618.
- (2) Champion, J. A.; Mitragotri, S. *Proc. Natl. Acad. Sci. U.S.A.* **2006**, *103*, 4930-4934.
- (3) Rejman, J.; Oberle, V.; Zuhorn, I. S.; Hoekstra, D. *Biochemical Journal* **2004**, *377*, 159-169.
- (4) Zauner, W.; Farrow, N. A.; Haines, A. M. R. *J. Controlled Release* **2001**, *71*, 39-51.
- (5) Harush-Frenkel, O.; Debotton, N.; Benita, S.; Altschuler, Y. *Biochemical and Biophysical Research Communications* **2007**, *353*, 26-32.
- (6) Champion, J. A.; Katare, Y. K.; Mitragotri, S. *Journal of Controlled Release* **2007**, *121*, 3-9.
- (7) Champion, J. A.; Mitragotri, S. *Proceedings of the National Academy of Sciences of the United States of America* **2006**, *103*, 4930-4934.
- (8) Euliss, L. E.; DuPont, J. A.; Gratton, S.; DeSimone, J. *Chemical Society Reviews* **2006**, *35*, 1095-1104.
- (9) Gary, D. J.; Puri, N.; Won, Y. Y. *Journal of Controlled Release* **2007**, *121*, 64-73.
- (10) Oupicky, D.; Konak, C.; Ulbrich, K.; Wolfert, M. A.; Seymour, L. W. *Journal of Controlled Release* **2000**, *65*, 149-171.
- (11) Conner, S. D.; Schmid, S. L. *Nature* **2003**, *422*, 37-44.
- (12) Gratton, S. E. A.; Pohlhaus, P. D.; Lee, J.; Guo, J.; Cho, M. J.; DeSimone, J. M. *Journal of Controlled Release* **2007**, *121*, 10-18.
- (13) Moghimi, S. M.; Hunter, A. C.; Murray, J. C. *Pharmacological Reviews* **2001**, *53*, 283-318.
- (14) Owens, D. E.; Peppas, N. A. *Int. J. Pharm.* **2006**, *307*, 93-102.
- (15) Euliss, L. E.; DuPont, J. A.; Gratton, S.; DeSimone, J. *Chem. Soc. Rev.* **2006**, *35*, 1095-1104.

- (16) Davis, M. E.; Chen, Z.; Shin, D. M. *Nature Reviews Drug Discovery* **2008**, *7*, 771-782.
- (17) Champion, J. A.; Katare, Y. K.; Mitragotri, S. *Proceedings of the National Academy of Sciences of the United States of America* **2007**, *104*, 11901-11904.
- (18) Rolland, J. P.; Maynor, B. W.; Euliss, L. E.; Exner, A. E.; Denison, G. M.; DeSimone, J. M. *Journal of the American Chemical Society* **2005**, *127*, 10096-10100.
- (19) Bianco, A.; Kostarelos, K.; Prato, M. *Current Opinion in Chemical Biology* **2005**, *9*, 674-679.
- (20) Geng, Y.; Dalhaimer, P.; Cai, S. S.; Tsai, R.; Tewari, M.; Minko, T.; Discher, D. E. *Nature Nanotechnology* **2007**, *2*, 249-255.
- (21) Muro, S.; Garnacho, C.; Champion, J. A.; Leferovich, J.; Gajewski, C.; Schuchman, E. H.; Mitragotri, S.; Muzykantov, V. R. *Molecular Therapy* **2008**, *16*, 1450-1458.
- (22) Roh, K. H.; Martin, D. C.; Lahann, J. *Nature Materials* **2005**, *4*, 759-763.
- (23) Roh, K. H.; Yoshida, M.; Lahann, J. *Langmuir* **2007**, *23*, 5683-5688.
- (24) Gratton, S. E. A.; Napier, M. E.; Ropp, P. A.; Tian, S.; DeSimone, J. M. *Pharmaceutical Research* **2007**, *In Press*.
- (25) Hilgenbrink, A. R.; Low, P. S. *Journal of Pharmaceutical Sciences* **2005**, *94*, 2135-2146.
- (26) Lu, Y. J.; Xu, L. C.; Parker, N.; Westrick, E.; Reddy, J. A.; Vetzal, M.; Low, P. S.; Leamon, C. P. *Molecular Cancer Therapeutics* **2006**, *5*, 3258-3267.
- (27) Chien, S. *Annual Review of Physiology* **1987**, *49*, 177-192.